THESIS

# ANALYZING POST-FLOOD RECOVERY AFTER AN EXTREME FLOOD: NORTH ST. VRAIN CREEK, CO

Submitted by

Johanna S. Eidmann

Department of Geosciences

In partial fulfillment of the requirements

For the Degree of Master of Science

Colorado State University

Fort Collins, Colorado

Summer 2018

Master's Committee:

Advisor: Sara Rathburn

Ellen Wohl
Peter Nelson

# ABSTRACT

## ANALYZING POST-FLOOD RECOVERY AFTER AN EXTREME FLOOD: NORTH ST. VRAIN CREEK, CO

Assessing the ongoing sediment remobilization and deposition following an extreme flood is important for understanding disturbance response and recovery, and for addressing the challenges to water resource management. From September 9-15, 2013, a tropical storm generated over 350 mm of precipitation across the Colorado Front Range. The resulting 200-year flood triggered landslides and extreme channel erosion along North St. Vrain Creek, which feeds Ralph Price Reservoir, water supply for the Cities of Lyons and Longmont, CO. The flood resulted in 10 m of aggradation upstream of the reservoir, transforming the reservoir inlet into an approach channel. 4 years after the flood, downstream transport of flood sediment and deposition in the reservoir continues. This research tracks the fate of flood-derived sediment to understand the evolution of the approach channel and delta to assess post-flood response processes and controls and to quantify sediment remobilization. Photographic analysis and DEM differencing of the approach channel indicates that the majority of channel response to the flood occurred within 1 year following the flood. Evolution of the channel from an initial plane bed occurred through channel incision of up to 2.5 m and widening of up to 10 m, forming a trapezoidal cross section. Channel geometry changes in years 2-5 post-flood are limited in spatial extent, largely dependent on sediment discharge and local variations in channel confinement. Bathymetric DEM differencing from 2014 and 2016 (years 1 and 3 post-flood) indicates a minimum sediment accumulation of 68,000 m$^3$ on the delta plain, and progradation of 170 m of the delta front since the 2013 flood. Between fall 2016 and spring 2017, the reservoir level was dropped approximately 10 m during construction at the spillway, creating a base level drop, delta incision, and causing over 15,000 m$^3$ of sediment to be transported further into the reservoir. Based on bathymetry and reservoir core analyses, a

total of 74,000 $m^3$ of sediment was deposited in the delta from 2014 through 2017, producing an estimated loss of 0.4% in reservoir storage capacity. Approximately 184,000 $m^3$ (equivalent to another 1% of reservoir storage capacity) is estimated to remain in storage upstream of the reservoir. Although the approach channel appears to be adjusted to a typical snowmelt runoff, stored sediment remaining upstream of the reservoir indicates that complete recovery of the approach channel may not occur on a management time scale. The remaining large volume of sediment still in storage upstream highlights the potential for future disturbances to trigger additional sediment inputs.

ACKNOWLEDGEMENTS

This field research could not have been completed without the close collaboration and help of many people. I especially appreciate the help of Ken Huson and Jamie Freel for continuously supporting this project, helping coordinate field efforts, and providing data when needed. I would also like to thank Dave Dust and Adam Nielson for both helping with various field activities and flying a quadcopter for photogrammetry surveys. Thanks to Juli Scamardo for offering her canoeing expertise to successfully conduct the August 2017 bathymetry survey, and Michael Gordon for proving to be a tremendously helpful and willing field assistant. I also thank Brandon McElroy for lending me his sonar equipment for bathymetry surveys. I thank Christy Briles for providing the equipment necessary to collect cores and sharing her lab space for processing samples. I'd additionally like to thank Christy Briles, Ben Wise, and the remainder of Christy's coring crew for offering their time and help to both collect and process core samples. Thanks to Mike Ronayne for teaching me how to krig my survey data, as well as Eryn Torres for teaching me how to krig using the Earth Volumetric Studio (EVS) software. I'd also like to thank Geosyntec Consultants for allowing me continuous access to EVS. Thanks to Michael Baker for helping me troubleshoot Matlab scripts, and Lisa Stright for letting me use her computers for many months of Structure from Motion troubleshooting and modeling. I thank Katherine Lininger and Annette Patton for their willingness to edit multiple versions of my writing and discussing ways to improve the presentation of my research. Thanks to Derek Schook for his help with fieldwork and ability to capture photographs of the coring procedure in action. I thank Ryan Brown for providing invaluable guidance on how to process RTK GPS data, and Anthony Mainiero, Erin Davidson, Cahill Kelleghan, and Ethan Hervey for helping out with various field tasks. A special thanks to Ian Nesbitt for providing 24/7 I.T. support, and to the fluvial geomorphology research group at CSU for keeping me motivated and continuously providing feedback on analytical methods, fieldwork, and more. I would especially like to thank the City of Longmont, American Water Resources Association (Colorado and National chapters), Colorado Water Institute, Colorado Scientific Society, American Engineering

Geologists, Anchor QEA, LLC, and Colorado State University for financially supporting this research. Finally, I would like to thank Sara Rathburn for her unwavering support and enthusiasm throughout this research process, commitment to transform me into a better researcher (and reign me in when necessary), and willingness to devote all of her energy towards ensuring a successful and fruitful research experience.

TABLE OF CONTENTS

LIST OF TABLES

LIST OF FIGURES

# Chapter 1

# Introduction

Large sedimentation events occur naturally through floods (Magilligan et al., 2014; Rathburn et al., 2017), volcanic eruptions (Montgomery and Buffington, 1997), wildfires (Moody, 2017), and mass movements (Madej et al., 2009). They can also be anthropogenically-induced via land cover changes (Church and Ferguson, 2015), gravel mining (Simon and Rinaldi, 2006; Church and Ferguson, 2015), dam removal (East et al., 2015; Magilligan et al., 2016), and sediment releases from dams (Scott and Gravlee, 1968; Wohl and Cenderelli, 2000). Over the past several decades, research has made progress on predicting and understanding fluvial system response to sedimentation events (e.g. Lisle (1982); Buraas et al. (2014); Magilligan et al. (2014)), but additional work is needed as geomorphologists are tasked with answering questions about how natural systems adjust to climate change and will adjust in the future (Lane, 2013; Gregory and Lewin, 2015).

Previous studies have identified multiple controls on fluvial responses to disturbances, including the magnitude and frequency of discharge fluctuations, channel geometry, bedform characteristics, and the geomorphic legacy of an area (Wolman and Miller, 1960; Balog, 1980; Wolman and Gerson, 1978; Magilligan et al., 1998; Church and Ferguson, 2015; Fryirs, 2017; Naylor et al., 2017). Due to the complex interplay between these factors, distinguishing their relative impact on river adjustment remains a challenge (Newson, 1980; Florsheim et al., 2008; Buraas et al., 2014). Identifying the most important controls on channel adjustments following sedimentation events is further limited by variability in research areas (location, scope, and size), lack of studies that analyze adjustments over a sufficiently long timescale, as well as technological constraints that (until recently) limit the resolution and frequency of channel measurements (Coats et al., 1985; Buraas et al., 2014). Understanding channel response to sedimentation events is becoming increasingly important in a changing climate, where naturally-occurring extreme events associated with increased sedimentation are predicted to become more frequent (Naylor et al., 2017). As a result, anticipating impacts on fluvial systems, especially in reference to water resources, is of prime interest to geomorphologists, engineers, and land resource managers.

This research tracks channel response, sedimentation, and ongoing recovery of North St. Vrain (NSV) Creek and Ralph Price Reservoir in Boulder County, CO, following a large sedimentation event that was triggered by a >200-year flood in 2013. In addition, a planned 10 m drop in base level between fall 2016 and spring 2017 provided an opportunity to evaluate system response to a larger-than-normal base level change. My analyses focus on documenting on-going channel evolution of NSV Creek and quantifying reservoir sedimentation 5 years following the flood and during the pronounced drop in base level. I first review existing research on morphodynamic adjustments of fluvial systems following extreme floods and base level changes, describe the study area, and present objectives and hypotheses for this research (Chapter 1). I then outline the field and laboratory methods applied during this research (Chapter 2), and present the results of my analyses (Chapter 3). I analyze my results in relation to objectives, critically examine my hypotheses, and evaluate overall system response to flood disturbance and a change in base level (Chapter 4). Finally, I summarize the main research findings and comment on future research that will further enhance understanding of fluvial system response to large sedimentation events (Chapter 5).

## 1.1 Channel Morphodynamics

### 1.1.1 Existing Conceptual Models

To determine the influence of sedimentation events on fluvial system response, it is useful to assess established conceptual models that encapsulate the connection between various drivers (e.g. incoming water and sediment) and channel morphodynamics (channel process and form). Lane (1955) presented a relation that identifies channel response based on a balance of ‘dynamic equilibrium’ in which adjustments in channel form (e.g. sinuosity and slope) and bed aggradation or degradation are connected to changes in grain size, water discharge and sediment discharge. For example, an increase in water discharge and/or slope produces an increase in transport capacity and channel incision. Conversely, an increase to sediment discharge and/or grain size increases sediment supply and channel aggradation. His model was expanded upon and modified by Doyle and Shields (2000) and Dust and Wohl (2012), who incorporate progressive grain size changes due to channel evolution, and channel width-depth ratios, respectively.

Although Lane (1955)'s conceptual model is still widely used by geomorphologists and engineers to understand general interactions between discharge and channel change, others have emphasized the need to incorporate site-specific channel characteristics at the reach scale to better predict channel adjustment (Madej et al., 2009; Church and Ferguson, 2015). For example, in narrow and confined reaches, channel adjustments to disturbances have been found to occur primarily through changes in bed elevation via aggradation and erosion rather than modifications in sinuosity (Madej et al., 2009). In expansive floodplains, however, adjustments primarily occur through a combination of changes to bed elevation and sinuosity (Madej et al., 2009). Physical variation throughout a reach and channel network is also important to consider, as localized differences in flow characteristics can result in inconsistencies of adjustments throughout a reach (Church and Ferguson, 2015).

### 1.1.2 Disturbances and Channel Change

#### Flood Response

Previous research uses multiple approaches to better understand changes in channel form and sediment dynamics resulting from floods. Extreme storms and floods produce rapid increases in water and sediment discharge, large, visible changes to river channels, and provide a natural scenario that illustrates the complex interaction between various responses (Florsheim et al., 2008). Sediment remobilization and channel widening are identified as common fluvial responses to catastrophic floods across different environments (Lisle, 1982; Simon, 1992; Krapesch et al., 2011; Magilligan et al., 2014; Tamminga et al., 2015; Wicherski et al., 2017). Lisle (1982) analyzed the affects of the December 1964 flood in northern California, during which he noticed a general response of channel widening. He also found that sediment remobilization from channels produced pool infilling, which in turn led to an overall decrease in bedform roughness and reduced the threshold for sediment transport. Others have identified channel widening to occur via bank sloughing in response to vertical incision, as a means for rivers to enhance channel conveyance and accommodate larger flows (Madej et al., 2009).

Although water discharge is a primary driver of channel change, the magnitude of channel adjustments vary based on discharge magnitude and duration. Magilligan et al. (2014) analyzed the impacts of Tropical Storm Irene in the Northeastern U.S. and found that distinguishing water discharge duration from magnitude and unit stream power was important for predicting the spatial extent of channel adjustments. Tropical Storm Irene (a short, high-magnitude event) produced channel widening that was limited to isolated portions of the study reach. As a result, Magilligan et al. (2014) defined the storm as a 'selectively effective' flood that contributed a large volume of sediment to the channel, but did not produce widespread changes in channel morphology.

It is also important to consider antecedent geomorphic events when predicting post-flood morphological changes in a system (Hooke, 2015; Naylor et al., 2017). According to Wolman and Gerson (1978) and Brunsden and Thornes (1979), an event of similar magnitude and forcing can produce vastly different responses in a channel due to different event histories. Magilligan et al. (1998) found this to be true on the Upper Mississippi River, where he discovered that the 1993 flood produced a more moderate sedimentological impact than a flood of similar magnitude that had occurred in 1983. As a result, holding other driving forces equal, the chronology of events, in terms of system response and recovery, plays a significant role in observed channel changes, adding to the complexity of such interpretations.

**Dam Removal and Sediment Release**

Over the past three decades, aging dams and restoration efforts have prompted an increase in dam removal (Pizzuto, 2002; Magilligan et al., 2016). For geomorphologists, the removal of a dam provides an opportunity to perform a controlled experiment on the channel response upstream of the dam due to a drop in base level (Scott and Gravlee, 1968; Pizzuto, 1994; Blizard and Wohl, 1998; Doyle and Harbor, 2003; Doyle et al., 2003; Hooke, 2007; East et al., 2015; Randle et al., 2015; Magilligan et al., 2016). A common response across study sites includes enhanced upstream vertical channel incision due to knickpoint migration that further triggers channel widening through bank collapse (Pace et al., 2016).

In addition, planned or accidental sediment releases from dams provide further insight into channel change as they isolate identified drivers (i.e. high-magnitude flood discharges) from changes in sediment grain size and discharge. Although sediment flux has been identified as a driver of channel adjustments, sediment movement in and out of in-channel storage is still not fully understood (Wohl and Cenderelli, 2000; East et al., 2015). Dam removals and reservoir sediment releases are thus important analogs to assess flood-induced sedimentation and a drop in base level, respectively.

## 1.2 Study Area

North St. Vrain (NSV) Creek begins in Rocky Mountain National Park in Colorado and drains 245 $km^2$ east of the continental divide (Wohl et al., 2004; Rathburn et al., 2017). Geology of the drainage basin consists of middle Proterozoic Silver Plume granite, Precambrian gneiss, biotite schist, Holocene and late Pleistocene landslide deposits, and Pleistocene Pinedale deposits (Braddock and Cole, 1990; Wohl et al., 2004). Defined by a semi-arid climate, the majority of the runoff and measured peak discharges of the NSV are associated with spring snowmelt between May and July, whereas thunderstorms during the summer months can generate lower discharges through flash floods (Wohl et al., 2004; Rathburn et al., 2017).

Ralph Price Reservoir within Button Rock Preserve in north Boulder County (Figure 1.1a) provides municipal water to the Cities of Longmont and Lyons ($\sim$100,000 residents). Fed by the NSV, the reservoir captures 100% of the sediment transported by the creek (Figure 1.1b) and impounds $19 \times 10^6$ $m^3$ (16,000 af) of water (Rathburn et al., 2017). In an average year, the reservoir water level fluctuates approximately 6.4 m (21 ft) between a spillway elevation of 1,950.7 m and low stand of 1,944.3 m. The planned drop in base level fall 2016 - spring 2017 was associated with a total drop of 9.4 m (31 ft) in reservoir level to an elevation of 1,941.3 m.

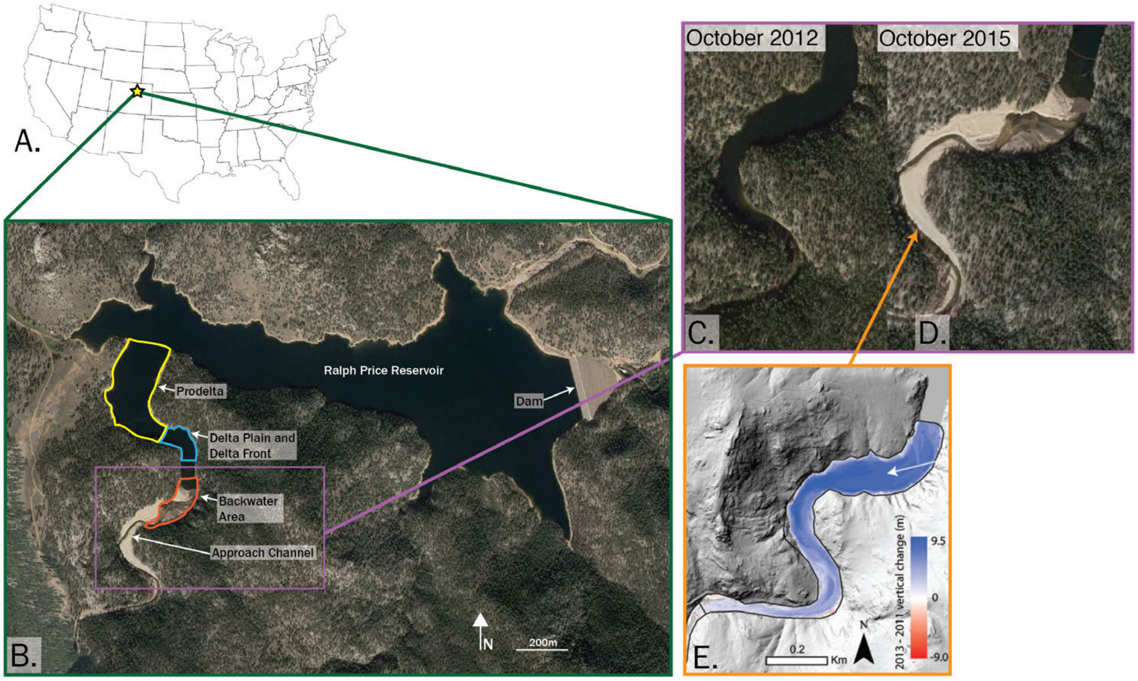


**Figure 1.1:** Images showing the location of the study area (a), and relevant areas of interest along North St. Vrain (NSV) Creek and Ralph Price Reservoir (b). Google Earth satellite images from October 2012 (c) and October 2015 (d) show sediment aggradation at the approach channel of NSV Creek due to the 2013 flood. Image (e) illustrates sediment aggradation at the approach channel from Rathburn et al. (2017).

This study focuses on an approximately 1 km reach of the NSV before it enters Ralph Price Reservoir, as well as the reservoir inlet that is characterized by a depositional delta and defines the southern 800 m of the reservoir (labeled 'prodelta', 'delta plain', and 'delta front' in Figure 1.1b). This analyzed reach is characterized by alternating pool-riffle and multi-thread segments, as is identified by Montgomery and Buffington (1997)'s classification scheme.

# 1.3 The September 2013 Storm

## 1.3.1 Regional Impacts

From September 9-16, 2013, a large-scale atmospheric flow pattern brought an unusual amount of moisture into the Colorado Front Range. The tropical storm generated between 200 and 450 mm of precipitation (Figure 1.2) across a 3,430 km$^2$ area, with the most intense precipitation rates of 50-70 mm/hr and 40-60 mm/hr occurring in a 6-hour and 5-hour time period on September 12-13, 2013 (Coe et al., 2014; Gochis et al., 2015). The nature, magnitude, and duration of the storm was exceptional, especially considering its location within the semi-arid continental interior during a typically dry season in Colorado (Coe et al., 2014; Gochis et al., 2015). In the aftermath of the storm, 18 counties were declared federal disaster areas by the Federal Emergency Management Agency (FEMA), 18,000 people were displaced, 8 lives were lost, at least 1,880 structures were destroyed, and over 485 miles of highway were damaged, amounting to over $2 billion in damages (Coe et al., 2014; Gochis et al., 2015).

In addition to its economic impacts, the rainfall also triggered widespread landslides and debris flows across the Front Range. Within the first day of the storm, rainfall had sufficiently saturated slope materials, enabling the subsequent moderate to intense rainfall to trigger widespread debris flows (Anderson et al., 2015; Wieczorek and Glade, 2005). As a result, the storm caused over 1,100 landslides and debris flows that excavated hundreds to thousands of years of hillslope weathering products from the Front Range slopes (Anderson et al., 2015; Gochis et al., 2015; Rathburn et al., 2017).

### 1.3.2 Flood Impacts to Ralph Price Reservoir

The September 2013 storm impacted every major river in the Front Range, producing prolonged and widespread flooding (Gochis et al., 2015). NSV Creek was one of the most affected rivers. Areas within its watershed experienced some of the most extreme rainfall of over 400 mm (Figure 1.2), causing the NSV to have an estimated peak flow of 280-348 $m^3/s$ and a >200-year flood (Houck, 2014; Yochum, 2015). These increased flows caused extensive damage to existing infrastructure along NSV Creek (refer to Appendix A for more information). The main access road and water supply pipeline from the reservoir were washed out and the gaging station located on the NSV upstream of Ralph Price Reservoir was completely removed by the flood.

Within a 15 km reach of the NSV upstream of the reservoir, over 108 documented landslides (ranging in volume from 10,000-23,000 $m^3$) contributed sediment and debris to the river channel (Rathburn et al., 2017). Approximately 300,000 $m^3$ of the 500,000 $m^3$ flood-derived sediment

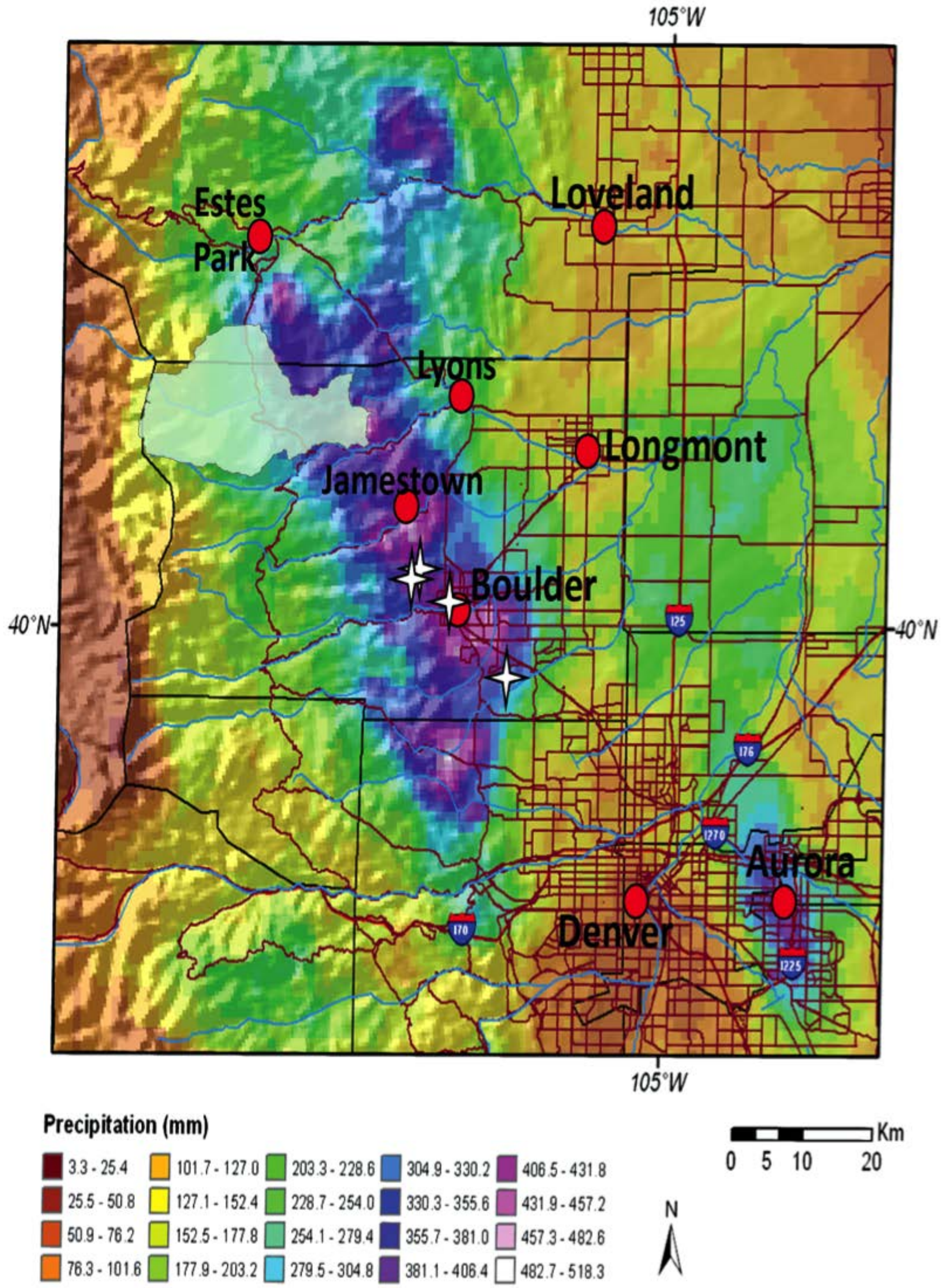


**Figure 1.2:** Total precipitation accumulation measurements (mm) across the Front Range due to the September 2013 storm (9/9/2013-9/17/2013) (from Gochis et al. (2015)). The light green shaded area represents the spatial extent of the North St. Vrain watershed feeding Ralph Price Reservoir (USGS Streamstats) and where flood impacts were most pronounced. This area upstream from Ralph Price Reservoir is 100 km$^2$. For reference, dark red lines denote major roads and highways and red dots represent approximate town and city center locations

eroded from the hillslopes were deposited at the inlet of Ralph Price Reservoir, producing 10 m of aggradation and transforming the inlet into an approach channel (Figure 1.1c and d) (Rathburn et al., 2017). The influx of sediment transported into the reservoir additionally produced a 2-4% loss of its storage capacity and caused the delta to prograde over 20 m (Rathburn et al., 2017). A sediment core collected at the delta of the reservoir in 2014 indicated that an equivalent of 100 years of sedimentation was delivered to the reservoir by the storm (Rathburn et al., 2017).

Despite the storm's direct impact, over 40% of the material eroded by the September flood remains stored as unconsolidated flood deposits in the catchment and channel upstream of the reservoir (Rathburn et al., 2017). During the snowmelt runoff in 2014, over 3 m of channel incision was produced, and a sediment volume equivalent to that deposited by the flood was remobilized and deposited into the reservoir (Rathburn et al., 2017).

In addition to continued channel recovery and sediment remobilization, the reservoir and NSV Creek have been impacted by changes in base level. Between fall 2016 and spring 2017, the reservoir level was dropped nearly 10 m to its lowest elevation since 1989 to aid downstream post-flood bridge reconstruction efforts. The response of sediment movement in the reservoir and at the approach channel due to this base level drop is therefore superimposed on continued post-flood channel recovery.

## 1.4 Research Objectives

The NSV approach channel and delta in Ralph Price Reservoir are an ideal location to study the natural channel development of a river following an extreme flood because the catchment is largely undeveloped, with minimal human impacts (e.g. land development, logging activities, or flow regulation). In addition, little unquantified post-flood clearance of sediment was completed since the storm, providing insight into an unaltered and natural response of the NSV and its recovery (Rathburn et al., 2017).

Although previous literature has identified many drivers of channel change, these studies often observe a short time frame (e.g. 1 year or less) following a disturbance, despite the fact that channel recovery occurs over multiple years to decades (Madej et al., 2009). This research focuses on changes to the approach channel and reservoir delta that occur over 1 year, between 2016 and 2017, as well as changes to the delta since the September 2013 flood through fall 2017.

The overarching goals of this research are twofold: 1) to contribute to existing research on the rate of channel development and sediment movement of a coarse-grained river affected by an extreme flood disturbance and; 2) to assess the rate of sediment remobilization, channel change, and additional reservoir sedimentation to inform reservoir management. Three specific research objectives will address these goals:

- Objective 1: Identify channel response between 2016 and 2017 and determine the relative rate and magnitude of these adjustments,
- Objective 2: Quantify delta aggradation and erosion due to the 2013 flood, for the 5 years following the flood, and resulting from the planned drop in base level.
- Objective 3: Compare volumetric changes in sediment at the channel with that of the delta to evaluate whether there is a direct relationship between channel erosion of the approach channel and reservoir sedimentation at the delta.

## 1.5 Hypotheses

The hypotheses tested in this thesis link to the research objectives as follows:

**Objective 1:**

Identify channel response between 2016 and 2017 and determine the relative rate and magnitude of these adjustments.

**Hypothesis 1:**

The post-flood response of the approach channel will be an increase in channel width:depth, channel slope, and sinuosity.

**Rationale 1:**

Rathburn et al. (2017) documented an initial flood response through an increase in sediment supply from landsliding and channel erosion. This input produced 10 m of aggradation at the inlet, creating a plane bed defined by a shallow slope. As the approach channel evolves, I expect post-flood discharges of lower magnitude to entrain and transport the easily erodible unconsolidated sediment, causing vertical incision of the channel into the plane bed. Incision will induce bank collapse and channel widening once it has surpassed a critical bank height. According to the modified Lane's Balance (Dust and Wohl, 2012), the channel will accommodate the increased width:depth ratio through an increase in slope and sinuosity, as detailed below:

$$Q_w^{\downarrow}\left(\frac{\triangle z}{\rho H_a}\right)^{\uparrow} \propto Q_s^{\downarrow} D_s^{\downarrow}\left(\frac{w}{d}\right)^{\uparrow}$$

where $Q_w$ is water discharge, $Q_s$ is sediment discharge, $\triangle z$ is slope, $\rho$ is sinuosity, $H_a$ is bed amplitude, w is width, and d is depth. It should be noted that in this research the relative change of water discharge, sediment discharge, and grain size were only qualitatively examined, whereas changes in slope, sinuosity and width:depth were quantified.

**Objective 2:**

Quantify delta aggradation and erosion due to the 2013 flood, for the 5 years following the flood, and resulting from the planned drop in base level.

**Hypothesis 2a:**

As the NSV recovers, I predict a nonlinear decrease in sediment flux with time to the delta. As a result, I expect to see a progressive decrease in both volumetric aggradation at the delta and progradation of the delta front (see hypothesized disturbance response curve, Figure 1.3).

**Hypothesis 2b:**

A 10 m drop in reservoir base level provided an opportunity to test another hypothesis related to post-flood reservoir delta changes. I predict that the base level drop will enhance the rate of

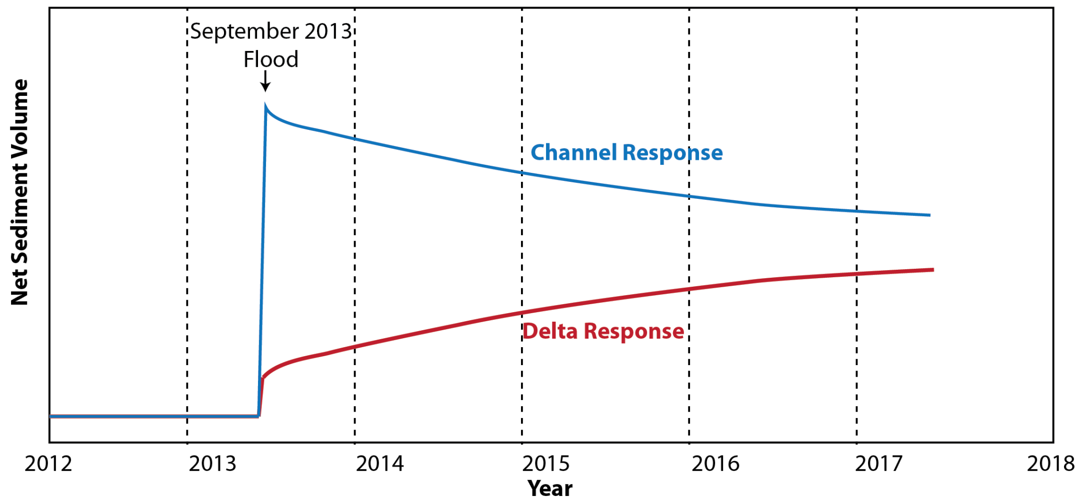


**Figure 1.3:** A conceptual model illustrating the relative predicted change in volume of the approach channel and delta with time since the September 2013 flood. Note that the y-axis is not scaled, but should rather be used to illustrate relative volumetric changes.

vertical channel incision and channel widening at the approach channel (related to Hypothesis 1), and produce incision of the delta plain.

**Rationale 2:**

Based on field and laboratory flume experiments, Pizzuto (2002) noted a decrease in sediment supply with distance and time since a sedimentation event. I therefore expect an overall decrease in the volume of sediment added to the approach channel (via erosion) of NSV Creek following the flood. Post-flood discharge will winnow fine bed sediments, resulting in channel armoring that further decreases sediment flux and transport capacity needed to deliver sediment to the inlet (Church and Ferguson, 2015). Based on dam removal research, a drop in base level is expected to produce upstream incision, which in turn creates a knickpoint, enhances knickpoint migration, increases channel slope downstream from the knickpoint, and increases sediment flux into the reservoir (Pace et al., 2016; Doyle et al., 2003).

**Objective 3:**

Compare volumetric changes in sediment from the approach channel with volumes of the delta to evaluate whether there is a direct relationship between channel erosion of the approach channel and reservoir sedimentation at the delta.

**Hypothesis 3:**

I expect measured volumetric changes in channel geometry upstream of the reservoir to approximate the volumetric aggradation and progradation of the delta.

**Rationale 3:**

The study location at the confluence of the NSV into Ralph Price Reservoir is unique, because 100% of the sediment that is transported by the creek is captured by the reservoir. As such, it is possible to develop a sediment budget that tracks sediment movement out of channel storage and into the reservoir.

# Chapter 2

# Methodology

## 2.1 Field Methods

### 2.1.1 Drone Flights and Surveying

A quadcopter was flown over an 800 m reach of the approach channel (identified in Figure 1.1b) to capture the images required for photogrammetric analysis. Drone flights took place in April 2017 and October 2017–prior to and following 2017 spring snowmelt runoff.

A DJI Phantom 3 PRO quadcopter was flown over the inlet on April 23, 2017 and collected 2,189 images from approximately 30 m above ground surface using an FC300X camera. Each image had a resolution of 4000x3000 pixels, a focal length of 3.61 mm, F-stop of F/2.8, and ISO of 100. Twenty-one 5'x5' black and white targets were placed on both sides of the NSV channel and dispersed across the analyzed area (labeled Targets 1-21 in Figure 2.1). The coordinates and elevation of the center of each target were then surveyed using a Topcon GR-5 Real Time Kinematic (RTK) GPS (0.01 m horizontal accuracy and 0.015 m vertical accuracy). The images were processed using Agisoft PhotoScan Professional (version 1.4.1) to create a high resolution DEM of the field area (Appendix C.7).

To measure the changes in channel geometry following spring 2017 snowmelt runoff, a second aerial survey was conducted on October 3, 2017. A DJI Phantom 4 PRO drone was flown over the inlet also at 30 m above ground surface using an FC6310 camera. Each image had a resolution of 5472x3078 pixels, a focal length of 8.8 mm, F-stop of F/4.5, and ISO of 100. Twenty-five targets (labeled Targets A-Y in Figure 2.1) were spread out on both sides of the NSV channel, and were similarly surveyed using the RTK. Through this field effort, 997 images were captured and processed.

A limitation to photogrammetry is the inability to detect terrain that is either under water or underneath vegetation. Little vegetation covers the approach channel due to the dry, unconsolidated


**Figure 2.1:** Target locations for the April and October 2017 drone surveys

sand and gravel comprising the flood deposit. Although recent literature documents the ability to capture subaqueous topography in clear water (Dietrich, 2017), the sparse point cloud from photogrammetry analysis revealed that limited subaqueous points were collected at this field site. Instead, channel geometry beneath the water surface was measured by topographic survey. Survey points were collected at approximately 1-3 m spacing with the RTK at the top and bottom of each bank, along bedrock outcrops, and along the thalweg. Additional points were collected at multi-thread channels or depositional bars to incorporate these topographic characteristics.

The 2016 channel geometry RTK surveys were conducted on August 3, 2016 and September 1, 2016. The 2017 post-snowmelt channel geometry was also surveyed the following year, on July 7, 2017, July 8, 2017, July 10, 2017, September 16, 2017, September 17, 2017, and October 1, 2017. During each field effort, survey coordinates were calculated using the average of three fixed point locations. To ensure accurate post-processing point correction, when possible the base station remained in the same location for at least 2 hours (Appendix C.1).

### 2.1.2 Discharge Measurements

To record discharge at NSV Creek, automatic repeat pictures were taken of a staff plate mounted on the former gaging station weir at 1-hour increments each day beginning in April 2017. Because the camera could not capture photographs at night, the total number of photographs obtained per day varied depending on the time of year and total hours of daylight.

The staff gage located at the weir was used as a scale reference for the repeat images. However, because the staff gage was secured to the weir after the storm without an accurate measure of datum, it was not used for stage measurement. Using Adobe Photoshop, a scale of 58 pixels on the photograph was calculated to represent 0.3048 m (1.0 ft) at the weir. Using this scale, the distance between the top of the weir and stage was visually measured. This distance was deducted from the surveyed elevation of the the weir (1,949.68 $\pm$ 0.012 m) to determine the elevation of the stage. The calculated elevation was then applied to the existing rating curve of the USGS weir to determine fluctuations in water discharge with time.

### 2.1.3 Approach Channel Grain Size Analysis

Pebble counts were conducted in summer 2014 and 2017 at seven locations across the approach channel (Appendix C.4). Analyses at each location followed the Wolman (1954) method (n=100) and took place across a 10 m-by-10 m area. Results from 2014 and 2017 were compiled and compared to analyze any temporal changes in grain size distribution.

### 2.1.4 Bathymetric Surveys

Repeat bathymetric surveys were conducted across the delta plain (outlined in blue in Figure 1.1b). This area was delineated based on the largest area of overlap between all bathymetric surveys. Survey data were used for three purposes: 1) to track the movement of the delta front, 2) to analyze sediment remobilization and movement, and 3) to quantify the volume of sediment deposited in the reservoir on the delta plain. Surveys were conducted prior to snowmelt runoff in April 2014, April 2016, and May 2017. Due to the low reservoir level in May 2017, an additional and more detailed bathymetric survey was also conducted in August 2017.

For all bathymetric surveys, a Lowrance HDS 7 sonar with a 200kHz transducer was used (Figure C.1a in Appendix C.3). The May 2017 survey is of limited use because of the unusually low reservoir level. As such, that survey was only used to track the delta front and not for volumetric calculations.

### 2.1.5 Reservoir Core Collection

A total of 12 cores (Figure 2.3) were collected across the delta at Ralph Price Reservoir after the September 2013 flood. All but two cores were collected from a boat using a Livingstone surface coring device (Figure 2.4a) and extruded into previously-cut split spoon samplers. Cores C and D were collected on the subaerially-exposed delta by advancing a 1.5 m-long PVC tube into the sediment with a rubber mallet (Figure 2.4b). Information pertaining to core coordinate locations, measurements, depth of retrieval, and length of subsampling is compiled in Table 2.1 and Appendix C.3.

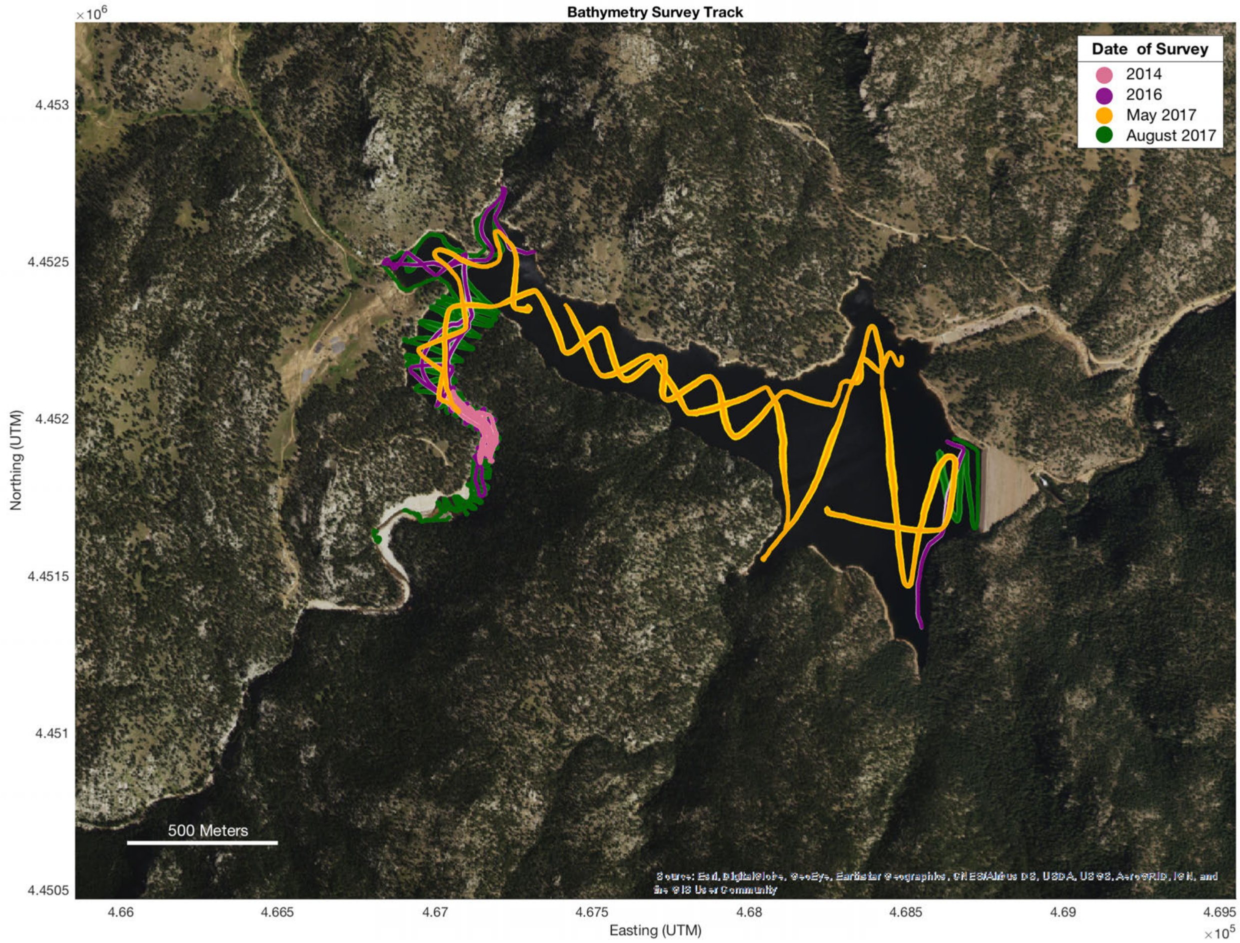


**Figure 2.2:** Google Earth image overlain by the survey paths across the reservoir for each bathymetry survey conducted.

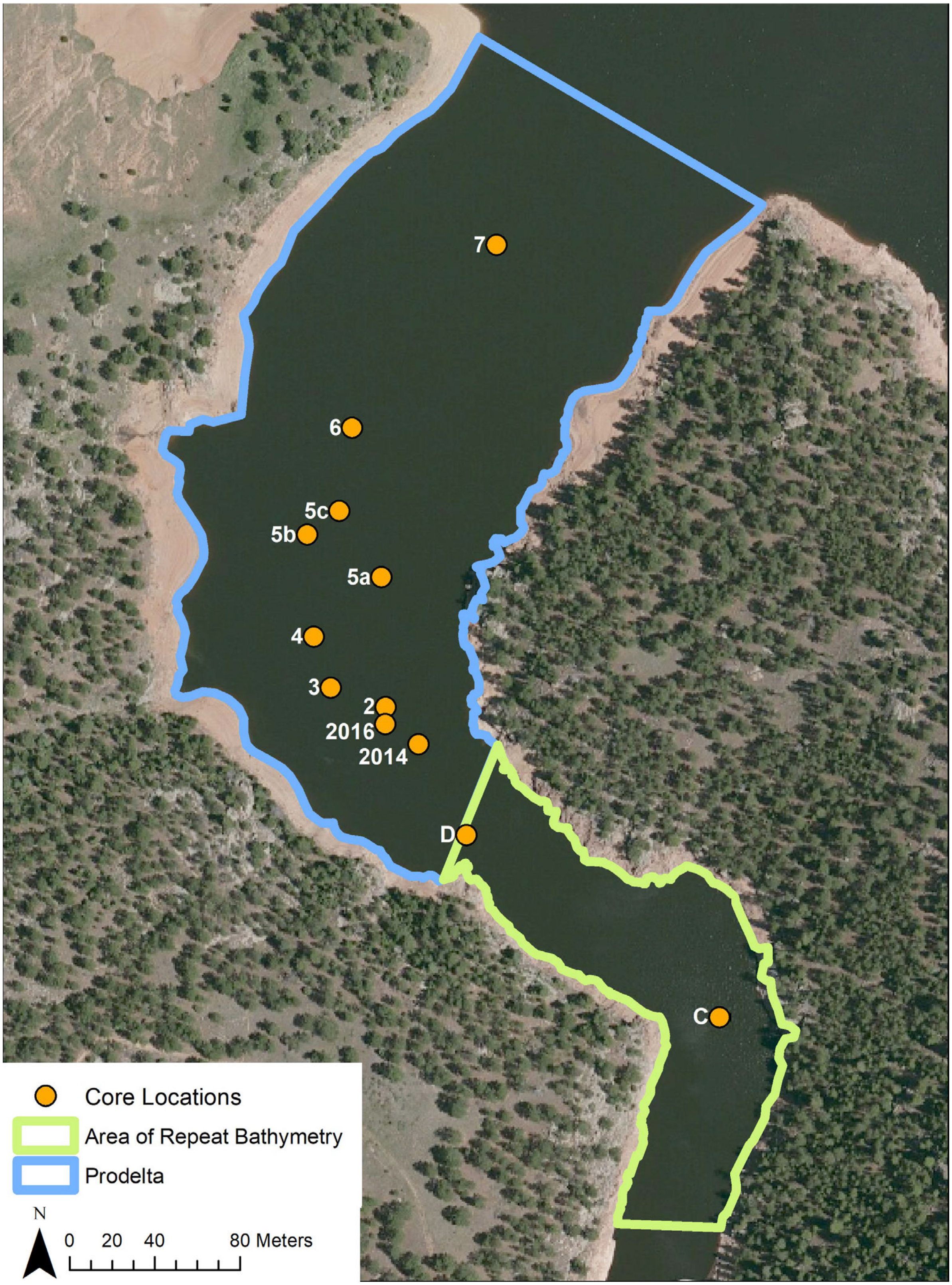


**Figure 2.3:** Google Earth image of the area of repeat bathymetry at the reservoir inlet, including the locations of each core collected from the reservoir prodelta.

**(a)** A field photograph of a core collected using a Livingstone surface corer

**(b)** A field photograph of the collection of Core D on the exposed delta surface during the base level drop in 2016-2017.

**Figure 2.4:** Field images of methods used to collect cores across the delta.

## 2.2 Laboratory Methods

### 2.2.1 Core Analyses

Following the collection of the sediment cores, each was stored in a plastic tube. Prior to analysis, each core was prepared by splitting it into two halves–an archive and working half. Due to the high moisture content of the sediment, the cores were air dried for 12 hours, covered in plastic wrap, and stored at 4°C.

#### Visual Core Stratigraphy and Texture Analysis

Each core was visually inspected for variations in grain size, soil texture, and color. A Munsell Soil Color chart was used to determine visual color changes and help correlate stratigraphic layers amongst the cores. Lamination thickness and patterns, indications of organic material, and soil texture were qualitatively assessed and recorded.

**Table 2.1:** Field data pertaining to core sampling information, core length, and additional comments.

| Core Name | Collection Date | Sample Elevation (m) | Whirlpack Sample (cm) | Total Core Length (cm) | Additional Notes |
|---|---|---|---|---|---|
| Core 2014 | 4/11/2014 | 1928.89 | – | 65 | Core not collected after two attempts due to loss of bottom sandy layer. A 14+ cm-thick sand lens was noted to extended up to a depth of over 42 cm below the water-sediment interface. |
| Core 2016 | 4/23/2016 | 1934.83 | 0-7 | 45 | |
| Core 1 | 4/22/2017 | – | – | – | Core not collected due to sediment loss out of the bottom caused by a thick, unconsolidated sandy layer. |
| Core 2 | 4/22/2017 | 1929.76 | 0-3 | 54 | Sandy top layer |
| Core 3 | 4/22/2017 | 1932.32 | 0-3 | 51 | 5 coring attempts |
| Core 4 | 4/22/2017 | 1934.18 | 0-5 | 84 | |
| Core 5A | 4/22/2017 | 1927.31 | – | 79 | 3 coring attempts; had to extrude plug later |
| Core 5B | 4/21/2017 | 1933.67 | 0-6 | 59 | |
| Core 5C | 4/22/2017 | 1930.81 | 0-6 | 69 | |
| Core 6 | 4/21/2017 | 1929.68 | 0-6 | 54 | |
| Core 7 | 4/21/2017 | 1924.07 | 0-17 | 77 | |
| Core C | 5/17/2017 | 1924.07 | – | 45 | |
| Core D | 5/17/2017 | 1924.07 | – | 113 | |

### Magnetic Susceptibility

Magnetic susceptibility (relative concentrations of iron-bearing minerals measured in centimeter-gram-second, or cgs) was measured at 1 cm intervals with a Bartington MS2E point sensor (Gedye et al., 2000). Because temperature can impact recorded concentrations, analysis was only conducted once the core was at room temperature.

### Loss-on-Ignition

Loss-on-ignition (LOI) quantifies sediment water content and total organic carbon, providing an additional metric for stratigraphic correlation. Due to the effort required to process a sample, each core was subsampled at locations representative of each stratigraphic change. Because Core 4 contained the most stratigraphic complexity, this core was sampled at 1 cm intervals. The LOI analysis procedure, as well as the subsampling depths at each core, are detailed in Appendix C.5.

### X-ray fluorescence (XRF)

X-Ray Fluorescence (XRF) analysis was performed to determine the geochemistry and elemental signature of stratigraphic units throughout the cores (Finkenbinder et al., 2014). These analyses were conducted from the same samples used for LOI analysis. Once LOI analysis was complete, samples were ground up and homogenized using an agate mortar and pestle. The sediment for each sample was then compacted into a p-XRF tube and covered with a 4 µm ultralene window film.

### Grain Size Analysis

Grain size analysis of core samples was completed in a series of steps. First, each sample was pretreated to remove organic matter in the sample. Following pretreatment, samples were sieved through a series of three, 3-in diameter standard sieves (500 µm, 250 µm, and 125 µm). Lastly, laser particle size analysis was conducted to quantify the proportion of very fine sand, silt, and clay (<125 µm) in each sample. Sediments in Cores C and D did not go through a pretreatment step and were sieved through a series of five, 3-in diameter standard sieves (2 mm, 1 mm, 500 µm, 250 µm, and 125 µm). Detailed analytical procedures of grain size analyses can be found in Appendix C.5.

## 2.3 Analytical Methods

### 2.3.1 Delta Volumetric Analysis

Volumetric analysis was conducted through ordinary kriging of bathymetry survey data across the delta plain and delta front (covering approximately 14,000 $m^2$). To verify the volumetric calculations, kriging was completed using two methods: 1) the Stanford Geostatistical Modeling Software (SGeMS) in conjunction with the Geomorphic Change Detection (GCD) ArcGIS package (Wheaton et al., 2010) and, 2) CTech's Earth Volumetric Studio software. Detailed analytical steps used for each method, as well as the variogram analysis results and applied kriging parameters are discussed in Appendix C.6.

### 2.3.2 Photogrammetry Analysis

Quadcopter imagery was imported and processed into a dense point cloud using Agisoft Photoscan Professional. The dense point clouds from each quadcopter survey were exported as .xyz files and further aligned in Cloud Compare. Refer to Appendix C.7 for a thorough overview of the process used to perform photogrammetry analysis.

#### Channel Morphology Differencing

To quantify volumetric differences in channel geometry between 2016 and 2017, RTK points collected over 10 field days were aligned and imported into ArcMap. Similar to the bathymetric surveys, the RTK points were kriged in SgEMs and processed into DEMs in ArcMap. DEMs from 2016 and 2017 were then differenced using GCD. Volumetric differencing of DEMs produced by SfM were evaluated for just changes in channel banks as well as changes in the complete channel topography (including the subaqueous river bed). Differencing of RTK-produced DEMs included all RTK measurement points. For more detailed information about the alignment and kriging procedure applied, refer to Appendix C.8.

# Chapter 3

# Results

## 3.1 Channel Development

Repeat photographs of the approach channel between November 2013 and March 2018 (Figure 3.1) qualitatively illustrate channel adjustment since the flood. The most noticeable changes occurred within the first year after the flood. Immediately after the 2013 flood, channel adjustments were dominated by vertical incision of approximately 0.3 m into the nearly plane bed surface (see photo 3/21/2014, Figure 3.1), forming the approach channel. The first year after the flood (2014 snowmelt), additional vertical incision of up to 0.5-1.5 m at the repeat photo location was coupled with bank collapse and channel widening to approximately 10 m (bottom width), producing a trapezoidal channel (photo 5/2/2015, Figure 3.1). Between years 2 and 5 (2015 - 2018), changes to channel geometry were less visible, with a documented maximum incision of 2.5-3.5 m and channel bottom width of 10 m in 2017.


**Figure 3.1:** Repeat photographs showing the channel development of the approach channel of NSV Creek upstream of the reservoir. All photos are from the same location except for 11/20/2013, which was taken approximately 300 m downstream. Photo on 11/20/2013 courtesy of Ken Huson.

**Table 3.1:** Morphological changes before and after the September 2013 flood. Channel slope and sinuosity were calculated from a topographic map (USGS (1957) for 1957) and RTK survey measurements (2014, 2015, 2016, and 2017). Channel width:depth ratios were calculated from measurements collected in the field.

| Date | Channel Slope (m/m) | Channel Sinuosity | Width:Depth |
|---|---|---|---|
| 1957 | 0.02 | – | – |
| 2014 | 0.006 | 1.5 | 9m/0.3m = 30 |
| 2015 | 0.008 | 1.5 | 10m/1.5m = 7 |
| 2016 | 0.008 | 1.5 | 10m/2.5m = 4 |
| 2017 | 0.008 | 1.5 | 10m/2.5m = 4 |

Measurements from the 1957 pre-dam topographic map (USGS, 1957) were compared to post-flood measurements (Table 3.1). Map measurements indicate that prior to the flood and the reservoir's construction (1969), the analyzed reach of the NSV had a slope of 0.02 m/m (USGS, 1957). Field evidence indicates a planar and shallow slope in 2014, followed by incision and steepening to a slope of 0.008 m/m in 2016. Comparison of 2016 and 2017 thalweg measurements additionally show little change in the overall channel slope and sinuosity index of 1.5 (Table 3.1, Appendix D.2). A longitudinal profile along the 2017 thalweg from field surveys, however, illustrates localized aggradation of up to 0.35 m and degradation of up to 0.95 m (at a confined bend) between 2016 and 2017 (Figure 3.2).

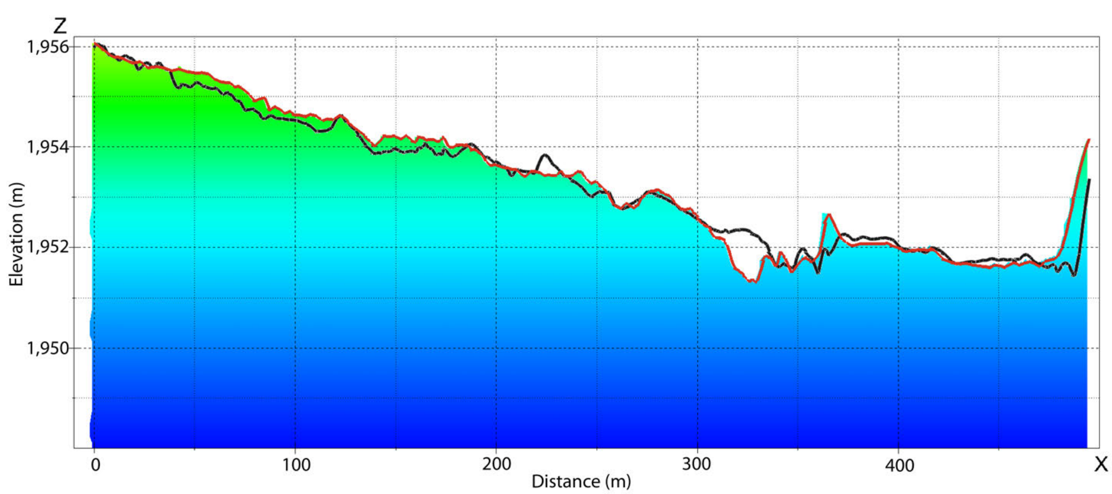


**Figure 3.2:** Longitudinal profile of the approach channel at North St. Vrain Creek showing changes in channel elevation between 2016 (marked in black) and 2017 (marked in red).

**Table 3.2:** Calculated volumetric changes at the approach channel based on the three methods of analysis. I have greater confidence in the RTK-derived DEMs due to the smallest vertical error and thus will use these values for my data analysis.

| Method Used | Method Vertical Error (m) | Volume Eroded ($m^3$) | Volume Deposited ($m^3$) | Net Volume Moved ($m^3$) | Total Volume ($m^3$) |
|---|---|---|---|---|---|
| SfM (just banks) | 1.2 | 1,250 ± 300 | 660 ± 200 | -580 ± 360 | 1,910 ± 500 |
| SfM (banks and river bed) | 1.2 | 2,260 ± 610 | 1,120 ± 430 | -1,040 ± 740 | 3,480 ± 1,040 |
| RTK | 0.004 | 890 ± 350 | 400 ± 220 | -490 ± 410 | 1,280 ± 570 |

DEMs created by SfM had a larger vertical error than those produced by RTK measurements (Table 3.2). The vertical error of SfM-derived DEMs was larger than anticipated due to variable lighting conditions, oblique angles, and too much overlap between photographs collected in the April 2017 survey. Differencing maps of pre- and post-2017 snowmelt DEMs produced using SfM and the RTK can be found in Appendix D.7, D.8, D.9 and D.10.

Results of DEM change detection analysis were calculated and compared (see Figure 3.3 and Table 3.2). Similarities in all three maps include channel incision of the inner, downstream bedrock bend (marked as 'Point A' in Figure 3.3). Google Earth satellite imagery additionally show that this bank collapse took place between June 9, 2017 and June 18, 2017 (Figure 3.4), which temporally overlaps with measured peak snowmelt discharges (Figure 3.5). Other changes illustrated by the differencing maps include lateral bank retreat at the most upstream and downstream outer bends (marked as 'Points B' in Figure 3.3).


**Figure 3.3:** Change detection of the 2016 and 2017 DEMs produced from the RTK point surveys. Points A and B denote areas of change discussed in the results and discussion sections.


**Figure 3.4:** Google satellite imagery from June 9, 2017 and June 18, 2017 showing bank collapse of the inner bend between this time period.

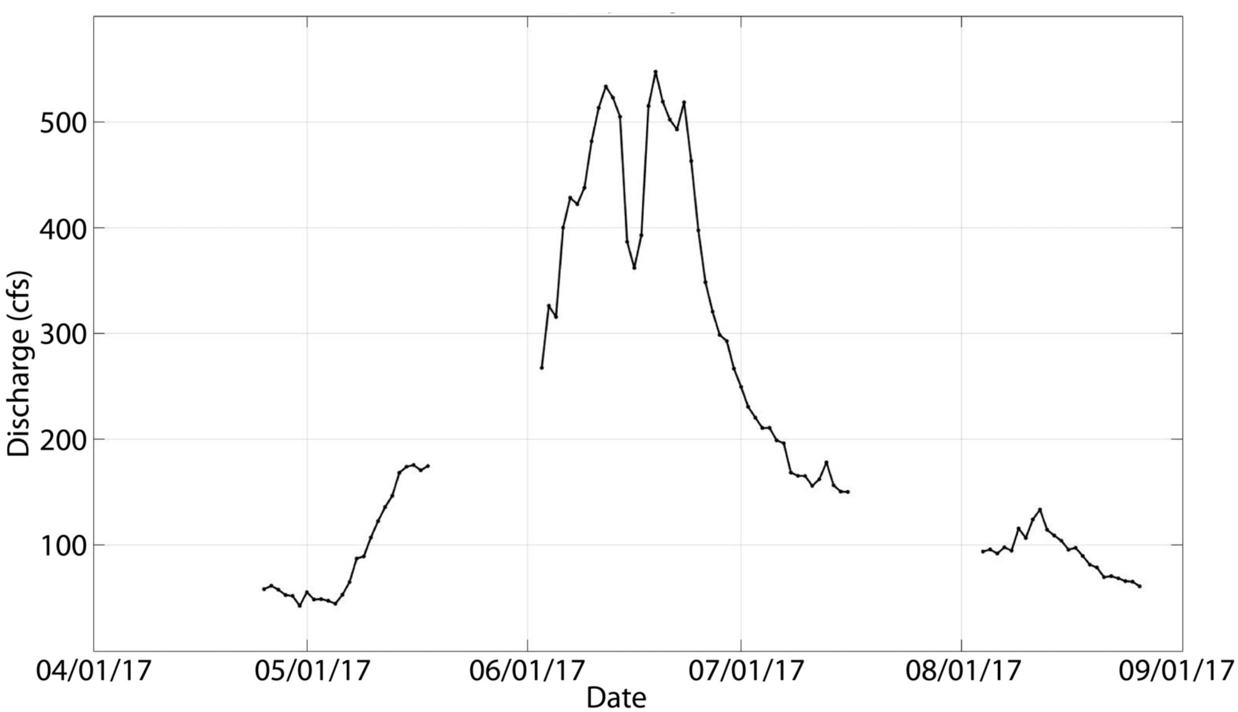


**Figure 3.5:** Measured water discharge at the NSV weir in 2017 as average daily inflow. Gaps indicate missing record.

Grain size analyses previously conducted in 2014 at seven sites across the approach channel floodplain were repeated in 2017. Comparison of the results indicate that a large distribution of grain sizes, varying from sand to cobbles, was found across the approach channel. Results from these analyses point to little change in median grain size at these locations between 2014 and 2017 (Figure 3.6).

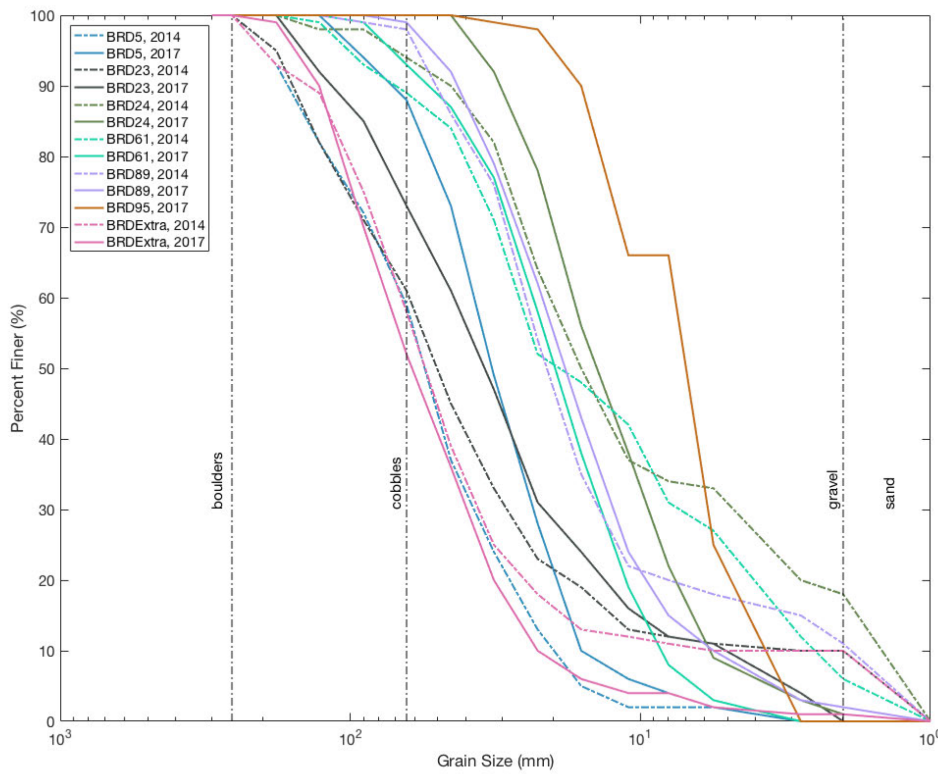


**Figure 3.6:** Grain size distribution of clasts at seven locations across the floodplain of the approach channel in 2014 and 2017.

## 3.2 Delta Bathymetry

Bathymetry surveys are compared across an area that covers 14,000 m$^2$, equal to 94% coverage of the 2017 delta plain. Change detection analysis of the bathymetric surveys indicates a net aggradation of sediment between 2014 and 2016 (years 1 and 3 post-flood), with a maximum aggradation of 11.4 m and incision of -5.8 m (Figure 3.8a). Between 2016 to 2017 (year 4), a net degradation occurred at the delta, with maximum localized aggradation of 8.4 m and incision of -3.9 m (Figure 3.8b). Field observations additionally noted the development of a knickzone near the southern extent of the delta plain during this time (location shown in Figure 3.7). Although year 4 is characterized by sediment transport out of the inlet, DEM differencing of bathymetry surveys in 2014 and 2017 indicate a net addition of 57,090 $m^3$ of sediment at the delta plain (Appendix D.16). To corroborate these results, change detection analyses were also conducted in EVS (Appendix D.17). Quantitative results from both methods of change detection analyses are specified in Table 4.1.

**Table 3.3:** Volumetric sediment changes within the delta plain and delta front between 2014 and 2017. Data includes volumetric changes calculated using the GCD tool and EVS software.

| Time Interval | Volume Eroded ($m^3$) | Volume Deposited ($m^3$) | Net Volume Moved ($m^3$) | Total Volume ($m^3$) | Max. Vert. Change (m) |
|---|---|---|---|---|---|
| Method 1: SGeMs and Geomorphic Change Detection | | | | | |
| April 2014 to April 2016 | $1,150 \pm 80$ | $68,230 \pm 2,690$ | $67,080 \pm 2,690$ | $69,380 \pm 2,770$ | 11.4, -5.8 |
| April 2016 to August 2017 | $15,630 \pm 2,270$ | $5,530 \pm 400$ | $-10,100 \pm 2,310$ | $21,160 \pm 2,680$ | 8.4, -3.9 |
| April 2014 to August 2017 | $60 \pm 30$ | $57,030 \pm 2,720$ | $56,980 \pm 2,720$ | $57,090 \pm 2,750$ | 11.9, -0.8 |
| Method 2: Earth Volumetric Studio | | | | | |
| April 2014 to April 2016 | 1,680 | 66,840 | 65,160 | 68,520 | – |
| April 2016 to August 2017 | 15,822 | 6,390 | -9,430 | 22,210 | – |
| April 2014 to August 2017 | 640 | 57,000 | 56,370 | 57,640 | – |

## 3.3 Movement of the Delta Front

Bathymetry analysis illustrates that the delta front has prograded northward into the reservoir since 2014 (Figure 3.7). Graphing the relative distance of movement with time reveals a total

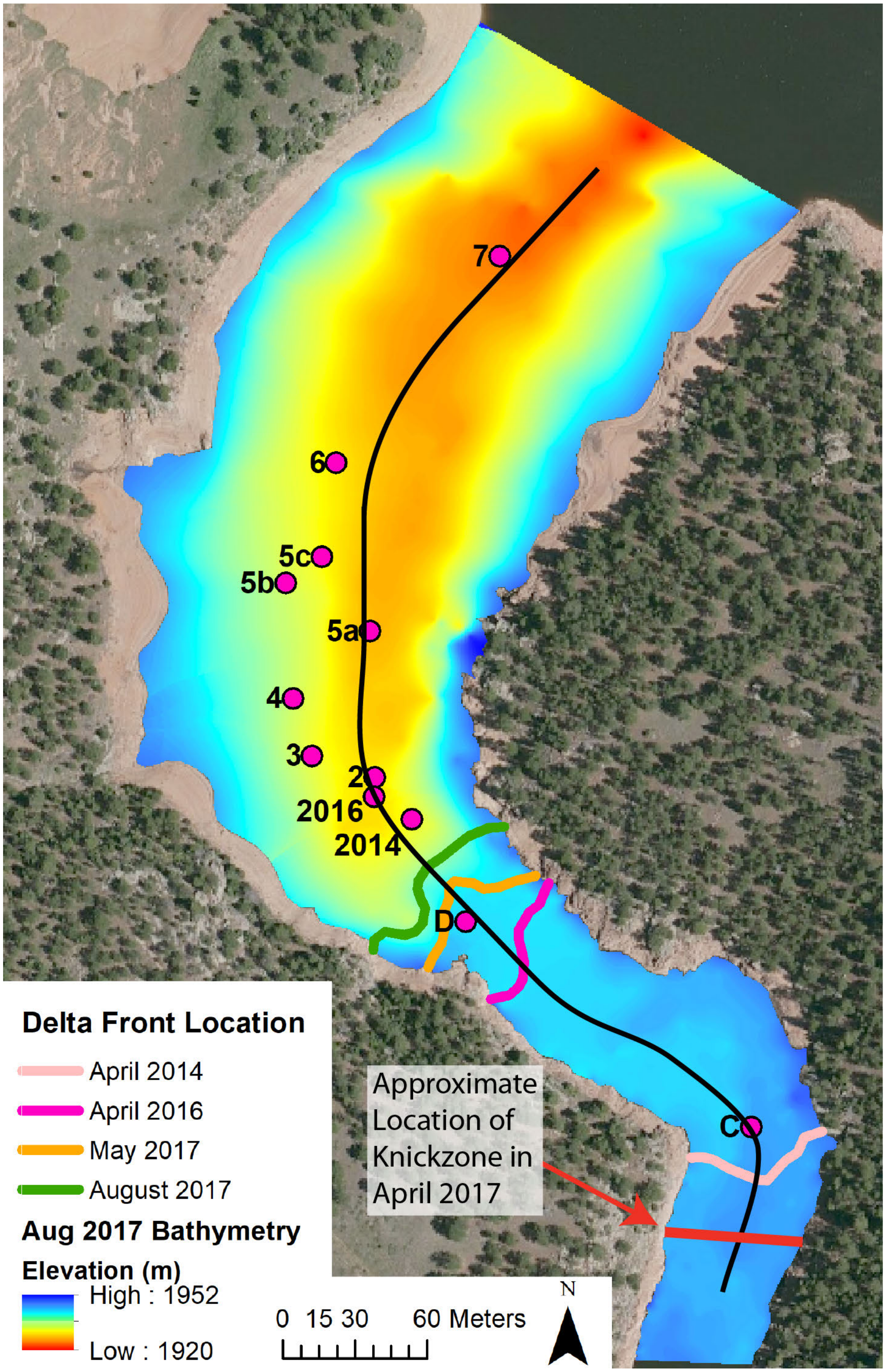


**Figure 3.7:** A Google Earth image overlaid by 2017 delta bathymetry, cores collected (dots) and locations of the delta front between 2014 and 2017. The black line indicates the location of the longitudinal profile of the delta, and the red line delineates the approximate location of the knickzone in April 2017.

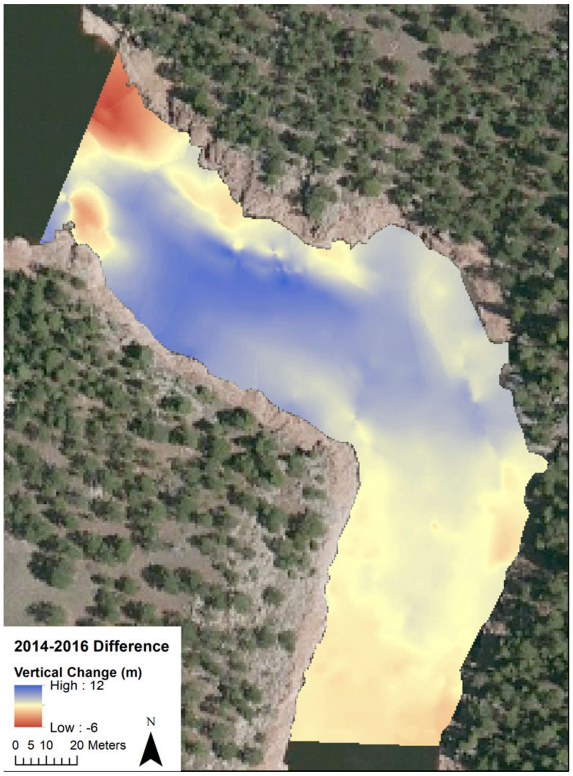


**(a)** Difference 2014-2016

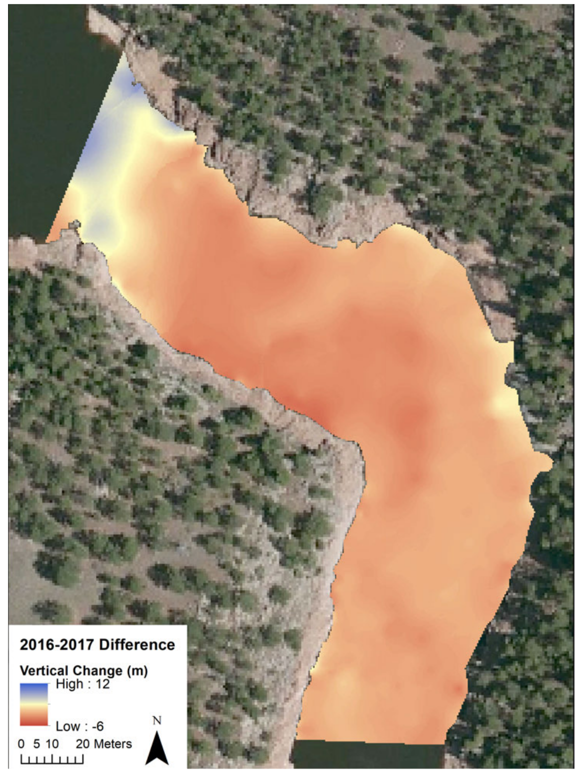


**(b)** Difference 2016-2017

**Figure 3.8:** Maps showing net vertical aggradation and degradation at the delta plain and delta front between 2014 and 2017.

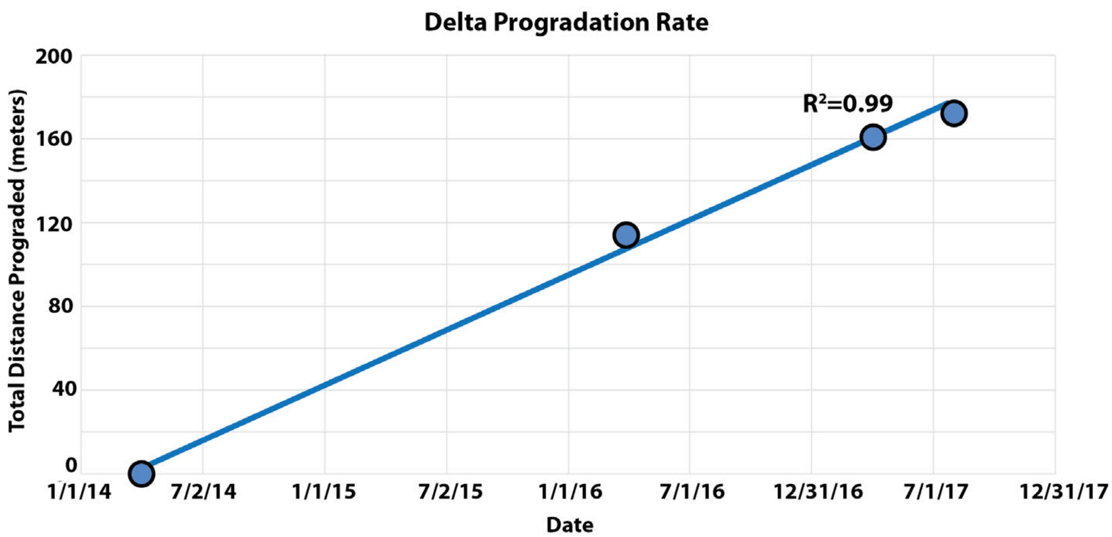


**Figure 3.9:** Distance of delta front progradation over time relative to its location in April 2014. The blue line indicates a linear regression of delta front progradation and an $R^2$ value of 0.99 indicates a consistent rate of progradation between 2014 and 2017.

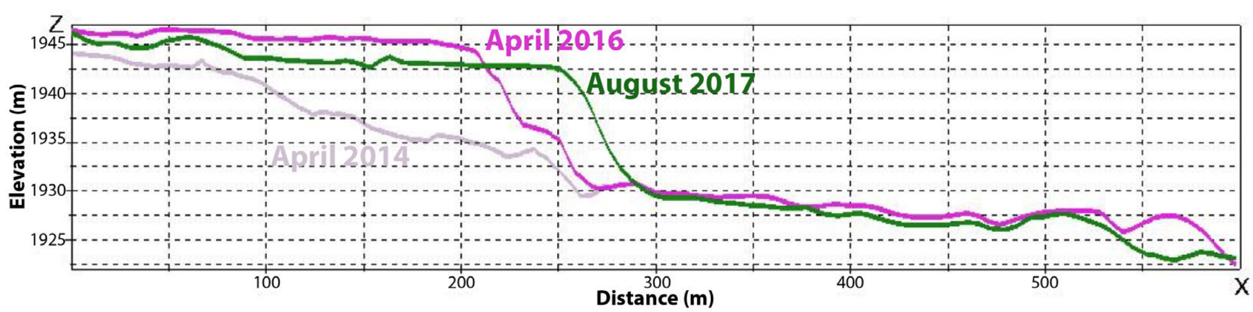


**Figure 3.10:** Changes in delta topography with time along the former NSV thalweg. The delta front was derived from the break in slope identified in each bathymetric survey.

progradation of 170 m since 2014, and a constant progradation rate of approximately 50 m/yr over the four years of analysis (Figure 3.9).

The longitudinal profile along the former NSV thalweg (black line in Figure 3.7) illustrates variations in delta geometry with time (Figure 3.10). Similar to the change detection results of the bathymetry surveys, the longitudinal profile shows that the delta plain aggraded and the delta front prograded between April 2014 and April 2016. Between April 2016 and August 2017, the elevation of the delta plain decreased between while the delta front continued to prograde. Based on the longitudinal profile, no significant changes in topography occurred within the prodelta between 2016 and 2017 (Figure 3.10).

## 3.4 Delta Sedimentation

### 3.4.1 Sediment Cores

Core data including visual changes in color, texture and grain size analysis, magnetic susceptibility, LOI, and XRF (Appendix D.13) were used to stratigraphically align the 8 cores collected in April 2017 (Figure 3.11). A visual change in sediment color from gray to tan, shift in texture from clay to homogeneous fine sand, and a spike in magnetic susceptibility were used to identify the contact between pre- and post-flood deposited sediments in 6 of the 8 cores.

Cores C and D, located upstream of the other analyzed cores were characterized by more massive and coarser sedimentary layers. This demonstrates an overall fining across the delta towards the prodelta. Results of grain size analyses from these cores are documented in Appendix D.14.

Stratigraphic layers in cores 2014 and 2016 were matched to those collected in April 2017 to temporally delineate sediment accumulation. A thick (1.25-40 cm), tan layer of homogeneous sand was found in all cores. Its stratigraphic position on top of the organic-rich, pre-flood clay, coarse median grain size (1-2 mm), and delta-wide aggradation suggests that it represents 2013 flood sedimentation. A depositional sequence of silt, organics, and clay was found in all of the cores, including the 2014 core, indicating delta-wide deposition from the flood and continued sediment input throughout the first year post-flood.

A package of gray and tan laminated sand overlain by organic silt was attributed to 2015 and 2016 sedimentation. The sandy layer pinched out, only extending to Core 5C in the prodelta, whereas the organic silt and mud layer persisted in all of the cores collected at the prodelta (Figure 3.11 and Figure 3.12). The discontinuity of the sand layer indicates lower-magnitude flows than the flood that are associated with a lower sediment transport capacity, such as those observed during 2015 and 2016 peak snowmelt discharge. Lastly, a layer of fine silt and sand only identified in the least distal cores (Cores 2, 3, and 4) from April 2017 were attributed to 2017 (year 4 post-flood) sedimentation.

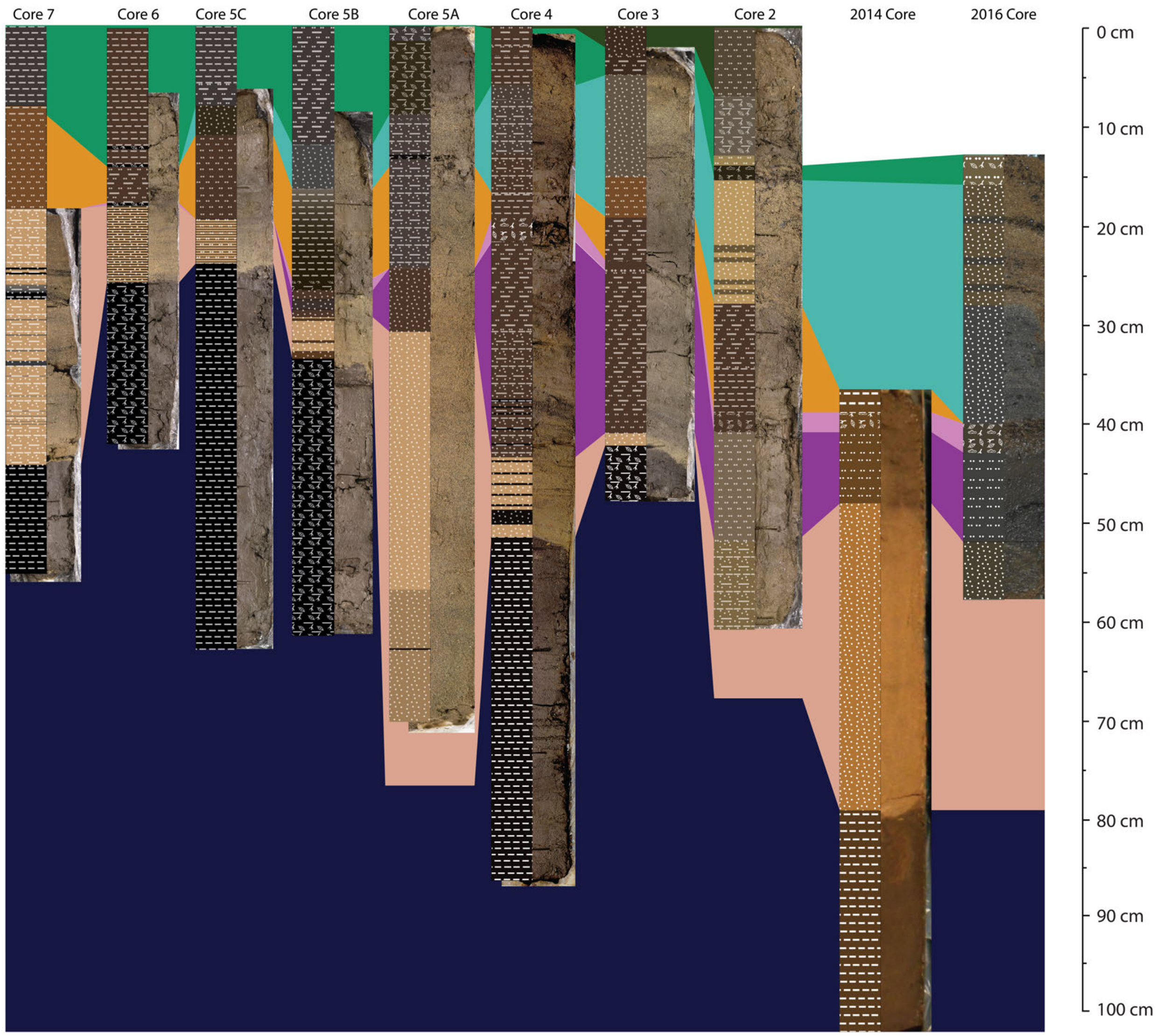


**Figure 3.11:** Images of Ralph Price Reservoir cores and stratigraphic symbols denoting changes in sediment texture. Sedimentary layers were correlated across the cores using grain size, magnetic susceptibility, LOI, and XRF data. The line that distinguishes the dark blue from the peach layer represents the pre-flood and post-flood sediment interface. Cores are oriented left to right from distal prodelta (Core 7) to near the inlet (Cores 2, 2014, and 2016). See Figure 3.7.

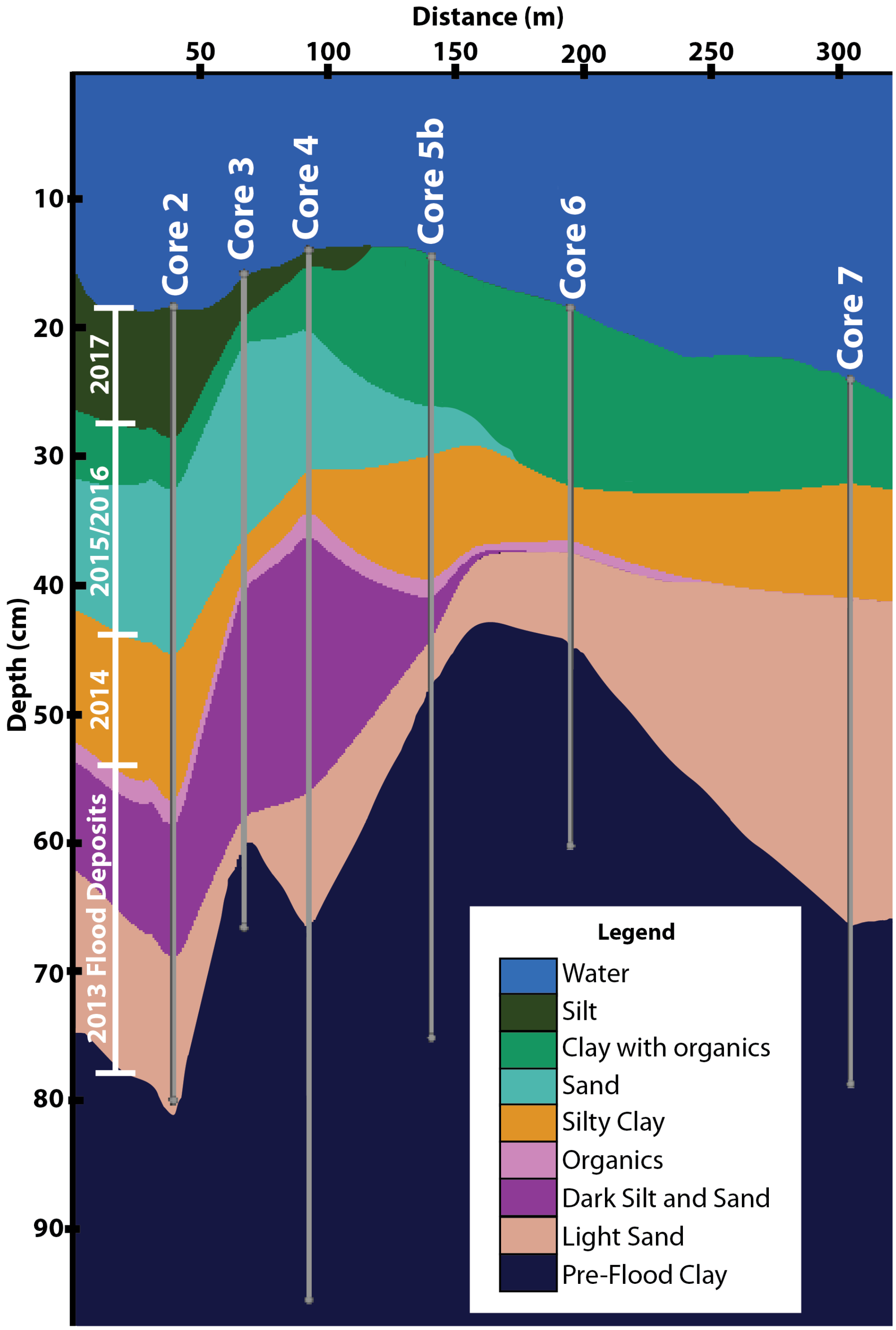


**Figure 3.12:** A longitudinal profile of the delta showing pre-flood, flood, and post-flood facies. Delta topography is exaggerated 5x, whereas core stratigraphy is exaggerated 50x to better illustrate changes in stratigraphic thickness with distance. Cores are oriented left to right, closer to the inlet (Core 2) to distal portions of the prodelta (Core 7). See Figure 3.7.

### 3.4.2 Quantifying Sedimentation on the Delta Plain

Having defined the pre- and post-flood sediment interface, sediment accumulation since the September 2013 storm was measured in the cores. Using the eight April 2017 core locations and assuming a sediment thickness of 0 m at the channel banks, measured thicknesses were kriged across the prodelta to estimate total sediment accumulation in this area (outlined in blue in Figure 2.3).

The kriged sediment thicknesses were differenced from the August 2017 bathymetry survey to produce pre-September 2013, post-flood, and August 2017 DEMs. These were compared to produce a rough estimate of sedimentation across the prodelta. Between September 2013 and April 2017, accumulation up to 0.72 m occurred throughout the prodelta, with the largest vertical aggradation in the former thalweg of the NSV channel (Figure 3.13).

Calculated bathymetry differences (2014-2017) indicate a total of 5,370$\pm$880$m^3$ of sediment was deposited within the prodelta. Deposition of approximately 3,340$\pm$50$m^3$ in the delta occurred as a result of the September 2013 flood. A summary of channel and inlet-wide sedimentation is graphically presented in Figure 3.14.

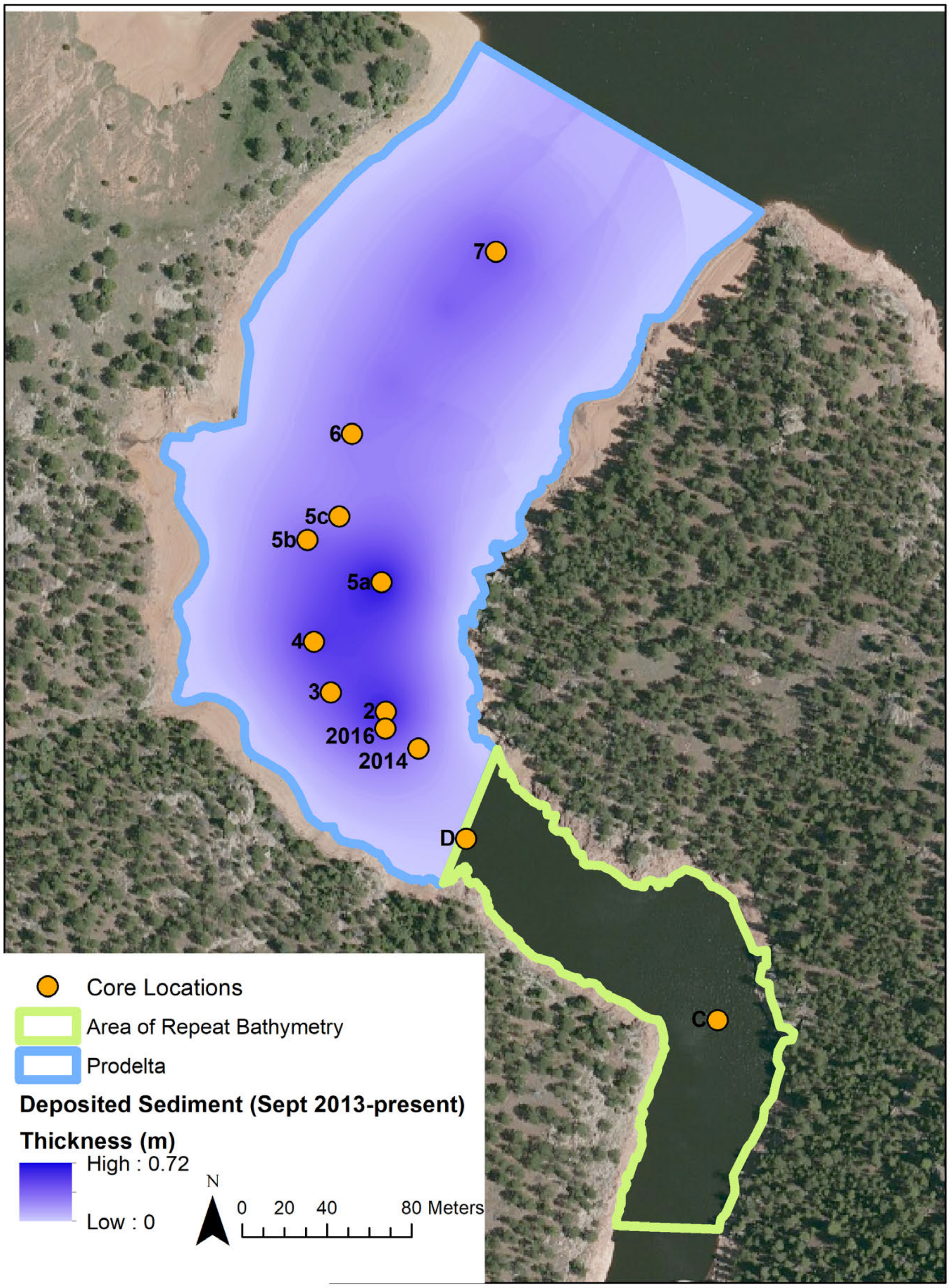


**Figure 3.13:** Total sediment accumulation in the prodelta since September 2013


**Figure 3.14:** A summary of the total volumetric change in sediment within the approach channel and reservoir delta between September 2013 and August 2017. Blue represents the volume of sediment aggradation within the analyzed area, red represents the volume of sediment eroded from the area, and black corresponds to the net change of sediment. Uncertainty is included for all estimates based on the degree of differencing output. The gray boxes show the temporal extent of the volume estimates, based on data availability.

# Chapter 4

# Discussion

Analytical results and observations at the North St. Vrain approach channel and the delta of Ralph Price Reservoir were interpreted to address research objectives and test the proposed hypotheses. I address these objectives and evaluate the hypotheses in light of my findings and apply these interpretations to form a system-wide connection between the continued impact and recovery due to flood-induced sedimentation.

## 4.1 Channel Changes

Repeat photographs of the channel immediately following the 2013 flood, and nearly 5 years after the 2013 flood, illustrate large-scale and visible channel adjustments with time (Figure 3.1). Notable initial flood impacts (shown in the photograph from November 2013) include the complete infilling of the former NSV channel into a planar (low slope) surface of unconsolidated sediment. By March 2014 (prior to the 2014 snowmelt period), a wide, shallow channel had already been formed, which is likely the result of receding limb discharges in the weeks after the flood. Although channel bed material grain size was not quantified, photographs (Figure 3.1) indicate that the approach channel initially consisted of sand and gravel.

Lisle (1982) analyzed the channel impacts of a large flood in northern California that produced an increase in sediment discharge and widespread aggradation. Lisle (1982) noted that flood-related aggradation decreased bed roughness and the median grain size. He found that these trends led to a decrease in the entrainment threshold required to transport bedload sediment, thereby increasing the mobility of particles as well as the effectiveness of moderate discharges that can trigger channel adjustments. Wohl and Cenderelli (2000) analyzed the impacts of the North Fork Poudre River in Colorado following a sediment release, which caused widespread infilling of pools with fine sediments. Results of that study indicate that 70-80% of this sediment was flushed out of the system within year 1 post-flood, with the areas closest to the sediment source scoured first (Wohl and Cenderelli, 2000).

Applying the observations from Lisle (1982) and Wohl and Cenderelli (2000) to the 2014 NSV channel, the largest changes in channel adjustments are expected to have occurred within the first year. Specifically, a decrease in the channel bed grain size (shown in the 3/21/2014 photograph) is expected to increase sediment entrainment that, according to Wohl and Cenderelli (2000), will quickly flush the fine sediments downstream. Figure 3.1 and Table 3.1 support this prediction, showing that the greatest channel change occurred after the first snowmelt runoff following the flood (between March 2014, before peak 2014 snowmelt runoff, and May 2015, after 2014 snowmelt runoff and before peak 2015 snowmelt runoff). The unconsolidated sand and gravel along the approach channel were easily entrained by 2014 snowmelt runoff, the highest peak discharge since the flood (Appendix F.1)

Channel incision between 2013 and 2015 indicates that following the flood the transport capacity exceeded sediment supply. Research on river adjustments due to channel incision notes a general trend of increased vertical incision, which triggers bank collapse and results in channel widening (Doyle et al., 2003; Pace et al., 2016). This trend is evident at my study site, and is visible in repeat photographs and field measurements, which indicate that the channel initially incised between 2013 and 2014 (up to 0.3 m), followed by continued incision and channel widening between 2014 and 2015 (up to 1.5 m). It follows that an initial decrease in grain size and resulting increase in transport capacity likely promoted channel widening within the first year following the flood. Winnowing of fines later increased the median grain size, which slowed the rate of channel change. Signs of year 1 post-flood channel widening are still preserved in the trapezoidal channel shape observed through 2018, nearly 5 years following the flood-related sedimentation event.

Between May 2015 and March 2018, evidence of continued channel change are less visually distinct. DEM differencing, however, provides insight into channel adjustments of smaller magnitude than has occurred between summer 2016 and summer 2017 (years 3 and 4). Despite discrepancies in measurement precision between RTK and SfM-produced DEMs, all change detection analyses indicate a net loss in sediment throughout the approach channel. This supports the previous finding that the years following the flood were characterized by a decrease in sediment supply and/or relatively larger transport capacity.

Channel measurements of the thalweg in 2016 and 2017 show minimal change between this time period, as large-scale adjustments to sinuosity and slope did not occur (Table 3.1). The longitudinal profile (Figure 3.2), however, indicates that localized adjustments in bed elevation and migration of riffles and pools are still on-going. Thus, nearly 5 years following the flood, channel adjustments are much lower in magnitude and more localized in extent than those that occurred within 1 year of the flood.

Overall, change detection analyses indicate limited recent signs of channel change and scouring. According to *Hypothesis 1*, the approach channel was predicted to show vertical incision and riverbank-toe undercutting. On-going incision was predicted to cause an increase in bank height and slope and eventually lead to continued bank collapse and channel widening (an increase in the width:depth ratio). Although predictions of widespread channel incision and bank collapse did occur between 2013 and 2014, the width:depth ratio decreased (counter to that predicted in *Hypothesis 1*), and changes in slope (0.008 m/m) and sinuosity (1.5) did not occur in 2016 and 2017. As a result, *Hypothesis 1* is not supported.

Areas where bank erosion did occur were limited to the outer banks of meander bends ('Points B' in Figure 3.3). Outer bank retreat occurs naturally in channels, as the largest-magnitude flows associated with the highest shear stresses occur at the far bank of bends and promote erosion (Simon et al., 2000). Secondary helical flows further move eroded sediment towards the inner bank, increasing efficiency of bank erosion (Simon et al., 2000). In 2016 and 2017 erosion was largely limited to the outer banks, which suggests that the approach channel has adjusted to snowmelt flows, whereas on-going changes reflect natural river processes commonly observed at unconfined meander bends.

The largest channel change that occurred between 2016 and 2017 took place at a confined meander bend, where outer bank bedrock confinement likely promoted erosion of the inner meander bend (‘Point A’ in Figure 3.3). Madej et al. (2009) found that channel adjustments at narrow and confined areas occurred more through changes in bed elevation via aggradation and erosion than modifications in sinuosity, whereas expansive floodplain adjustments primarily occurred through changes in both bed elevation and sinuosity. Similar to Madej et al. (2009)’s findings, erosion at the confined bedrock bend (‘Point A’ in Figure 3.3) largely occurred through vertical incision (Figure 3.2). Increased incision due to confinement thus likely led to adjustment via bank collapse of the unconsolidated and unconfined inner bend. Google Earth satellite images (Figure 3.4) indicate that pool incision triggered bank collapse during 2017 peak snowmelt discharge. As a result, channel adjustment between 2016 and 2017 was driven by a combination of an increase in water discharge and local channel confinement.

When evaluating the overall changes to the approach channel between 2016 and 2017, it is relevant to consider the nature of the channel response. Are ongoing channel adjustments due to continued recovery from the 2013 flood, due to a change in downstream reservoir base level, or rather due to local site-specific variability of the channel? Analyses of the NSV approach channel indicate that the largest channel adjustments from flood sedimentation occurred within the first year after the flood. Based on previous literature, a drop in base level would have produced upstream bed incision which, at a reach scale, was not observed (Figure 3.2). Further, the knickzone produced by the drop in base level was observed downstream of the approach channel. According to Pace et al. (2016) and Doyle et al. (2003), little channel adjustment occurs upstream of the knickzone, further supporting this conclusion. With this in mind, channel changes between 2016 and 2017 were caused by upstream changes in discharge, river sinuosity, and bank collapse in response to local confinement at meander bends (*Objective 1*). The magnitude of these changes, however, was much less than those observed within the first year of flood recovery. Although predictions on *Hypothesis 1* were largely supported with regards to channel recovery after a sedimentation event, these adjustments were observed within the first year of recovery, but are no longer measurable at an annually detectable rate and magnitude. These conclusions are also supported by other literature, which has documented the majority of channel recovery after sedimentation events to occur within the initial 2-3 years following a disturbance (Wohl and Cenderelli, 2000; Rathburn et al., 2018).

## 4.2 Remobilization of Delta Sediment

### 4.2.1 2014-2016 Delta Aggradation

The longitudinal profile along the former channel of the NSV (Figure 3.10) and bathymetric differencing indicates that initial system recovery and upstream channel adjustments between 2014 and 2016 are associated with both vertical aggradation of the delta plain and progradation of the delta front (*Objective 2*). Comparing initial delta sedimentation to that between 2016 and 2017 indicates a difference in sediment source. Whereas within the initial 2 years after the flood upstream channel adjustment produced additional sedimentation at the delta, continued lower discharges (after the flood) were expected to promote winnowing of fine flood sediments and decrease the flux of sediment into the delta with time. Such a decrease would be expressed by a reduction in the rate of delta progradation and aggradation (*Hypothesis 2a*). However, between 2016 and 2017 the rate of delta progradation remained constant and therefore this element of *Hypothesis 2a* is not supported.

### 4.2.2 Impacts of a Base Level Drop

Existing literature has identified a typical sequence of channel changes through channel evolution models (e.g. Schumm et al. (1984)) that occur in response to dam removal–an event analogous to base level lowering. Doyle et al. (2003), for example, studied 2 dam removals in southern Wisconsin to examine relative rates of channel response of fine- and coarse-grained rivers following base level lowering. Based on their analysis, Doyle et al. (2003) created a 6-stage sequence that defined trends of channel evolution. According to their model, base level lowering initiates upstream erosion and channel incision, which acts to create a headcut and produce a constricted channel. This in turn increases flow velocity in the channel and enhances vertical incision and mass-wasting of banks. With an ensuing increase in sediment remobilization and reduction of the local energy slope, continued channel widening and downstream aggradation occur.

According to this model, a drop in base level at Ralph Price Reservoir would have produced a knickzone or headcut and promoted channel incision downstream of the knickzone (e.g. across the delta plain). Field observations identified the development of a knickzone at the southern extent of the delta plain, which suggests that incision in 2016 and 2017 did occur due to a drop in base level (supporting *Hypothesis 2b*). The 2016 and 2017 bathymetric differencing confirms this channel response, indicating widespread vertical incision at the delta plain comparable in volume to sediment aggradation at the delta front (Figure 4.1). This suggests that delta plain incision, sediment remobilization, and delta progradation in 2016 and 2017 were likely a response to a drop in base level and represent the first time since the flood that processes shifted from aggradation to erosion. Such a response provides further evidence for why the delta progradation rate between 2016 and 2017 remained higher than expected, and did not decrease. Currently, with a return to typical reservoir level conditions, delta plain incision is expected to cease and sediment remobilization at the delta is predicted to decrease. It follows that a decrease in sediment remobilization will be reflected by a decreased rate in progradation of the delta front. To fully evaluate *Hypothesis 2a*, an additional survey in August 2018 will be conducted to test this prediction.

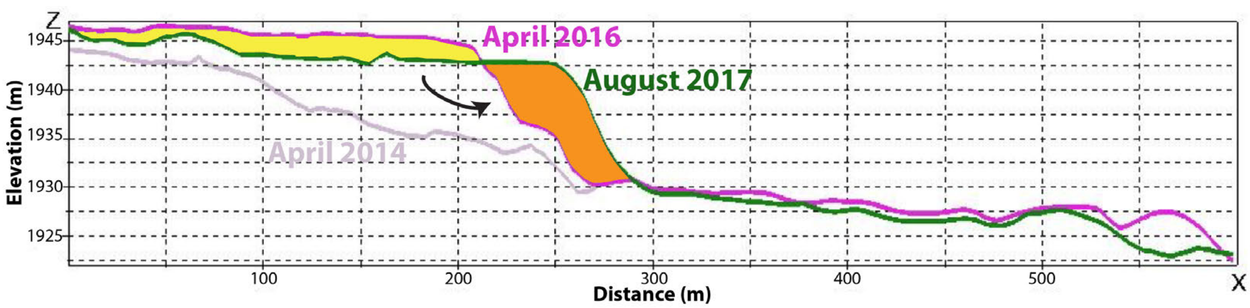


**Figure 4.1:** A figure of delta channel evolution, highlighting a comparable volume of incision at the delta plain and sediment deposition at the delta front between 2016 and 2017

Prodelta stratigraphy in the reservoir cores indicates that fine to medium sand (the coarser fraction in the cores) has not been deposited across the prodelta since the flood. In fact, sediment layers deposited in 2015 and 2017 pinch out with distance towards the more distal end of the delta. This suggests that, although spring snowmelt discharges do produce an influx of sediment into the delta, sediment deposition is minimal and largely occurs closer to the delta front. As a result, the delta plain is expected to continue to aggrade, but at a decreased progradation rate with time.

## 4.3 Channel-Delta Sediment Budget

In this research, I evaluated the assumption that sediment fluxes in the delta directly correlate to upstream changes to the approach channel (*Objective 3, Hypothesis 3*). If this holds, geomorphic change analysis will produce a sediment budget in which the volume of sediment transported out of the approach channel will balance delta aggradation since the flood.

DEM differencing through RTK and SfM data demonstrate that between 2016 and 2017 the approach channel had a net loss of sediment. The most accurate differencing calculations, however, estimate erosion of 890±350 $m^3$ from the approach channel between 2016 and 2017. This value is one order of magnitude smaller than the measured volume of sediment aggradation of 5,530±400 $m^3$ across the delta plain in 2016 and 2017. This finding supports *Objective 2*, which relates sediment deposition in the delta to both upstream sediment input and sediment remobilization at the delta. *Hypothesis 3* is therefore not supported, however, as the volume of sediment eroded and transported out of storage along the approach channel does not equal the volume of sediment deposited at the reservoir delta.

These results demonstrate that the sediment budget at the analyzed study area cannot be closed, and additional sediment sources must be taken into account. One possible reason for the unbalanced budget is the omission of sediment deposited and remobilized in the backwater area (shown in Figure 1.1b). Here the NSV becomes ponded at the most upstream extent of the reservoir, which leads to a decrease in flow velocity and promotes sediment deposition. Due to large quantities of floating wood at this area, repeat bathymetric surveys in the backwater area could not be conducted. As a result, this sediment budget, where inflow is represented by channel erosion and outflow is calculated by delta deposition, may be imbalanced because it does not include the backwater area.

## 4.4 Cumulative Sediment Volumes

DEM differencing between 2014 and 2016 indicate that incision occurred at the southern end of the delta plain, whereas significant sediment aggradation took place at the northern half of the analyzed area. In contrast, this same area is characterized by widespread incision the following year (2016-2017). Comparing these surveys shows that the flood and ensuing drop in base level enhanced the translation of a sediment pulse into the reservoir.

Assuming that 1957 (pre-flood and pre-dam) channel slope represented equilibrium conditions, minimal channel changes at a much shallower channel slope suggests that the flood induced a system shift to a new baseline condition (Rathburn et al., 2018). As a result, the NSV is not expected recover to pre-disturbance conditions within a management time frame. Minimal change in median grain size between 2014 and 2017 further suggests that overbank flows that act to remobilize and flush out fine sediments have not occurred outside of the current channel since the flood. This highlights that the channel is adjusted and temporally defined by annual snowmelt runoff (Appendix G), but a large volume of unconsolidated sediment still remains in storage. Analyses since the flood have quantified the cumulative volume of sediment added to the reservoir and resulting loss in water storage capacity since the 2013 flood.

Previous analyses found that the September 2013 flood remobilized approximately 500,000 $m^3$ of sediment. Of this total volume, a total of 289,200 $m^3$ of sediment was deposited into the reservoir, of which 11% was (31,000 $m^3$) deposited on the delta (Rathburn et al., 2017). After the storm, 258,200 $m^3$ of sediment remained stored at the approach channel (Rathburn et al., 2017). Since 2014, an additional volume of 74,000 $m^3$ has been deposited on the delta plain, accounting for approximately 29% of the total volume of sediment (289,200 $m^3$) initially stored in the approach channel (Table 4.1). Analyzing the decrease in volumetric deposition on the delta plain supports *Hypothesis 2a* (Figure 4.2), but as mentioned previously, this will need to be confirmed by an additional bathymetric survey in August 2018. A drop in base level between 2016 and 2017 enhanced sediment remobilization to the prodelta and decreased volumetric aggradation of the delta plain to 6,000 $m^3$ (Figures 4.2 and 4.3). Because sediment deposition at the prodelta during the drop in

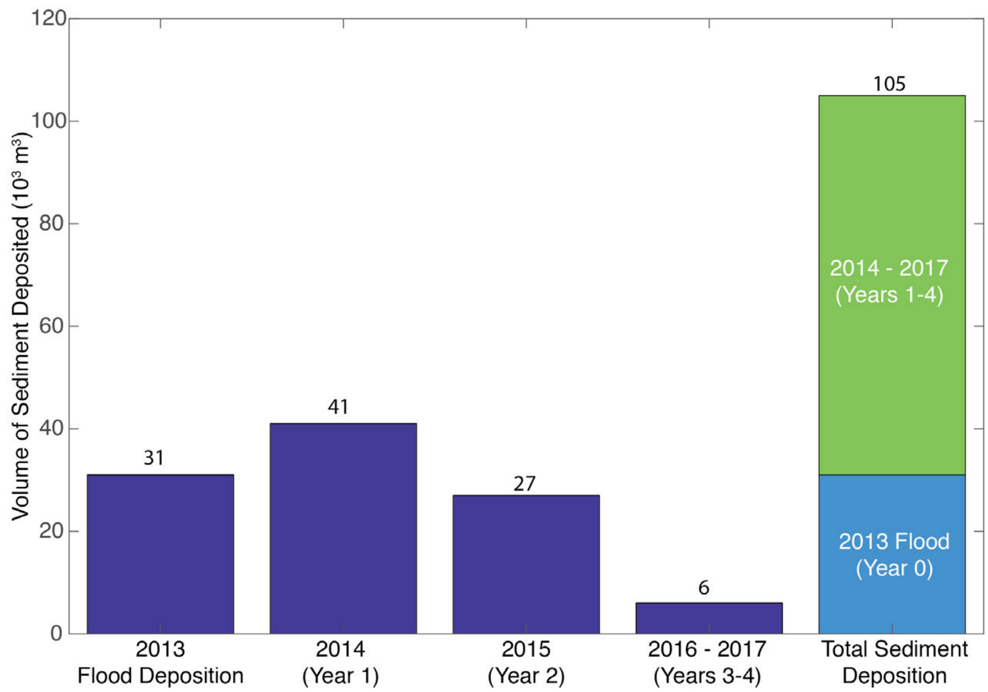


**Figure 4.2:** Volume of sediment deposited at the delta by year since the September 2013 flood. Sediment accumulation rates for 2013 and 2014 were provided by the City of Longmont and documented by Rathburn et al. (2017)

.

base level largely reflected sediment remobilized from the delta plain, accumulation at the prodelta during this time period was not incorporated into total sediment accumulation estimates.

Assuming a 1:1 ratio of sediment to water displacement, sediment deposition since 2014 accounts for an additional 0.4% loss in total water storage capacity since the flood. Although limited changes to the upstream approach channel since 2015 suggest that upstream flood sediments will remain in storage, it is important to consider the potential of future storms and floods.

Channel incision and development within the first year following the flood was fast in rate and magnitude (Figure 4.3). By 2015, the approach channel had evolved to accommodate snowmelt flows. Results of this research indicate that approximately 57% of the initial sediment deposited in the approach channel (equivalent to 148,000 m$^3$) in September 2013 remains upstream in storage. As discussed earlier (Wolman and Gerson, 1978; Brunsden and Thornes, 1979; Magilligan et al., 1998), it is important to consider antecedent geomorphic events when predicting future morphological changes. It follows that, although typical snowmelt runoff discharges do not appear to be

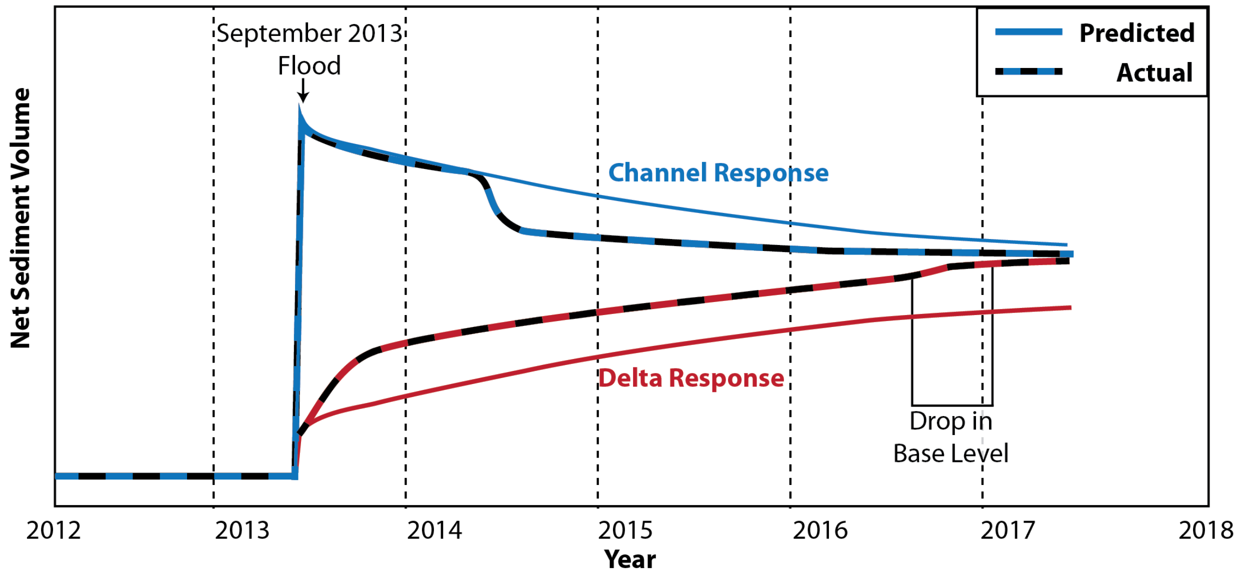


**Figure 4.3:** A conceptual model illustrating the relative predicted change and the actual change in volume of the approach channel and delta with time since the September 2013 flood.

**Table 4.1:** Calculated volume of remobilized sediment at the approach channel and reservoir delta between 2014 and 2017.

| Time Interval | Volume ($m^3$) | Percent of Volume in Upstream Storage After Flood |
|---|---|---|
| Flood-Induced Delta Deposition | 31,000 | – |
| Deposition Between 2014 and 2017 | 74,000 | 29% |
| Approximate Volume Remaining in Upstream Storage | 184,000 | 71% |

producing significant influxes of sediment into the reservoir, future floods lower in magnitude than September 2013 that either cause channel avulsion or overtop the current channel banks would likely trigger large-magnitude sediment fluxes. If the remainder of sediment stored upstream were transported by future floods, the reservoir could lose an additional 0.9% in total water storage capacity.

# Chapter 5

# Conclusion

Scientific understanding of how rivers change in response to large storms, floods, and sedimentation events remains poorly understood due to variability of research areas, limitations in the temporal scope of analysis, and poor resolution of data. Understanding these responses, however, is a necessary component for improving river management and restoration practices, maintaining river ecosystem diversity, and incorporating policies to increase the resiliency of society in the face of future climate extremes (Magilligan et al., 1998; Naylor et al., 2017).

I analyzed the flood response of NSV Creek and the Ralph Price Reservoir delta using photogrammetry-, surveying-, geostatistical-, and core analyses. Multi-year analyses of the approach channel indicate that the largest channel response occurred in 2014, 1 year following the flood. By 2015, erosion and channel widening had carved a trapezoidal channel that persists in 2018. Additional channel measurements confirm that channel dimensions (width:depth), sinuosity, and slope have minimally changed between 2015 and 2017. Surveying analyses indicate that channel adjustments between 2016 and 2017 were limited to minimal lateral migration of unconfined meander bends, as well as local incision and channel widening that occured at confined reaches during peak snowmelt flows.

Bathymetry analyses indicate that the 2014 sediment flux associated with upstream channel adjustments led to aggradation of the delta plain and progradation of the delta front. I noted a non-linear decrease in total sediment accumulation and a self-dampening response, which was interrupted by base level lowering in 2016. The base level lowering produced incision of 15,000 $m^3$ at the delta plain and a delta front progradation rate of 50 m per year. A return to normal conditions of the reservoir are expected to result in continued but decreasing sediment aggradation at the delta plain and a decrease in the rate of delta front progradation.

I found that sediment movement from the approach channel is not easily linked to sediment deposition at the reservoir delta. This discrepancy may be due to unquantified sediment accumulation in the backwater area of the reservoir. This volumetric discrepancy highlights the challenge of quantifying total sediment erosion and deposition.

Since 2014, a minimum of 74,000 $m^3$ of sediment has been deposited across the delta, leading to a loss of approximately 0.4% in total reservoir storage capacity. Based on these calculations a total of 184,000 $m^3$ remains in storage upstream of the reservoir. Although the channel appears to have adjusted to the average snowmelt runoff since the flood, future above-average discharges have the potential to entrain and transport large volumes of sediment into the reservoir and cause an additional loss of up to 0.9% of total reservoir storage capacity. Ongoing storage of sediment upstream from the reservoir indicates the potential for additional sediment to be transported during future events.

## 5.1 Future Work

Despite the progress made throughout this research, additional analyses will enhance our capability to predict future sediment fluxes and channel adjustments in response to large sedimentation events. This study tracks the movement of sediment into the delta ranging in size from coarse sand to clay, however, limited analysis of larger grain size movement within the channel was conducted. Transport of larger clasts (45 mm - 255 mm) is being investigated using >300 radiofrequency ID (RFID) tagged clasts placed on the channel bed of NSV Creek in April 2017. So far, 1 year of tracking data have been collected in this separate but related research.

Results of this study and the ongoing RFID analysis may also better parameterize and improve morphodynamic models. Sediment transport analyses coupled with documented changes in channel geometry and discharge can be incorporated to better predict entrainment and movement of sediment particles.

Finally, in this study discharge measurements were only recorded during daylight hours between April 2017 and August 2017. Collecting discharge measurements over the course of multiple years and throughout the day will further enhance understanding of daily and annual discharge variability at the NSV. Currently, stage is being continuously measured at the NSV weir over the

2018 snowmelt hydrograph. Better documentation of discharge variability may further enhance sediment transport predictions and morphodynamic model calculations that incorporate different hydrograph scenarios.

# Bibliography


Anderson, S. W., S. P. Anderson, and R. S. Anderson (2015). Exhumation by debris flows in the 2013 Colorado front range storm. *Geology 43*(5), 391–394.

Balog, J. (1980). Comment on 'Colorado Big Thompson flood: geologic evidence of a rare hydrologic event'. *Geology 8*(1), 9.

Blizard, C. R. and E. E. Wohl (1998). Relationships between hydraulic variables and bedload transport in a subalpine channel, Colorado Rocky Mountains, U.S.A. *Geomorphology 22*(3-4), 359–371.

Braddock, W. A. and J. Cole (1990). Geologic map of Rocky Mountain National Park and vicinity, Colorado: U.S. Geological Survey Map I-1973, scale 1:50,000.

Brunsden, D. and J. B. Thornes (1979). Landscape sensitivity and change. *Transactions of the Institute of British Geographers 4*(4), 463.

Buraas, E. M., C. E. Renshaw, F. J. Magilligan, and W. B. Dade (2014). Impact of reach geometry on stream channel sensitivity to extreme floods. *Earth Surface Processes and Landforms 39*(13), 1778–1789.

Church, M. and R. I. Ferguson (2015). Morphodynamics: Rivers beyond steady state. *Water Resources Research 51*(4), 1883–1897.

Coats, R., L. Collins, J. Florsheim, and D. Kaufman (1985). Channel change, sediment transport, and habitat in a coastal stream: effects of an extreme event fish. *Environmental Management 9*(1), 35–48.

Coe, J. A., J. W. Kean, J. W. Godt, R. L. Baum, E. S. Jones, D. J. Gochis, and G. S. Anderson (2014). New insights into debris-flow hazards from an extraordinary event in the Colorado Front Range. *GSA Today 24*(10), 4–10.

Dietrich, J. T. (2017, feb). Bathymetric Structure-from-Motion: extracting shallow stream bathymetry from multi-view stereo photogrammetry. *Earth Surface Processes and Landforms 42*(2), 355–364.

Doyle, M. W. and J. M. Harbor (2003). A scaling approximation of equilibrium timescales for sand-bed and gravel-bed rivers responding to base-level lowering. *Geomorphology 54*(3-4), 217–223.

Doyle, M. W. and F. Shields (2000, sep). Incorporation of bed texture into a channel evolution model. *Geomorphology 34*(3-4), 291–309.

Doyle, M. W., E. H. Stanley, and J. M. Harbor (2003). Channel adjustments following two dam removals in Wisconsin. *Water Resources Research 39*(1), 1–15.

Dust, D. and E. Wohl (2012). Conceptual model for complex river responses using an expanded Lane's relation. *Geomorphology 139-140*, 109–121.

East, A. E., G. R. Pess, J. A. Bountry, C. S. Magirl, A. C. Ritchie, J. B. Logan, T. J. Randle, M. C. Mastin, J. T. Minear, J. J. Duda, M. C. Liermann, M. L. Mchenry, T. J. Beechie, and P. B. Shafroth (2015). Large-scale dam removal on the Elwha River , Washington , USA : River channel and fl oodplain geomorphic change. *Geomorphology 228*, 765–786.

Finkenbinder, M. S., M. B. Abbott, M. E. Edwards, C. T. Langdon, B. A. Steinman, and B. P. Finney (2014). A 31,000 year record of paleoenvironmental and lake-level change from Harding Lake, Alaska, USA. *Quaternary Science Reviews 87*, 98–113.

Florsheim, J. L., J. F. Mount, and A. Chin (2008). Bank erosion as a desirable attribute of rivers. *BioScience 58*(6), 519.

Fryirs, K. A. (2017). River sensitivity: a lost foundation concept in fluvial geomorphology. *Earth Surface Processes and Landforms 42*(1), 55–70.

Gedye, S., R. Jones, W. Rinner, B. Ammann, and F. Oldfield (2000). The use of mineral magnetism in the reconstruction of fire history: a case study from Lago di Origlio, Swiss Alps. *Paleography, Paleoclimatology, Palaecology 164*, 101–110.

Gochis, D., R. Schumacher, K. Friedrich, N. Doesken, M. Kelsch, J. Sun, K. Ikeda, D. Lindsey, A. Wood, B. Dolan, S. Matrosov, A. Newman, K. Mahoney, S. Rutledge, R. Johnson, P. Kucera, P. Kennedy, D. Sempere-Torres, M. Steiner, R. Roberts, J. Wilson, W. Yu, V. Chandrasekar, R. Rasmussen, A. Anderson, B. Brown, D. Gochis, R. Schumacher, K. Friedrich, N. Doesken, M. Kelsch, J. Sun, K. Ikeda, D. Lindsey, A. Wood, B. Dolan, S. Matrosov, A. Newman, K. Mahoney, S. Rutledge, R. Johnson, P. Kucera, P. Kennedy, D. Sempere-Torres, M. Steiner, R. Roberts, J. Wilson, W. Yu, V. Chandrasekar, R. Rasmussen, A. Anderson, and B. Brown (2015, sep). The great colorado flood of September 2013. *Bulletin of the American Meteorological Society 96*(9), 1461–1487.

Gregory, K. and J. Lewin (2015, dec). Making concepts more explicit for geomorphology. *Progress in Physical Geography 39*(6), 711–727.

Hooke, J. M. (2007). Complexity, self-organisation and variation in behaviour in meandering rivers. *Geomorphology 91*(3-4), 236–258.

Hooke, J. M. (2015). Variations in flood magnitude-effect relations and the implications for flood risk assessment and river management. *Geomorphology 251*, 91–107.

Houck, K. (2014). Memo: CDOT/CWCB hydrology investigation phase one – 2013 flood peak flow determinations. Technical report.

Krapesch, G., C. Hauer, and H. Habersack (2011). Scale orientated analysis of river width changes due to extreme flood hazards. *Natural Hazards and Earth System Sciences 11*(8), 2137–2147.

Lane, E. W. (1955). The importance of fluvial morphology in hydraulic engineering. *American Society of Civil Engineer, Proceedings 81*(745), 1–17.

Lane, S. N. (2013, jan). 21st century climate change: where has all the geomorphology gone? *Earth Surface Processes and Landforms 38*(1), 106–110.

Lisle, T. E. (1982). Effects of aggradation and degradation on riffle-pool morphology in natural gravel channels, Northwestern California. *Water Resources Research 18*(6), 1643–1651.

Madej, M. A., D. G. Sutherland, T. E. Lisle, and B. Pryor (2009). Channel responses to varying sediment input: A flume experiment modeled after Redwood Creek, California. *Geomorphology 103*, 507–519.

Magilligan, F. J., E. M. Buraas, and C. E. Renshaw (2014). The efficacy of stream power and flow duration on geomorphic responses to catastrophic flooding. *Geomorphology 228*, 175–188.

Magilligan, F. J., K. H. Nislow, B. E. Kynard, and A. M. Hackman (2016). Immediate changes in stream channel geomorphology, aquatic habitat, and fish assemblages following dam removal in a small upland catchment. *Geomorphology 252*, 158–170.

Magilligan, F. J., J. D. Phillips, L. A. James, and B. Gomez (1998). Geomorphic and sedimentological controls on the effectiveness of an extreme flood. *The Journal of Geology 106*(1), 87–96.

Montgomery, D. R. and J. M. Buffington (1997, may). Channel-reach morphology in mountain drainage basins. *Geological Society of America Bulletin 109*(5), 596–611.

Moody, J. A. (2017). Residence times and alluvial architecture of a sediment superslug in response to different flow regimes. *Geomorphology 294*(April), 40–57.

Naylor, L. A., T. Spencer, S. N. Lane, S. E. Darby, F. J. Magilligan, M. G. Macklin, and I. Möller (2017). Stormy geomorphology: geomorphic contributions in an age of climate extremes. *Earth Surface Processes and Landforms 42*(1), 166–190.

Newson, M. (1980, jan). The geomorphological effectiveness of floods—a contribution stimulated by two recent events in mid-wales. *Earth Surface Processes 5*(1), 1–16.

Pace, K. M., D. Tullos, C. Walter, S. Lancaster, and C. Segura (2016). Sediment pulse behaviour following dam removal in gravel-bed rivers. *River Research and Applications 33*(1), 102–112.

Pizzuto, J. (2002). Effects of dam removal on river form and process. *BioScience 52*(8), 683–691.

Pizzuto, J. E. (1994). Channel adjustments to changing discharges, Powder River, Montana. *Geological Society of America Bulletin 106*(11), 1494–1501.

Randle, T. J., J. A. Bountry, A. Ritchie, and K. Wille (2015). Large-scale dam removal on the Elwha River, Washington, USA: Erosion of reservoir sediment. *Geomorphology 246*, 709–728.

Rathburn, S., G. Bennett, E. Wohl, C. Briles, B. McElroy, and N. Sutfin (2017, jun). The fate of sediment, wood, and organic carbon eroded during an extreme flood, Colorado Front Range, USA. *Geology 45*(6), 499–502.

Rathburn, S. L., S. Shahverdian, and S. Ryan (2018). Post-disturbance sediment recovery: Implications for watershed resilience. *Geomorphology 305*, 61–75.

Schumm, S. A., M. D. Harvey, and C. C. Watson (1984). *Incised channels : morphology, dynamics, and control*. Water Resources Publications.

Scott, K. M. and G. C. Gravlee (1968). Flood surge on the Rubicon River, California hydrology, hydraulics and boulder transport. *Geological Survey Professional Paper 422-M*, 1–38.

Simon, A. (1992, aug). Energy, time, and channel evolution in catastrophically disturbed fluvial systems. *Geomorphology 5*(3-5), 345–372.

Simon, A., A. Curini, S. E. Darby, and E. J. Langendoen (2000). Bank and near-bank processes in an incised channel. *Geomorphology 35*(3-4), 193–217.

Simon, A. and M. Rinaldi (2006, sep). Disturbance, stream incision, and channel evolution: The roles of excess transport capacity and boundary materials in controlling channel response. In *Geomorphology*, Volume 79, pp. 361–383. Elsevier.

Tamminga, A. D., B. C. Eaton, and C. H. Hugenholtz (2015, sep). UAS-based remote sensing of fluvial change following an extreme flood event. *Earth Surface Processes and Landforms 40*(11), 1464–1476.

USGS (1957). Raymond, CO NW/4 Boulder 15' Quadrangle.

Wheaton, J. M., J. Brasington, S. E. Darby, and D. A. Sear (2010). Accounting for uncertainty in DEMs from repeat topographic surveys: Improved sediment budgets. *Earth Surface Processes and Landforms 35*(2), 136–156.

Wicherski, W., D. P. Dethier, and W. B. Ouimet (2017). Erosion and channel changes due to extreme flooding in the Fourmile Creek catchment, Colorado. *Geomorphology 294*, 87–98.

Wieczorek, G. F. and T. Glade (2005). Climatic factors influencing occurrence of debris flows. In *Debris-flow hazards and related phenomena*, pp. 325–362. Heidelberg: Springer, Berlin.

Wohl, E., J. N. Kuzma, and N. E. Brown (2004). Reach-scale channel geometry of a mountain river. *Earth Surface Processes and Landforms 29*(8), 969–981.

Wohl, E. E. and D. A. Cenderelli (2000). Sediment deposition and transport patterns following a reservoir sediment release. *Water Resources Research 36*(1), 319–333.

Wolman, M. G. and R. Gerson (1978). Relative scales of time and effectiveness of climate in watershed geomorphology. *Earth Surface Processes 3*, 189–208.

Wolman, M. G. and J. P. Miller (1960, jan). Magnitude and frequency of forces in geomorphic processes. *The Journal of Geology 68*(1), 54–74.

Yochum, S. E. (2015). Colorado Front Range Flood of 2013: peak flows at flood frequencies. In *3rd Joint Federal Interagency Conference on Sedimentation and Hydrologic Modeling*, pp. 537–548.

# Appendix A

# Additional Flood Information at Button Rock Preserve

Ralph Price Reservoir, which is fed by the NSV, was especially affected by the flood. Prior to the storm, the reservoir was almost full, which made it nearly impossible for the reservoir to absorb storm water volumes and reduce river discharges flowing downstream into Longmont (J. Freel, personal communication). By the morning of September 11th, water discharge flowing over the spillway (approximated to be up to 11,000 cfs) had completely removed the dirt road to Ralph Price, making travel out of the area via car or foot impossible (J. Freel, personal communication). As a result, 13 civilians and one ranger, ranging in age from 1 to 81 years old, were evacuated from the area via helicopter on September 15th (J. Freel, personal communication). The damages to roadways and infrastructure were so widespread, that residents could not return full-time until the following May.

# Appendix B

# Fieldwork Timeline

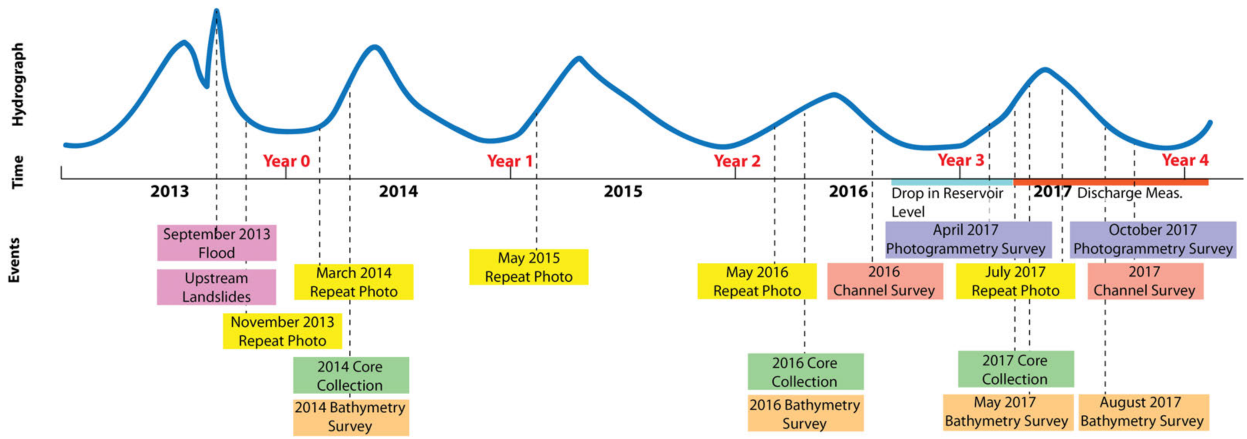


**Figure B.1:** A timeline of the fieldwork conducted at Ralph Price Reservoir in relation to the September 2013 flood, annual snowmelt runoff, and planned drop in base level

.

# Appendix C

# Details of Methodology Procedures

## C.1 RTK Survey Correction

Following the field effort, the base station location files (.tps) for each field survey were uploaded. For each base station location, the calculated vertical height and base station location files (see Table C.1) were uploaded into the NOAA Online Positioning User Service (OPUS). OPUS output provides the National Spatial Reference System (NSRS) coordinate of each base station. As part of the upload, the TPSGR5 antenna was selected.

The surveyed points were then corrected by the difference between the original RTK base station location and the corrected NSRS coordinate. The horizontal root mean square (HRMS) error ranged from 0.3 cm to 1.7 cm, and the vertical root mean square (VRMS) error ranged from 0.5 cm to 2.3 cm across all surveys.

## C.2 Bathymetric Survey Procedure

The 200kHz transducer has the ability to measure bathymetry up to an angle of 11° from vertical. The swath of area covered by the survey is therefore a function of the reservoir depth at a certain point (Figure C.1b), and varies by location. To get a better sense of aerial coverage, this horizontal distance was calculated and graphed in Matlab (see Appendix E.1 for Matlab script used).

Depth values along the survey track were calculated by measuring the distance between the water surface and the submerged sonar. This distance was added to each depth measurement to calculate the total depth (Figure C.1b). To calculate the reservoir bottom elevation, the total depth was subtracted from the reservoir elevation (shown in Table C.2).

**Table C.1:** RTK-GPS base station information for topographic surveys of the approach channel of North St. Vrain Creek at Ralph Price Reservoir for each survey date. Static uploads denote base stations that remained in the same location for at least 2 hours, whereas rapid uploads represent locations based on data collected for less than 2 hours.

| Date | Control Point | Vertical Height (m) | Log Name | Type of Upload |
|---|---|---|---|---|
| 03Aug2016 | Base1 | 1.909 | log0803p | static |
| 03Aug2016 | Base2 | 1.964 | log0803t000 | rapid |
| 01Sep2016 | BaseX | 1.909 | log0901o | static |
| 01Sep2016 | BaseY | 1.899 | log0901t | rapid |
| 22Apr2017 | Base1 | 1.961 | log0422r | static |
| 23Apr2017 | Base1 | 1.929 | log0423p | static |
| 06Jul2017 | Base1 | 1.979 | log0706q | rapid |
| 07Jul2017 | Base1 | 1.949 | log0707p | static |
| 08Jul2017 | Base1 | 1.919 | log0708p | rapid |
| 10Jul2017 | Base1 | 1.924 | log0710p | static |
| 16Sep2017 | 1654_LS2 (10:36) | 1.949 | log0916q | static |
| 16Sep2017 | 1654_LS2 (12:51) | 1.949 | log0916q | static |
| 16Sep2017 | 1654_LS2 (13:32) | 1.884 | log0917o | static |
| 17Sep2017 | 1654_LS2 | 1.989 | log0917o | static |
| 30Sep2017 | 1654_LS4 | 1.914 | log0930o | rapid |
| 01Oct2017 | 1654_LS3 | 1.907 | log1001p | static |
| 03Oct2017 | 1654_LS | 1.923 | log1003q | static |

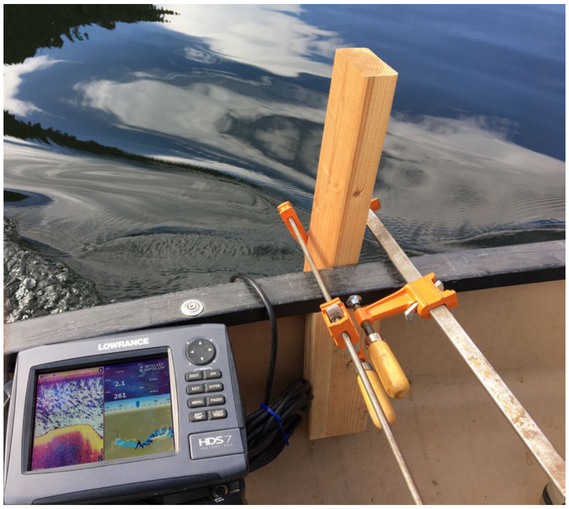

**(a)** A field photograph of the sonar setup mounted on a canoe during bathymetry surveying.

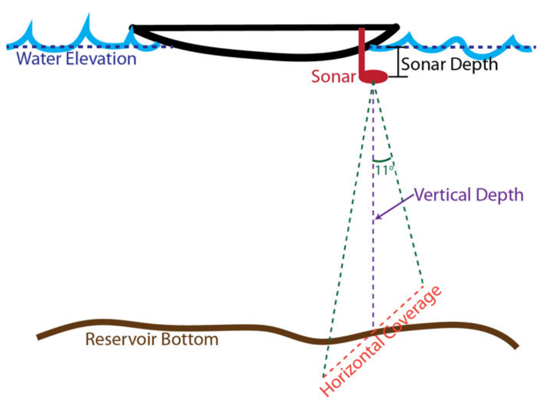


**(b)** An illustration of the measurements collected and used for each bathymetry survey to calculate the elevation of the reservoir bottom.

**Figure C.1:** A figure and illustration of the sonar setup used to complete bathymetric surveys.

Table C.2: Measured reservoir elevations used for bathymetry survey analysis.

| Date of Survey | Reservoir Elevation (m) |
|---|---|
| April 2014 | 1947.2 |
| April 2016 | 1948.8 |
| May 2017 | 1944.9 |
| August 2017 | 1950.8 |

## C.3 Core Collection

On April 11, 2014, one core was collected from a depth of 20 m below water surface and sediment surface elevation of 1928.89 m. On April 23, 2016, an additional core was collected 18 m to the northwest of the April 2014 core at an elevation of 1934.83 m.

To assess the rate of sediment remobilization in the inlet at the prodelta since the flood, eight cores were collected on April 21, 2017 and April 22, 2017. These cores provided one 'snapshot' of the sediment distribution, remobilization, and deposition in time. Six cores were collected near the former thalweg of the NSV and the deepest location of the analyzed reservoir area. To better understand the cross-sectional geometry of sediment accumulation in the inlet, two cores (Cores 5A and 5C) were retrieved from across the inlet.

The upper layer of many cores contained mud with a high water content. The viscous nature of these samples prevented them from being easily extruded and transferred into the split spoon sampler. As a result, these layers were subsampled at 1-cm increments and transferred into whirl packs. Information pertaining to core measurements, depth of retrieval, and length of subsampling is specified in Table 2.1. The relative location of each core is illustrated in Figure 2.3 and recorded in Table C.3.

**Table C.3:** Reservoir core sample location information.

| Core Name | Date Collected | Surface Elevation (m) | Easting (m) | Northing (m) |
|---|---|---|---|---|
| Core 2014 | 11Apr2014 | 1928.89 | 467034 | 4452086 |
| Core 2016 | 23Apr2016 | 1934.83 | 467019 | 4452096 |
| Core 2 | 22Apr2018 | 1929.76 | 467019 | 4452104 |
| Core 3 | 22Apr2018 | 1932.32 | 466993 | 4452113 |
| Core 4 | 21Apr2018 | 1934.18 | 466985 | 4452137 |
| Core 5A | 22Apr2018 | 1927.31 | 467017 | 4452165 |
| Core 5B | 21Apr2018 | 1933.67 | 466982 | 4452185 |
| Core 5C | 22Apr2018 | 1930.81 | 466997 | 4452196 |
| Core 6 | 21Apr2018 | 1929.68 | 467003 | 4452235 |
| Core 7 | 21Apr2018 | 1924.07 | 467071 | 4452321 |
| Core C | 17May2018 | 1944.71 | 467176 | 4451958 |
| Core D | 17May2018 | 1942.52 | 467057 | 4452044 |

## C.4 Pebble Count Locations


**Figure C.2:** The location of the pebble count surveys conducted in 2014 and 2017 (red), as well as additional channel surveyed in 2017.

## C.5 Core Analysis

Following the preparation procedure, a microscope slide was used to clean the surface of each core and make the stratigraphy more visible. High-resolution imagery of the cores were additionally captured using a Nikon D7200 camera paired with a 105mm f/2.8 telephoto Micro lens, and stitched together in Adobe Photoshop.

**Table C.4:** The subsampling depths of each core for LOI, XRF, and grain size analysis.

| Core Name | Subsampling Depths (cm) |
|---|---|
| Core 2 | 6-7, 13-14, 16-17, 17-18, 18-19, 28-29, 33-34, 39-40, 47-48, 58-59 |
| Core 3 | 2-3, 8-9, 15-16, 21-22, 26-27, 27-28, 32-33, 37-38, 40-41, 42-43, 45-46 |
| Core 4 | 0-57 at 1-cm intervals |
| Core 5A | 0-1, 7-8, 10-11, 13-14, 16-17, 23-24, 28-29, 39-40, 56-57, 64-65 |
| Core 5B | 9-10, 14-15, 18-19, 25-26, 28-29, 31-32, 38-39 |
| Core 5C | 0-2, 3-4, 6-7, 8-9, 12-13, 16-17, 20-21 |
| Core 6 | 9-10, 12-13, 15-16, 17-18, 19-20, 22-23, 24-25, 27-28 |
| Core 7 | 5-6, 14-15, 20-21, 25-26, 30-31, 33-34, 38-39, 47-48 |

### C.5.1 Loss on Ignition Procedure

Each sample consisted of a 1 $cm^3$ aliquot of the core sediment, whose wet mass was measured on an analytical balance with a 0.1 mg error (Step 1). As a next step, the sample was transferred to a pre-weighed crucible and dried in an oven for twenty-four hours at 90°C to remove the water content of the sample (Step 2). Once the mass of the dried soil samples was measured, the crucibles were placed into the oven for two hours at 550°C to burn off the organics in the sample (Step 3), and then re-weighed. Lastly, the samples were placed into the oven for two hours at 900°C to burn off the carbonates (Step 4), and then re-weighed.

The difference in mass throughout this process provides information about the concentration of water, carbon, and carbonates in each sample. Specifically, the difference between the mass obtained in Step 1 and Step 2 provide for the sample's water content, whereas the difference in mass between Step 2 and Step 3 provide for the sample's percent organics (e.g. carbon content).

Lastly, the difference between the sample mass in Step 3 and Step 4 determines the percent of carbonates in the sample.

### C.5.2 X-ray Fluorescence (XRF) Procedure

Geochemistry of the sample was conducted by placing the sample container into the sampling stand, and using an Olympus Delta scanner to shoot x-rays at the sample. Each sample was run three times, and the average of these measurements was recorded. The concentration of the following elements were measured for each sample: Ag*, Al, As*, Ca, Cd*, Cl*, Co*, Cr*, Cu*, Fe, K, Mn, Mo, Nb, Ni*, P*, Rb, S*, Sb*, Se*, Si, Sn*, Sr, Ti, V*, Y, Zn, Zr (note: the elements marked in an asterisk denotes insufficient detectable concentrations for useful analysis). Results were exported and uploaded into Matlab for comparison and analysis (see Appendix E.4 for the Matlab code used).

### C.5.3 Grain Size Analysis Procedure

#### Pretreatment Process

To begin the pretreatment process, a 0.25-0.5 $cm^3$ sample was extracted from the core, placed into a pre-weighed 125mL syringe, and weighed on an analytical balance. For the first treatment, approximately 20 mL concentrated hydrogen peroxide (30%) was poured into each syringe. Samples were soaked in hydrogen peroxide and shaken for 24 hours. As a next step, each sample was transferred into a 150 mL beaker using a metal spatula, and placed under a hood on a hotplate at medium heat. Once the contents in each beaker were reduced to a volume of approximately 5 mL, samples were monitored for remaining organic materials (i.e. needles, worms, etc.). Visible organics were removed with forceps and discarded. Next, approximately 60 mL of distilled water was added to the beaker, and the beaker was again placed on a hotplate on medium heat. Samples were removed from the hotplate once the contents in each beaker were reduced to a volume of approximately 5 mL.

If organic particles had been visible at the end of the first treatment, the treatment process was repeated. If not, samples were returned into a syringe, and 0.10 g of Sodium Hexametaphosphate (a deflocculant) was added to the samples. As a last step, samples were shaken for an additional 24 hours.

**Sieving Analysis**

As a next step, the proportion of sample greater than 500 um and 125 um in diameter was measured through a dry sieving procedure. Three, 3 in diameter USA standard nested test sieves were used to sort coarse sand (No.35, 500 um), medium sand (No. 60, 250 um), and fine sand (No.120, 125 um). Each sample was transferred into the sieves with water, and shaken for 90 minutes using a Cole-Parmer one-touch vibratory Sieve Shaker at Level 3. Sediment remaining in each sieve was transferred into a pre-weighed tin, and then dried in an oven for 24 hours. Once dried, the mass of each sample was measured. Sediment that passed the 125 um sieve was returned to a 125 mL syringe for laser particle size analysis. Between each sieving procedure, sieve screens were cleaned using an Elma S50R Elmasonic sieve cleaner, and dried in the oven.

**Laser Particle Size Analysis**

The difference between each sample's initial dry mass and the sum of the sieved sample mass were used to determine the percentage of the sample with a grain size less than 125 um. This remaining sediment was shaken for at least one hour before conducting laser particle size analysis. Next, each 150 mL test tube was filled to the top with deionized water. 100 uL of suspended material was added to 140 mL of deionized water in a glass sample vial, and mixed with a glass stir rod. This sample vial was placed into a Spectrex PC-2200 Laser Particle Counter and the proportion of very fine sand, silt, and clay grain sizes were measured. Numerous samples were rerun, and produced comparable results. However it was concluded that the sediments had a high clay content that overwhelmed the accuracy of the particle counter results. With this in mind, clay and silt results are reported and similar to qualitative observations of the relative proportion of each, but these analyses should be considered to be limited in accuracy. Results of a sample's total grain size analysis was graphed as part of core comparison analysis (refer to script used blow).

**Grain Size Analysis of Cores C and D**

A more crude grain size analysis was conducted on Cores C and D to form a general idea of size distributions. An approximately 100-gram aliquot of each sample was collected at 15-cm intervals and placed into a pre-weighed tin dish. Samples were dried in an overnight, and then reweighed.

Each sample was sieved using a series of six, 3 in diameter USA standard nested test sieves to sort very fine pebbles (No.10, 2 mm), very coarse sand (No. 18, 1 mm), coarse sand (No.35, 500 um), medium sand (No. 60, 250 um), and fine sand (No.120, 125 um). Samples were shaken for 60 minutes using a Cole-Parmer one-touch vibratory Sieve Shaker at Level 3. The sediment remaining in each sieve was transferred into a pre-weighed tin, dried in an oven for 24 hours, and weighed again. The proportion of each grain size was calculated by comparing the mass of each grain size to the original total mass of the sample. Between each sieving procedure, sieve screens were cleaned using an Elma S50R Elmasonic sieve cleaner, and dried in the oven.

## C.6 Methods for Volumetric Analysis at the Delta

**Method 1: SGeMs and Geomorphic Change Detection Package**

As a freely available software, SGeMs is able to conduct kriging of up to approximately 2000-3000 data points. More data values, however, will cause the program to crash. Since many of the points collected through the bathymetry surveys were recorded at very frequent time intervals, many of these points overlapped with one another and were not necessary for the data analysis. As a result, the data was randomly resampled to include a maximum of 2000 points.

Once resampled, the data was transformed to a .dat file that was readable for the SGeMs software, and then loaded into SGeMs as a point set. This point set was used to construct a variogram for each survey (Appendix D.1), used to determine the kriging parameters (Table C.5). These determined parameters were then used to perform ordinary kriging. Because the data are not anisotropic, a circular search ellipse was used to krig the data.

**Table C.5:** Table of the kriging parameters used for ordinary kriging of bathymetry survey data in SGeMs based on variogram analysis.

| Date of Survey | Downsample Size | Range (m) | Sill (m) | Nugget (m) | Conditioning Data |
|---|---|---|---|---|---|
| April 2014 | 2,000 | 12.5 | 5 | 0 | 0-25 |
| April 2016 | 2,000 | 37.0 | 7.5 | 0 | 0-30 |
| May 2017 | 1,400 | 92.0 | 30 | 0 | 0-30 |
| August 2017 | 2,000 | 15.0 | 35 | 0 | 0-25 |

Once a kriged model was produced, the data was output as a .csv file, and re-organized using a Matlab script (Appendix E.2).These kriged data points were then loaded and converted to a raster output in ArcGIS using the 'point-to-raster' module. Shapefile polygons were further created to outline the area covered by each survey and delineate the outline of the area of repeat bathymetry. Each kriged raster was then clipped by this area. These resulting rasters were used to difference vertical changes in sediment topography and define the progradation of the delta front with time.

Once each raster was clipped by the area of repeat bathymetry, change detection analysis was performed. Each Digital Elevation Model (DEM) was added to the Geomorphic Change Detection (GCD) project using the 'add to the GCD project' icon. In this module, each raster is corrected so that it contains the same cell resolution for alignment. Once imported and corrected, the 'add change detection' icon is selected. As part of this analysis, a 'New Survey' (e.g. more recent raster) was compared to a selected 'Old Survey' (e.g. older raster). A simple minimum level of threshold detection of 10 cm was applied.

### Method 2: Earth Volumetric Studio

For this method, each survey track was input into a geology (.geo) file that included the elevation of the reservoir level (set at an elevation of 1,948 m for consistency), as well as the bathymetry elevation along each point of the survey. Refer to Table C.6 for detailed instructions on how to set up this file type.

**Table C.6:** A template of the .geo file format used for each survey, and and example of the first few rows of data entered into the file.

| Template | | | | |
|---|---|---|---|---|
| $G | 1st Data Column (Easting) | 2nd Data Column (Northing) | | |
| Type of Values | 3rd Data Column | 4th Data Column | Unit of Measure | |
| No. of Points | No. Surfaces | 0 - Top Surface Index | 1 - Bathymetry Index | 2 - Bottom Surface Index |
| Pt 1 Easting | Pt 1 Northing | Water Surface Elevation | Bathymetry at Pt 1 | Bottom Surface Value |
| Pt 2 Easting | Pt 2 Northing | Water Surface Elevation | Bathymetry at Pt 2 | Bottom Surface Value |
| Pt 3 Easting | Pt 3 Northing | Water Surface Elevation | Bathymetry at Pt 3 | Bottom Surface Value |
| Pt 4 Easting | Pt 4 Northing | Water Surface Elevation | Bathymetry at Pt 4 | Bottom Surface Value |
| Pt 5 Easting | Pt 5 Northing | Water Surface Elevation | Bathymetry at Pt 5 | Bottom Surface Value |
| Pt 6 Easting | Pt 6 Northing | Water Surface Elevation | Bathymetry at Pt 6 | Bottom Surface Value |
| **Example** | | | | |
| $G | X | Y | | |
| Elevation | WaterSurfElev | Bathymetry | Meters | |
| 6 | 3 | 0 | 1 | 2 |
| 467168 | 4451900 | 1948 | 1942.214 | 1900 |
| 467168 | 4451898 | 1948 | 1942.259 | 1900 |
| 467170 | 4451895 | 1948 | 1942.593 | 1900 |
| 467170 | 4451896 | 1948 | 1942.367 | 1900 |
| 467168 | 4451897 | 1948 | 1942.063 | 1900 |
| 467167 | 4451900 | 1948 | 1942.032 | 1900 |

Once this 'krig_3d' module was run (see Table C.7 below for kriging parameters used), a three-dimensional volume was created for each bathymetry survey, representing the volume of water between the water surface and the reservoir bottom. To compare and overlay bathymetry data from different survey years across the same aerial extent, the volume produced through kriging was then vertically cut by the shapefile of the area of repeat bathymetry (using the 'area_cut' module).

To calculate the sediment volume, the reservoir bottom of each survey was also run through a 'geologic surfaces' module. This module outputs the reservoir surface from one model, and uses this surface to slice through the sediment volume of another model. The calculated volumetric difference represents the net accumulated sediment volume. The 'volumetrics' module calculates this volume and provides it in user-specified units. The workflow and interaction between modules used to calculate the volume of sediment accumulation in the inlet between April 2014, April 2016, and August 2017 is shown in Figure C.3.

**Table C.7:** Table of the kriging parameters used for ordinary kriging of bathymetry survey data in EVS.

| Date of Survey | Range (m) | Sill (m) | Nugget (m) | Reach (m) | Points in Reach |
|---|---|---|---|---|---|
| April 2014 | 20.0 | 3.30 | 0 | 422 | 20 |
| April 2016 | 40.0 | 6.00 | 0 | 1,637 | 20 |
| May 2017 | – | – | – | – | – |
| August 2017 | 75.0 | 48.0 | 0 | 1,139 | 20 |

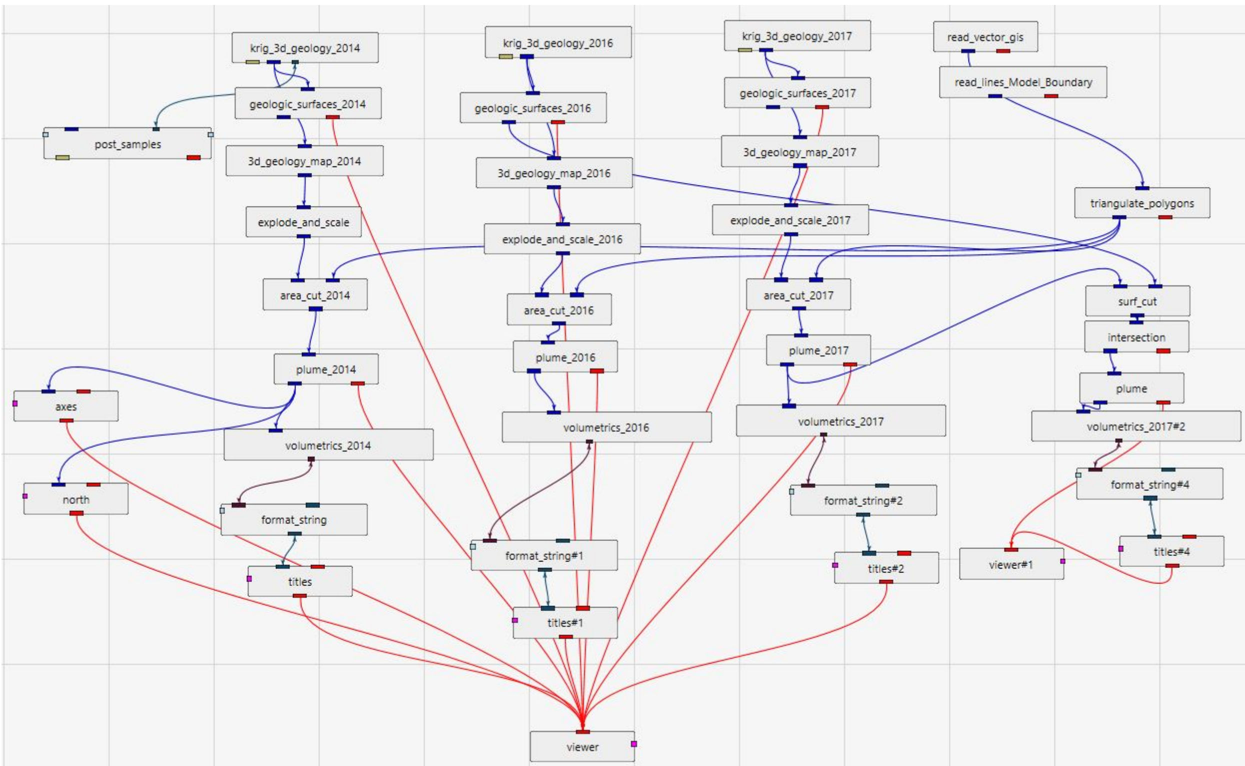


**Figure C.3:** The input modules in the EVS viewer used to calculate volumetric change based on bathymetry survey data.

## C.7 Photogrammetry Analysis Procedure

Photos were imported into Agisoft Photoscan Professional, and the image quality was verified to be above a 'quality' value of 0.8 (based on a scale of 0 to 1, with 1 representing best quality). Photos were then aligned using a medium accuracy detection setting, a key point limit of 60,000, and a tie point limit of 0. No adaptive camera model fitting was applied. The resulting sparse point cloud was then used to filter out points and decrease error alignment.

The ‘gradual selection’ module was used to reduce adjustment errors. First, points with a reconstruction uncertainty value above 10 were deleted to discard points with poor matches in geometry. Following this step, the camera alignment was re-optimized. Next, the ‘projection accuracy’ was decreased to less than 3 to remove points with high pixel matching error. The remaining points were then re-optimized. Lastly, points with high pixel residual errors were used by deleting points a ‘reprojection error’ above 0.3 pixels. Once points with associated error were deleted from the sparse point cloud, a dense point cloud was built using the ’high’ quality and aggressive depth filtering. Next, a 1.8-cm resolution DEM projected to UTM 13N was created from the dense point cloud and exported to an .xyz file.

In Matlab, the .xyz file was read using the ‘xyzread’ script. A shapefile was created in ArcGIS, and its vertices was pulled into Matlab using the ‘shaperead’ command. The ‘in polygon’ command created a binary vector that indicated whether certain points in the .xyz file were within or outside of the polygon (1=within, 0=outside). Using this binary vector, the data points in the .xyz file were then filtered based on being within and outside of the polygon. The points within the polygon were read into a new, reduced .xyz file point cloud. Matlab scripts for this procedure can be found in Appendix E.3.

These dense point clouds (in the form of .xyz) were then brought into Cloud Compare, which used 45 matching points to better align the dense point clouds. The April 2017 DEM was shifted and tilted to best match the October 2017 point cloud, and then exported. The transformation matrix used is detailed below.

## C.8 Channel Morphology Differencing Procedure

The RTK points were first corrected (as outlined in Section 2.1.1), and more closely aligned in EVS. 870 survey points were collected in 2016, and 1,667 survey points were recorded in 2017. Thirty survey points collected in 2016 and denoted as ’bedrock outcrops’ were also included in the 2017 survey, as it was assumed that no significant bedrock incision had occurred between 2016 and 2017.

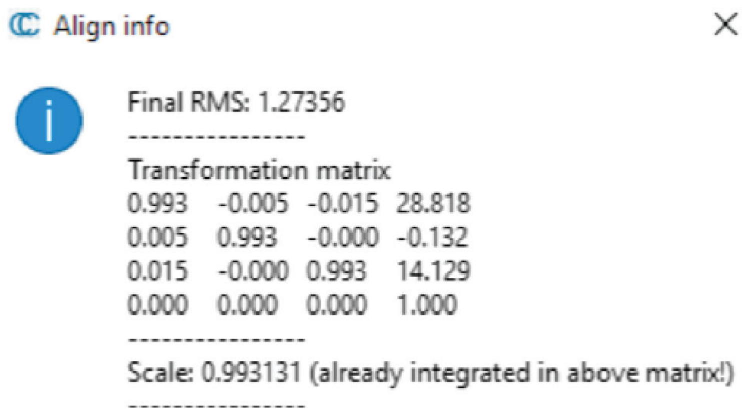


**Figure C.4:** The transformation matrix used to align the April 2017 DEM produced in Agisoft SfM.

The channel geometry was interpolated through ordinary kriging in SGeMs. Unlike the bathymetry surveys, points did not need to be downsampled in this case. The kriging parameters used to krig the data are presented in Table C.8.

**Table C.8:** Table of the kriging parameters used for ordinary kriging of channel RTK survey data in SGeMs.

| Survey Year | Range (m) | Sill (m) | Nugget (m) | Conditioning Data |
|---|---|---|---|---|
| Summer 2016 | 12.6 | 1.0 | 0 | 0-15 |
| Summer 2017 | 15.0 | 1.0 | 0 | 0-15 |

Each survey was kriged to a grid with cells 10cm-by-10cm in dimension. This data was read into Matlab, clipped by a rough polygon outline of the channel, and exported as an .xyz file (as outlined in Section C.6).

In ArcGIS the .xyz points were converted to a feature class using the ‘ASCII 3D to Feature Class’ tool. The output feature class type was set to ‘point’, and the coordinate system was set to NAD 1983 UTM Zone 13N. Once the points were created, the attribute table was modified to include a new column for each point’s corresponding elevation. This new column was then modified by right clicking and selecting the ‘Calculate Geometry’ feature to produce the ‘Z Coordinate of Point’, or elevation output. Next, the ‘Point to Raster (Conversion)’ tool was used to convert the points into a raster DEM. Elevation values were specified as an ‘input feature’ and a cell size of

0.10 meters was applied. Once created, the raster was run through the ‘clip’ module to clip the section by the appropriate polygon extent. The DEMs produced in ArcGIS were then overlayed as outlined in Section C.6 to produce approximate volumetric calculations of erosion and incision that has occurred in the channel between summer 2016 and summer 2017.

# Appendix D

# Detailed Results

## D.1 SGeMs Variogram Models

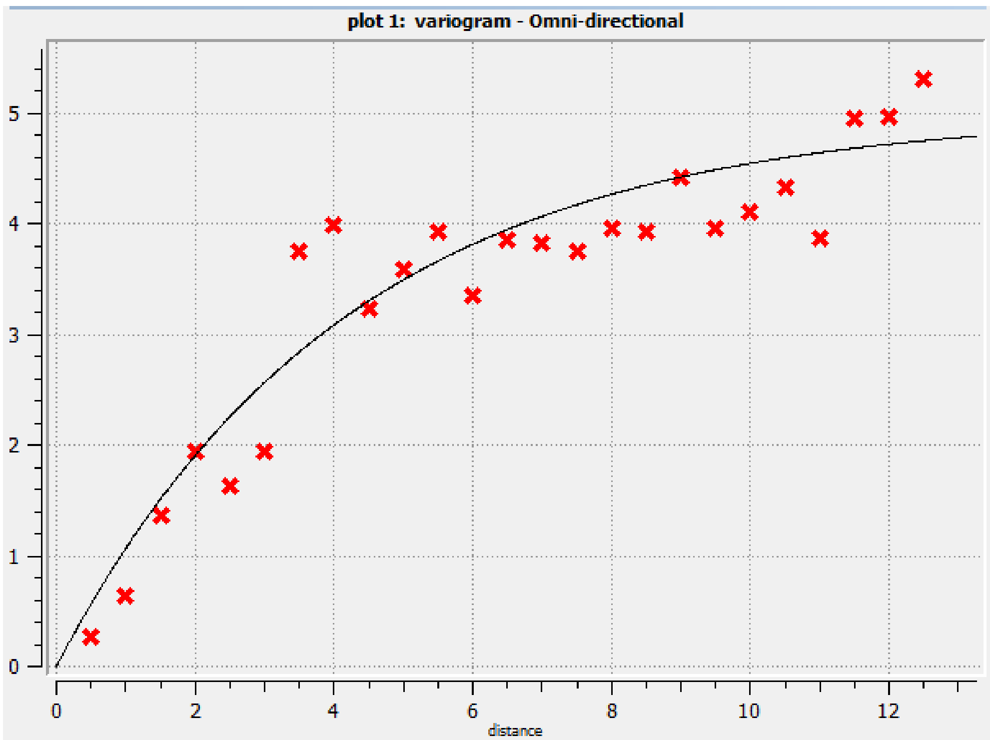


**Figure D.1:** April 2014 variogram

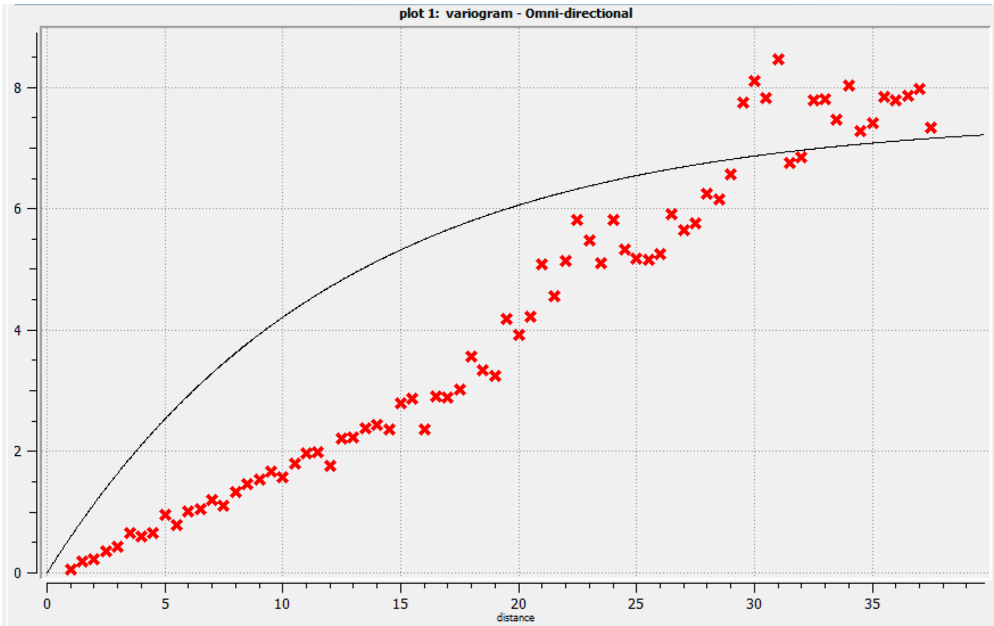


**Figure D.2:** April 2016 variogram

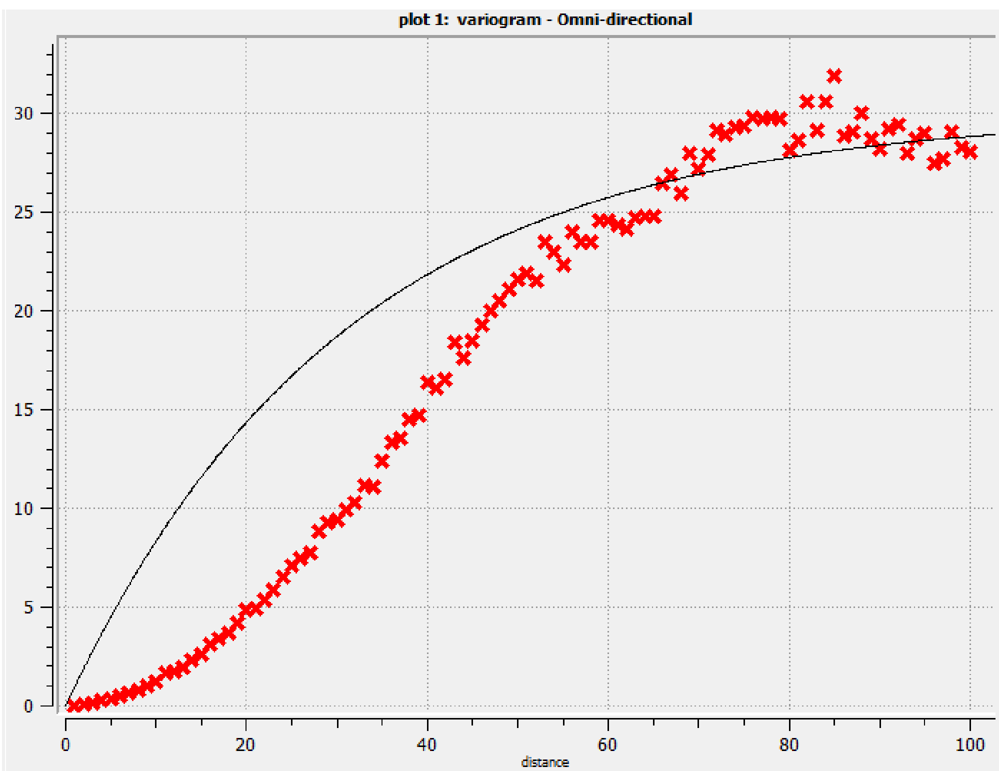


**Figure D.3:** May 2017 variogram

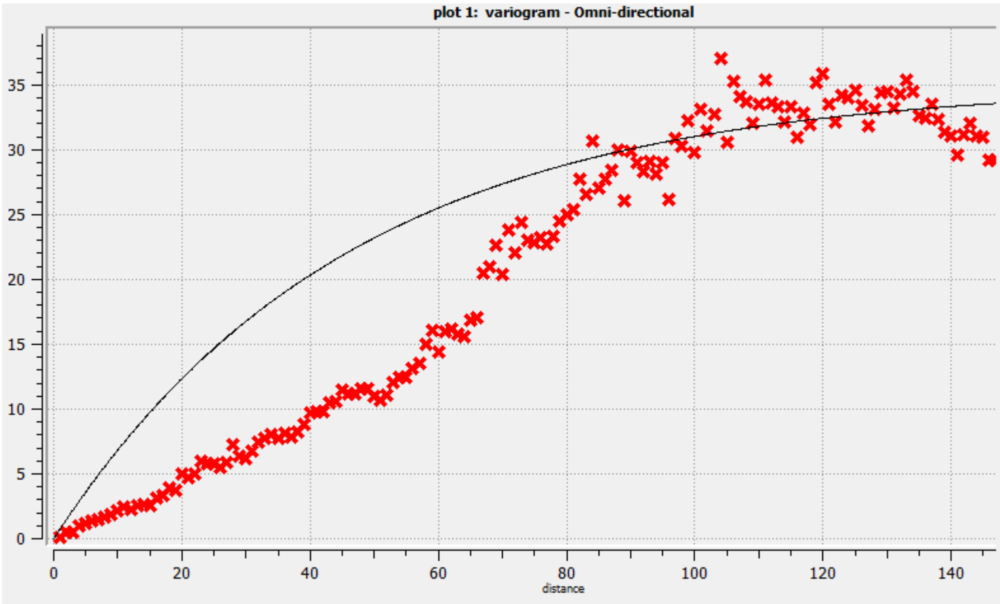


**Figure D.4:** August 2017 variogram

## D.2 Thalweg Location

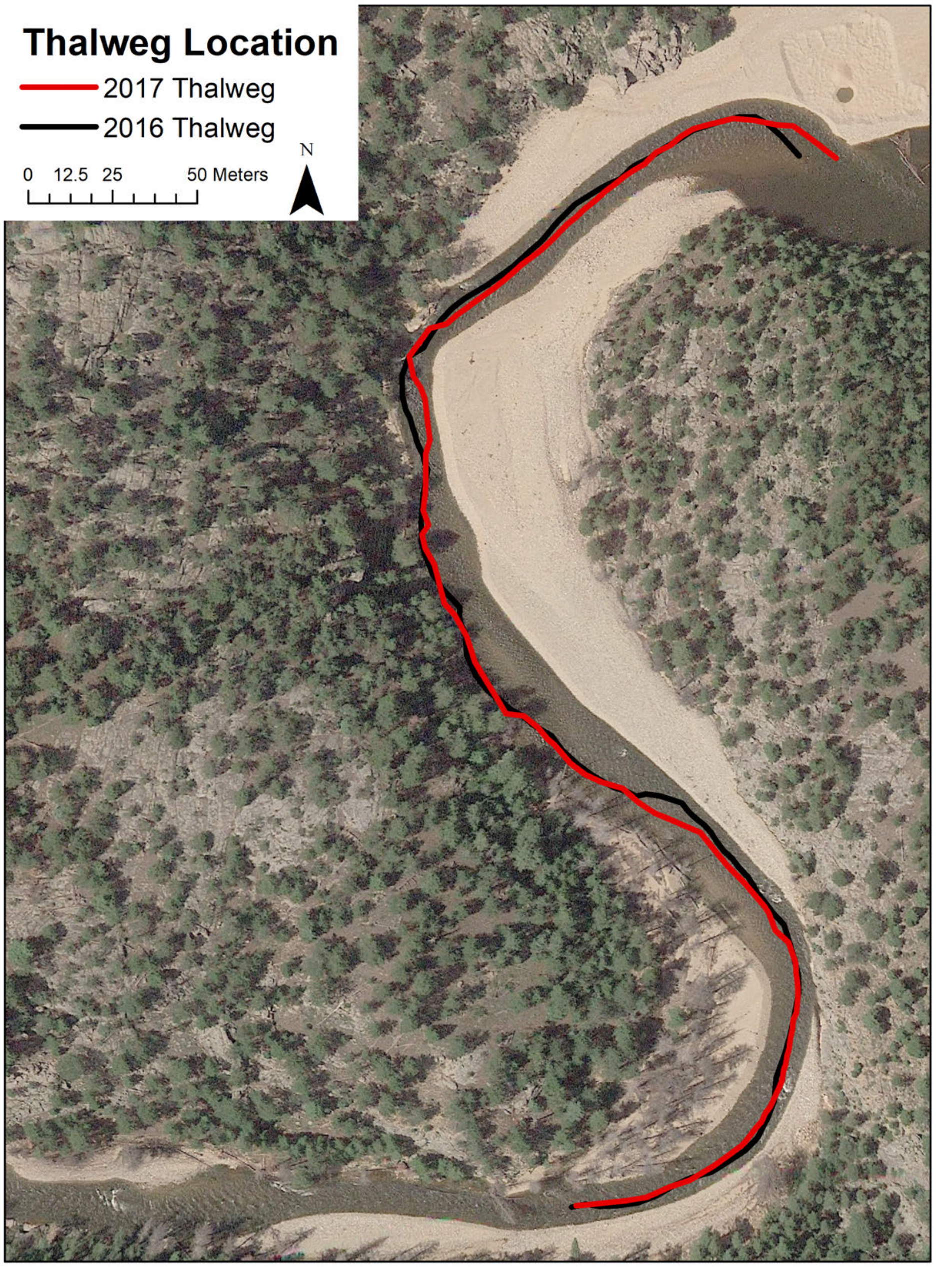


**Figure D.5:** The location of the 2016 and 2017 thalweg, obtained through RTK surveying. Comparison of the thalweg location indicates small lateral adjustment and changes in sinuosity.

## D.3 3-dimensional Channel Elevation Model

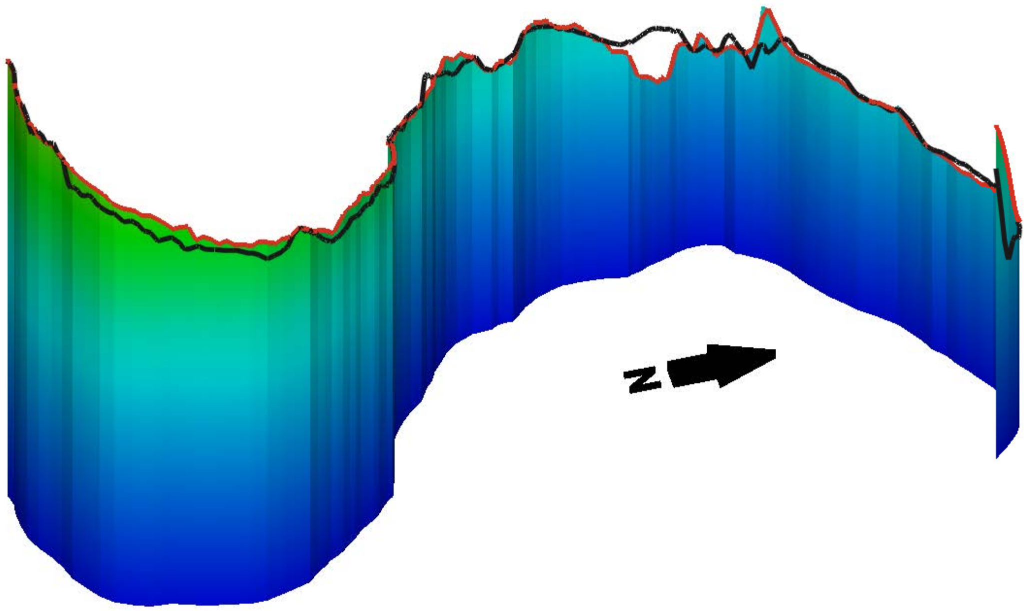


**Figure D.6:** Change in channel elevation between 2016 (black) and 2017 (red).

## D.4 April 2017 and October 2017 SfM Hillshade DEMs

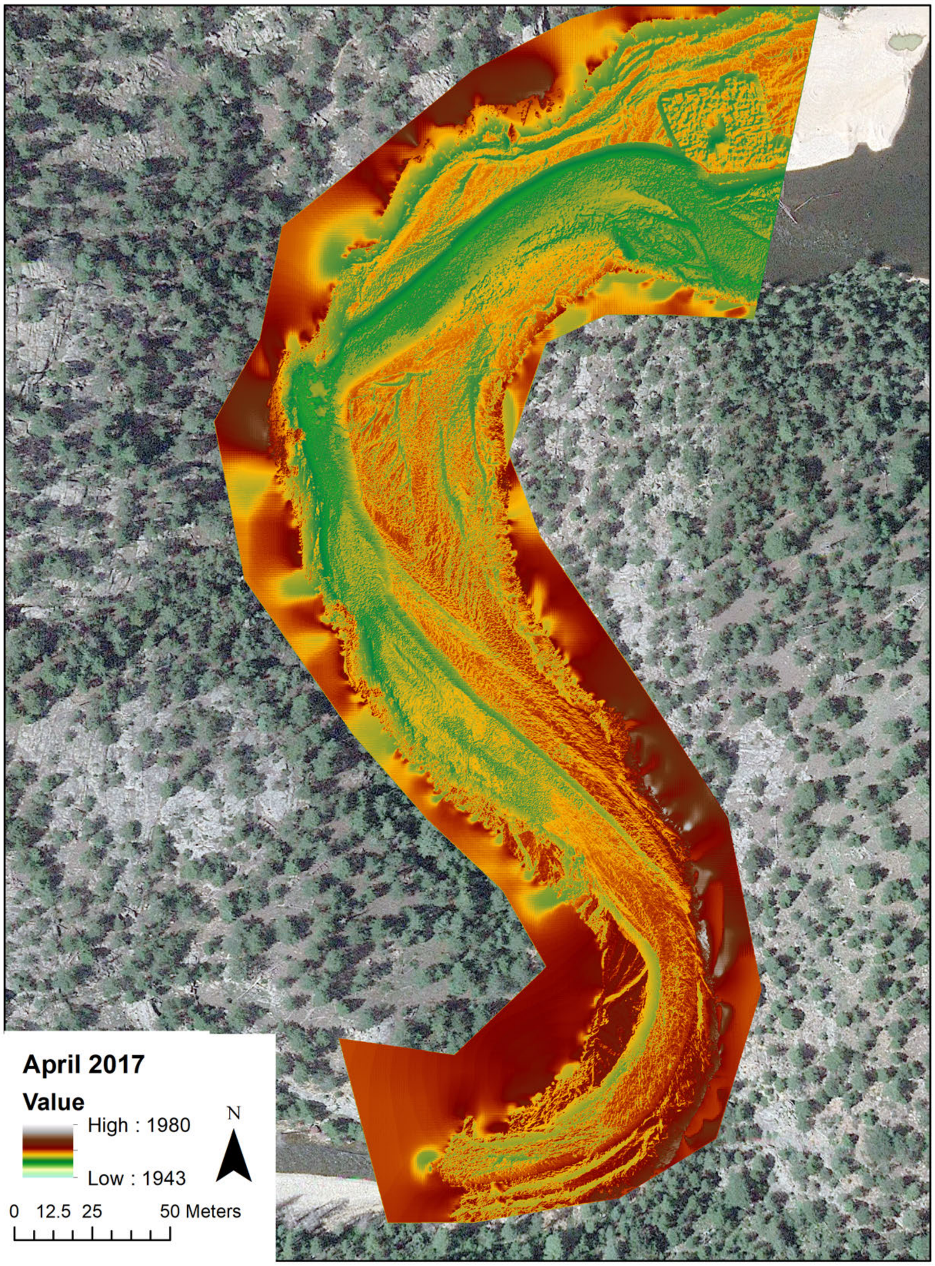


**Figure D.7:** April 2017 SfM hillshade DEM of the approach channel of North St. Vrain Creek upstream from Ralph Price Reservoir.

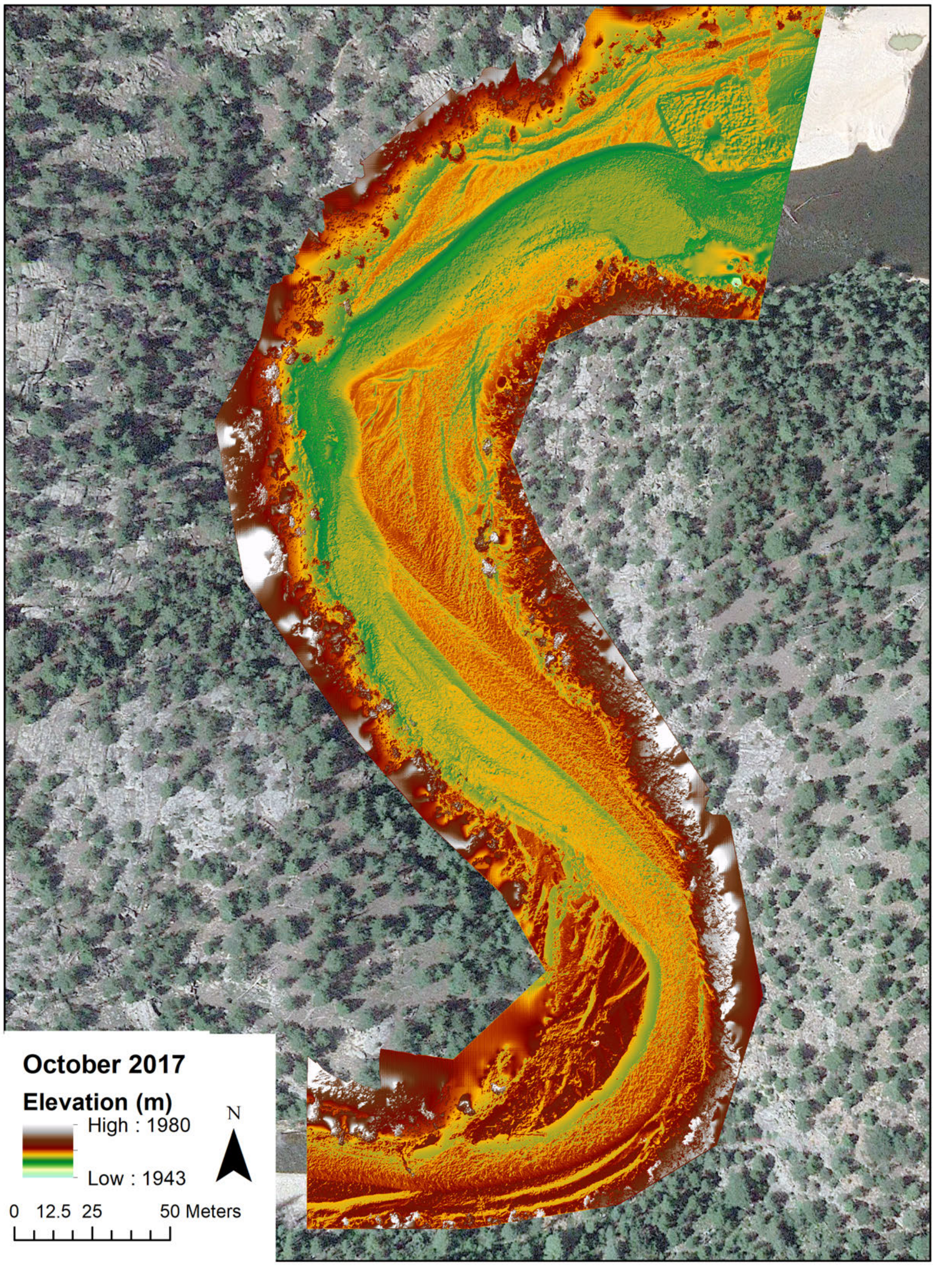


**Figure D.8:** October 2017 SfM hillshade DEM of the approach channel of North St. Vrain Creek upstream from Ralph Price Reservoir.

## D.5 Summer 2016 and Summer 2017 RTK Survey DEMs

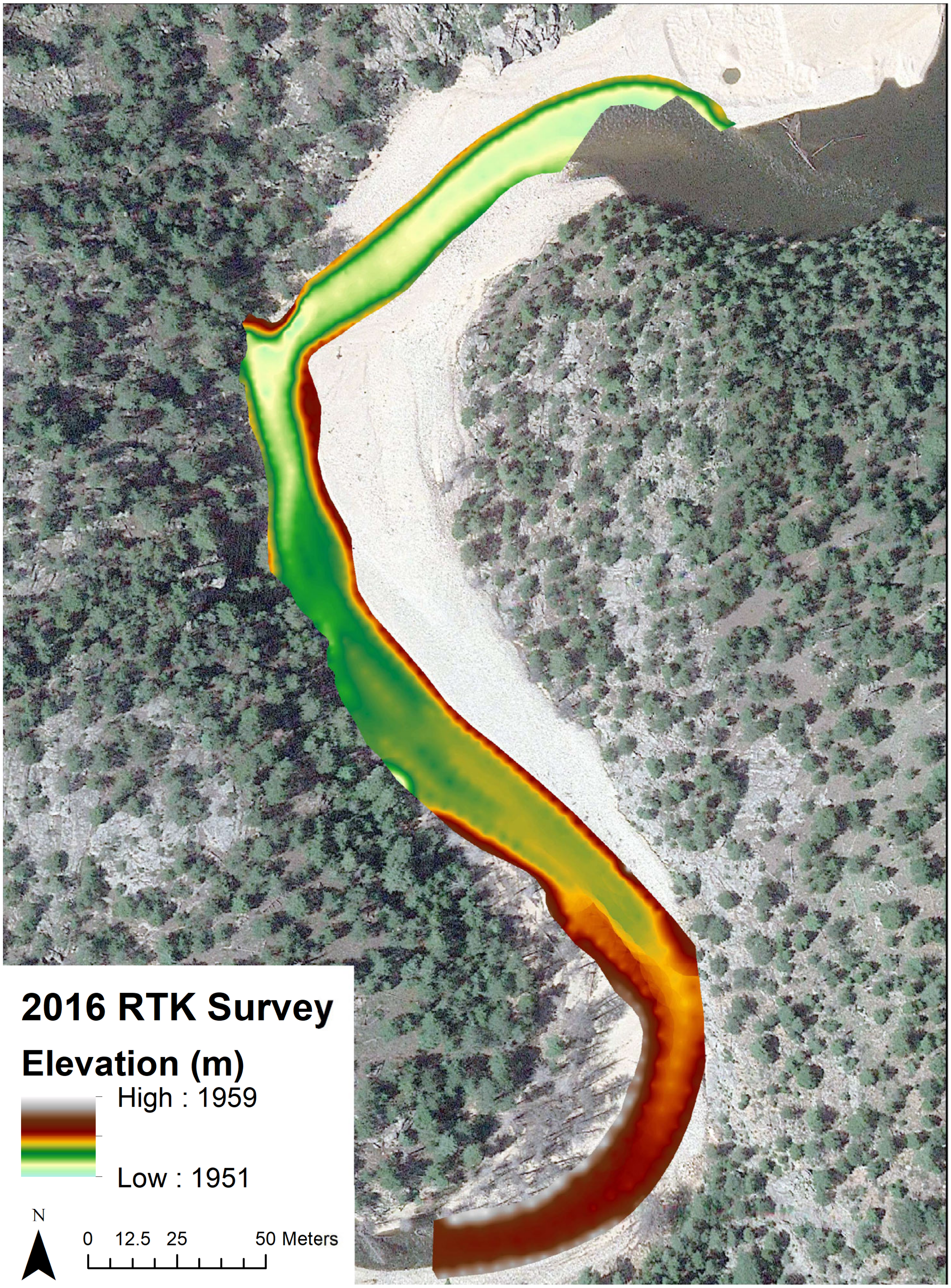


**Figure D.9:** Summer 2016 RTK survey

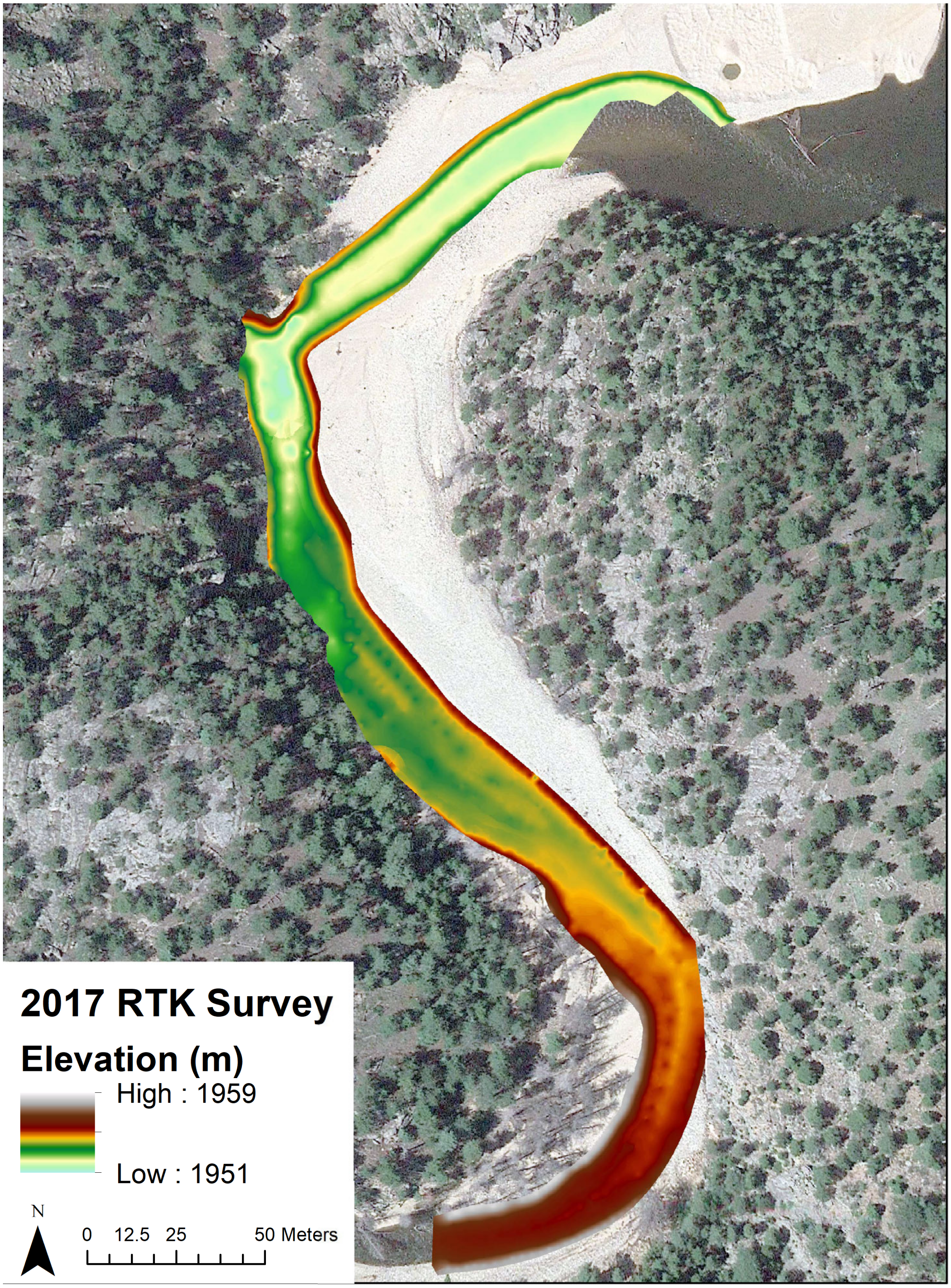


**Figure D.10:** Summer 2017 RTK survey

## D.6 Photogrammetry Analysis Differencing

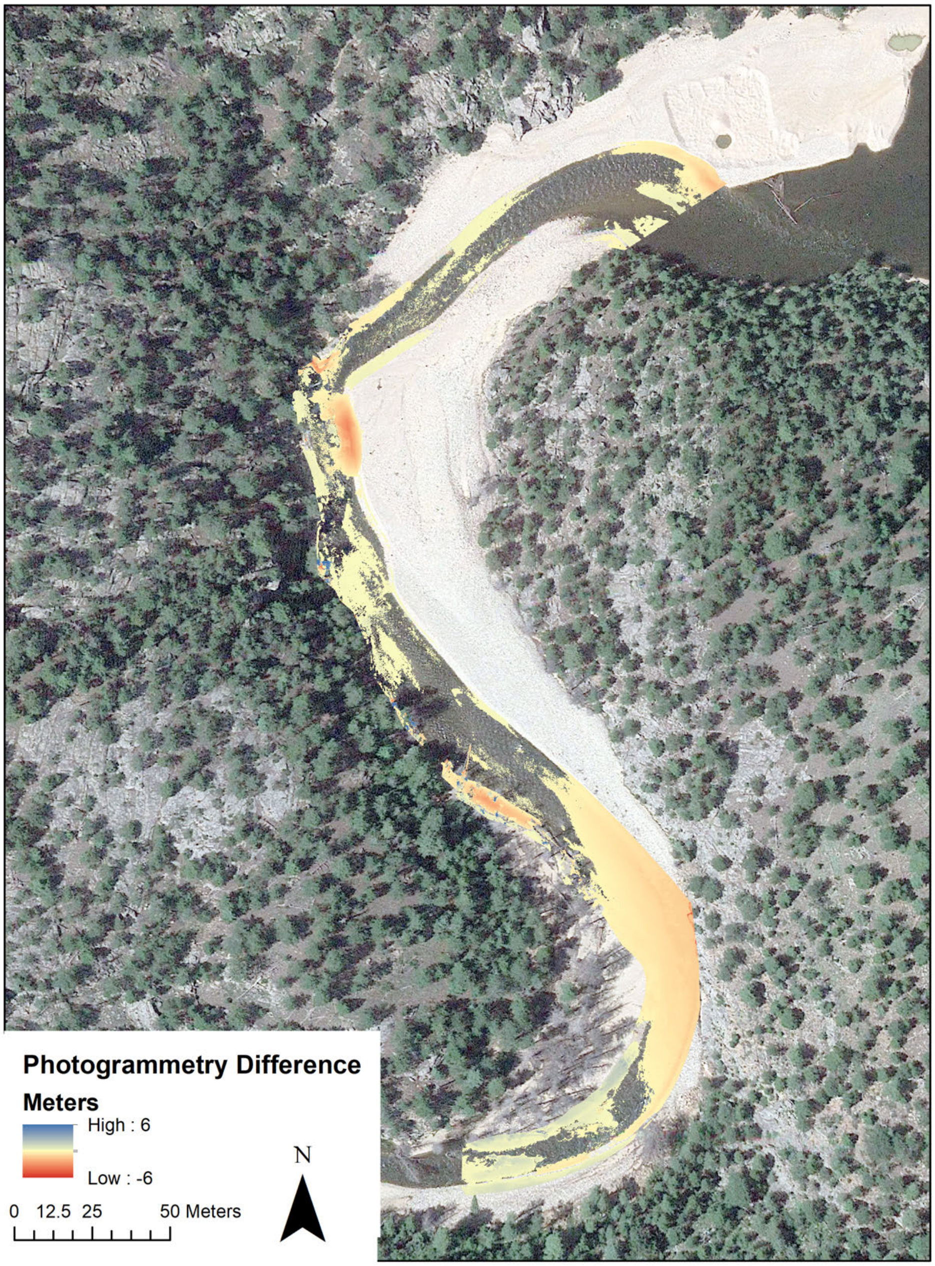


**Figure D.11:** Photogrammetry difference map produced when subaqueous channel points from the dense point cloud are included.

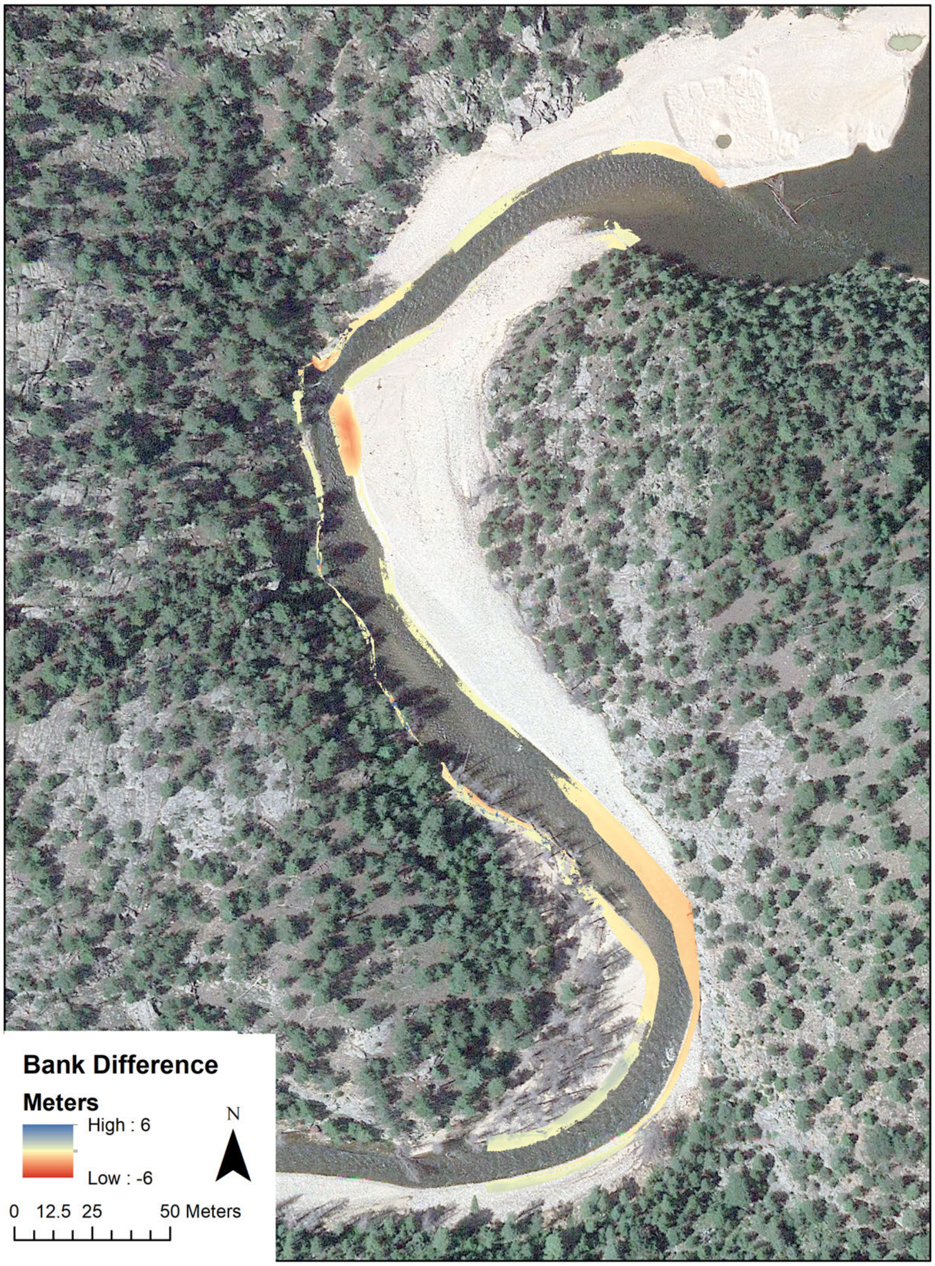


**Figure D.12:** Photogrammetry difference map produced when points from the banks are only included, and subaqueous channel points from the dense point cloud are removed.

## D.7 Channel Calculations Based on SfM DEMs

**Table D.1:** Volumetric differencing results of the left bank based on spring 2017 and fall 2017 photogrammetry-produced DEMs

Volumetric Difference: Left Bank

| Attribute | Raw | Thresholded | ± Error Volume | % Error |
|---|---|---|---|---|
| AREAL: | | | | |
| Total Area of Erosion ($m^2$) | 794.74 | 573.39 | | |
| Total Area of Deposition ($m^2$) | 827.46 | 575.73 | | |
| Total Area of Detectable Change ($m^2$) | NA | 1,149.12 | | |
| Total Area of Interest ($m^2$) | 1,622.20 | NA | | |
| Percent of Area of Interest with Detectable Change | NA | 70.84% | | |
| VOLUMETRIC: | | | | |
| Total Volume of Erosion ($m^3$) | 362.12 | 341.09 ± | 114.68 | 33.62 |
| Total Volume of Deposition ($m^3$) | 489.67 | 463.98 ± | 115.15 | 24.82 |
| Total Volume of Difference ($m^3$) | 851.79 | 805.08 ± | 229.82 | 28.55 |
| Total Net Volume Difference ($m^3$) | 127.56 | 122.89 ± | 162.51 | 132.24 |
| VERTICAL AVERAGES: | | | | |
| Average Depth of Erosion (m) | 0.46 | 0.59 ± | 0.2 | 33.62 |
| Average Depth of Deposition (m) | 0.59 | 0.81 ± | 0.2 | 24.82 |
| Average Total Thickness of Difference (m) for Area of Interest | 0.53 | 0.5 ± | 0.14 | 28.55 |
| Average Net Thickness of Difference (m) for Area of Interest | 0.08 | 0.08 ± | 0.1 | 132.24 |
| Average Total Thickness of Difference (m) for Area with Detectable Change | NA | 0.7 ± | 0.2 | 28.55 |
| Average Net Thickness of Difference (m) for Area with Detectable Change | NA | 0.11 ± | 0.14 | 132.24 |
| PERCENTAGES (BY VOLUME): | | | | |
| Percent Erosion | 42.51 | 42.37 | | |
| Percent Deposition | 57.49 | 57.63 | | |
| Percent Imbalance (departure from equilibium) | 7.49 | 7.63 | | |
| Net to Total Volume Ratio | 14.98 | 15.26 | | |

**Table D.2:** Volumetric differencing results of the right bank based on spring 2017 and fall 2017 photogrammetry-produced DEMs

Volumetric Difference: Right Bank

| Attribute | Raw | Thresholded | ± Error Volume | % Error |
|---|---|---|---|---|
| AREAL: | | | | |
| Total Area of Erosion ($m^2$) | 1,161.51 | 901.12 | | |
| Total Area of Deposition ($m^2$) | 865.13 | 430.96 | | |
| Total Area of Detectable Change ($m^2$) | NA | 1,332.08 | | |
| Total Area of Interest ($m^2$) | 2,026.64 | NA | | |
| Percent of Area of Interest with Detectable Change | NA | 65.73% | | |
| VOLUMETRIC: | | | | |
| Total Volume of Erosion ($m^3$) | 928.37 | 905.39 ± | 180.22 | 19.91 |
| Total Volume of Deposition ($m^3$) | 245 | 199.13 ± | 86.19 | 43.28 |
| Total Volume of Difference ($m^3$) | 1,173.37 | 1,104.52 ± | 266.42 | 24.12 |
| Total Net Volume Difference ($m^3$) | -683.38 | -706.26 ± | 199.77 | -28.29 |
| VERTICAL AVERAGES: | | | | |
| Average Depth of Erosion (m) | 0.8 | 1 ± | 0.2 | 19.91 |
| Average Depth of Deposition (m) | 0.28 | 0.46 ± | 0.2 | 43.28 |
| Average Total Thickness of Difference (m) for Area of Interest | 0.58 | 0.54 ± | 0.13 | 24.12 |
| Average Net Thickness of Difference (m) for Area of Interest | -0.34 | -0.35 ± | 0.1 | -28.29 |
| Average Total Thickness of Difference (m) for Area with Detectable Change | NA | 0.83 ± | 0.2 | 24.12 |
| Average Net Thickness of Difference (m) for Area with Detectable Change | NA | -0.53 ± | 0.15 | -28.29 |
| PERCENTAGES (BY VOLUME): | | | | |
| Percent Erosion | 79.12 | 81.97 | | |
| Percent Deposition | 20.88 | 18.03 | | |
| Percent Imbalance (departure from equilibium) | -29.12 | -31.97 | | |
| Net to Total Volume Ratio | -58.24 | -63.94 | | |

**Table D.3:** Volumetric differencing results of the channel bank (right and left) based on spring 2017 and fall 2017 photogrammetry-produced DEMs

Volumetric Difference: Right and Left Bank (combined)

| Attribute | Raw | Thresholded | | ± Error Volume | % Error |
|---|---|---|---|---|---|
| AREAL: | | | | | |
| Total Area of Erosion (m²) | 1,956.25 | 1,474.51 | | | |
| Total Area of Deposition (m²) | 1,692.59 | 1,006.69 | | | |
| Total Area of Detectable Change (m²) | NA | 2,481.20 | | | |
| Total Area of Interest (m²) | 3,648.84 | NA | | | |
| Percent of Area of Interest with Detectable Change | NA | 68.29% | | | |
| VOLUMETRIC: | | | | | |
| Total Volume of Erosion (m³) | 1,290.49 | 1,246.48 | ± | 294.90 | 23.66 |
| Total Volume of Deposition (m³) | 734.67 | 663.11 | ± | 201.34 | 30.36 |
| Total Volume of Difference (m³) | 2,025.16 | 1,909.60 | ± | 496.24 | 25.99 |
| Total Net Volume Difference (m³) | -555.82 | -583.37 | ± | 362.28 | -62.10 |
| VERTICAL AVERAGES: | | | | | |
| Average Depth of Erosion (m) | 1.26 | 1.59 | ± | 0.40 | 25.16 |
| Average Depth of Deposition (m) | 0.87 | 1.27 | ± | 0.40 | 31.50 |
| Average Total Thickness of Difference (m) for Area of Interest | 1.11 | 1.04 | ± | 0.27 | 25.96 |
| Average Net Thickness of Difference (m) for Area of Interest | -0.26 | -0.27 | ± | 0.20 | -74.07 |
| Average Total Thickness of Difference (m) for Area with Detectable Change | NA | 1.53 | ± | 0.40 | 26.14 |
| Average Net Thickness of Difference (m) for Area with Detectable Change | NA | -0.42 | ± | 0.29 | -69.05 |
| PERCENTAGES (BY VOLUME): | | | | | |
| Percent Erosion | 121.63 | 124.34 | | | |
| Percent Deposition | 78.37 | 75.66 | | | |
| Percent Imbalance (departure from equilibium) | -21.63 | -24.34 | | | |
| Net to Total Volume Ratio | -43.26 | -48.68 | | | |

**Table D.4:** Volumetric differencing results of the complete channel (including subaqueous points) based on spring 2017 and fall 2017 photogrammetry-produced DEMs

| Volumetric Difference: Modified Channel | | | | |
|---|---|---|---|---|
| Attribute | Raw | Thresholded | ± Error Volume | % Error |
| AREAL: | | | | |
| Total Area of Erosion (m²) | 4,924.69 | 3,048.45 | | |
| Total Area of Deposition (m²) | 5,003.25 | 2,139.37 | | |
| Total Area of Detectable Change (m²) | NA | 5,187.82 | | |
| Total Area of Interest (m²) | 9,927.94 | NA | | |
| Percent of Area of Interest with Detectable Change | NA | 52.25% | | |
| VOLUMETRIC: | | | | |
| Total Volume of Erosion (m³) | 2,423.33 | 2,261.39 ± | 609.69 | 26.96 |
| Total Volume of Deposition (m³) | 1,508.19 | 1,218.58 ± | 427.87 | 35.11 |
| Total Volume of Difference (m³) | 3,931.52 | 3,479.98 ± | 1,037.56 | 29.82 |
| Total Net Volume Difference (m³) | -915.14 | -1,042.81 ± | 744.85 | -71.43 |
| VERTICAL AVERAGES: | | | | |
| Average Depth of Erosion (m) | 0.49 | 0.74 ± | 0.2 | 26.96 |
| Average Depth of Deposition (m) | 0.3 | 0.57 ± | 0.2 | 35.11 |
| Average Total Thickness of Difference (m) for Area of Interest | 0.4 | 0.35 ± | 0.1 | 29.82 |
| Average Net Thickness of Difference (m) for Area of Interest | -0.09 | -0.11 ± | 0.08 | -71.43 |
| Average Total Thickness of Difference (m) for Area with Detectable Change | NA | 0.67 ± | 0.2 | 29.82 |
| Average Net Thickness of Difference (m) for Area with Detectable Change | NA | -0.2 ± | 0.14 | -71.43 |
| PERCENTAGES (BY VOLUME): | | | | |
| Percent Erosion | 61.64 | 64.98 | | |
| Percent Deposition | 38.36 | 35.02 | | |
| Percent Imbalance (departure from equilibium) | -11.64 | -14.98 | | |
| Net to Total Volume Ratio | -23.28 | -29.97 | | |

## D.8 Channel Calculations Based on RTK DEMs

**Table D.5:** Volumetric differencing results of 2016-2017 RTK-produced DEMs

| Attribute | Raw | Thresholded | ± Error Volume | % Error |
|---|---|---|---|---|
| AREAL: | | | | |
| Total Area of Erosion ($m^2$) | 5,242.32 | 1,737.39 | | |
| Total Area of Deposition ($m^2$) | 3,795.53 | 1,091.82 | | |
| Total Area of Detectable Change ($m^2$) | NA | 2,829.21 | | |
| Total Area of Interest ($m^2$) | 9,037.85 | NA | | |
| Percent of Area of Interest with Detectable Change | NA | 31.30% | | |
| VOLUMETRIC: | | | | |
| Total Volume of Erosion ($m^3$) | 1,220.13 | 886.81 ± | 347.48 | 39.18 |
| Total Volume of Deposition ($m^3$) | 625.9 | 394.95 ± | 218.36 | 55.29 |
| Total Volume of Difference ($m^3$) | 1,846.03 | 1,281.77 ± | 565.84 | 44.15 |
| Total Net Volume Difference ($m^3$) | -594.22 | -491.86 ± | 410.39 | -83.44 |
| VERTICAL AVERAGES: | | | | |
| Average Depth of Erosion (m) | 0.23 | 0.51 ± | 0.2 | 39.18 |
| Average Depth of Deposition (m) | 0.16 | 0.36 ± | 0.2 | 55.29 |
| Average Total Thickness of Difference (m) for Area of Interest | 0.2 | 0.14 ± | 0.06 | 44.15 |
| Average Net Thickness of Difference (m) for Area of Interest | -0.07 | -0.05 ± | 0.05 | -83.44 |
| Average Total Thickness of Difference (m) for Area with Detectable Change | NA | 0.45 ± | 0.2 | 44.15 |
| Average Net Thickness of Difference (m) for Area with Detectable Change | NA | -0.17 ± | 0.15 | -83.44 |
| PERCENTAGES (BY VOLUME): | | | | |
| Percent Erosion | 66.09 | 69.19 | | |
| Percent Deposition | 33.91 | 30.81 | | |
| Percent Imbalance (departure from equilibium) | -16.09 | -19.19 | | |
| Net to Total Volume Ratio | -32.19 | -38.37 | | |

## D.9 Grain Size Distribution Comparisons

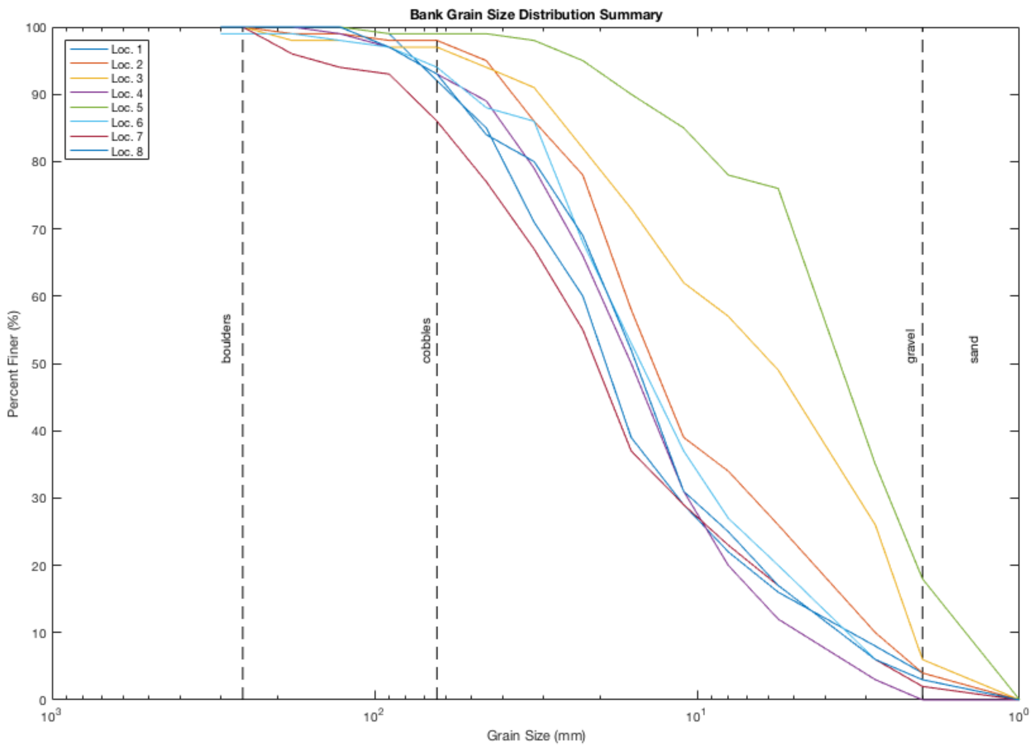


**Figure D.13:** Grain size analysis conducted in 2017 along the channel banks.

## D.10 Kriged Delta Bathymetry

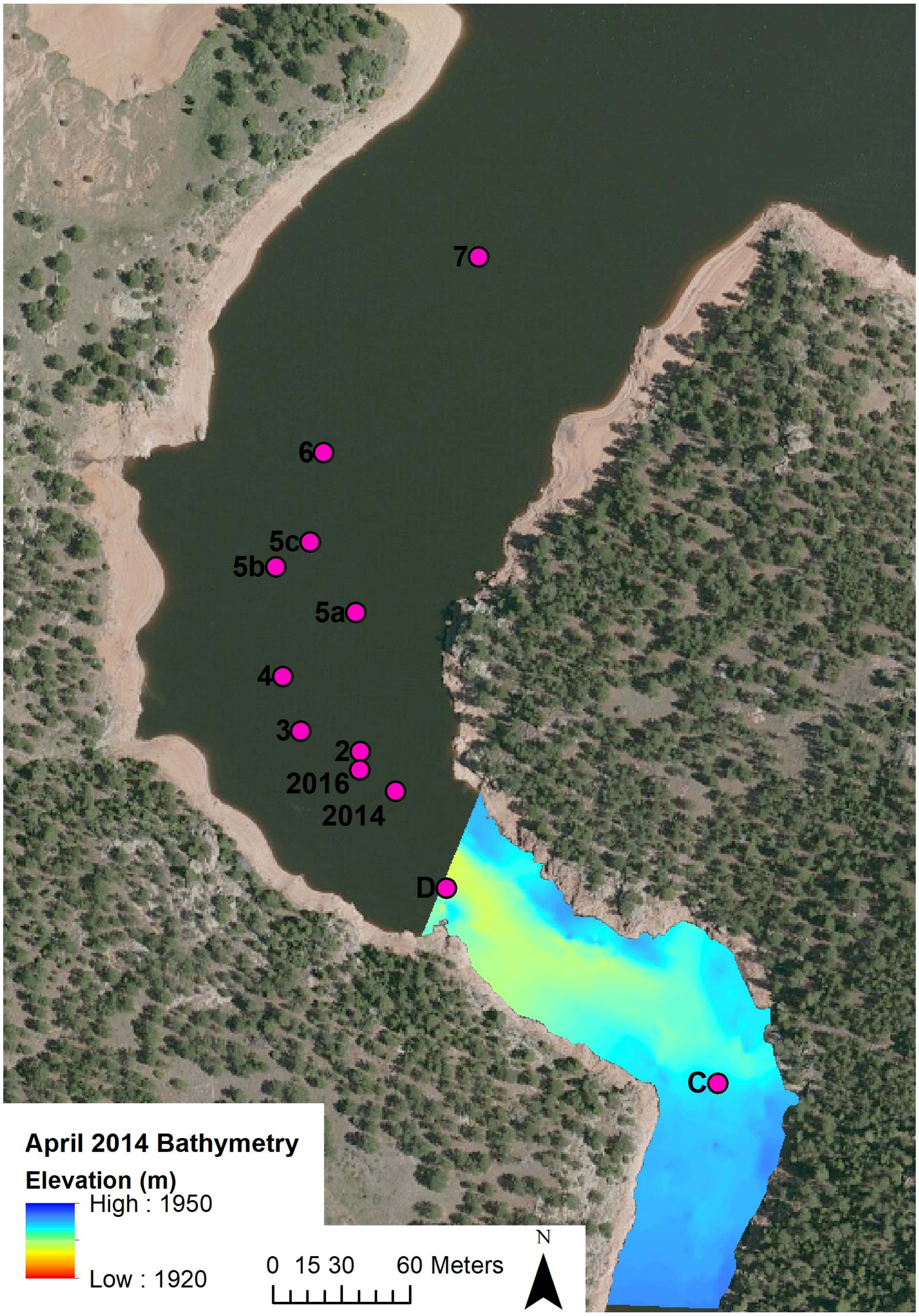


**Figure D.14:** April 2014 bathymetry

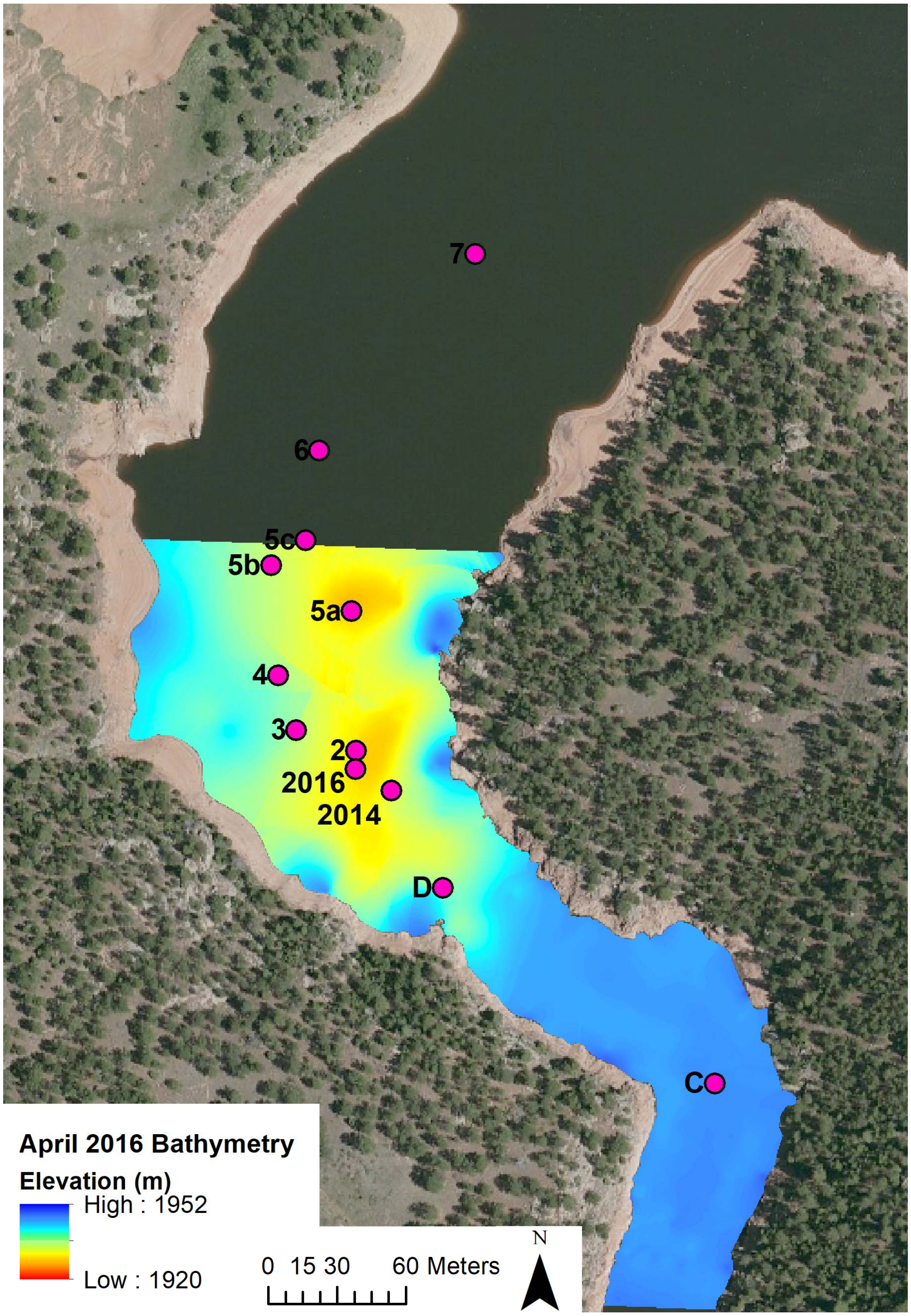


**Figure D.15:** April 2016 bathymetry

## D.11 2014-2017 Bathymetry Change Detection

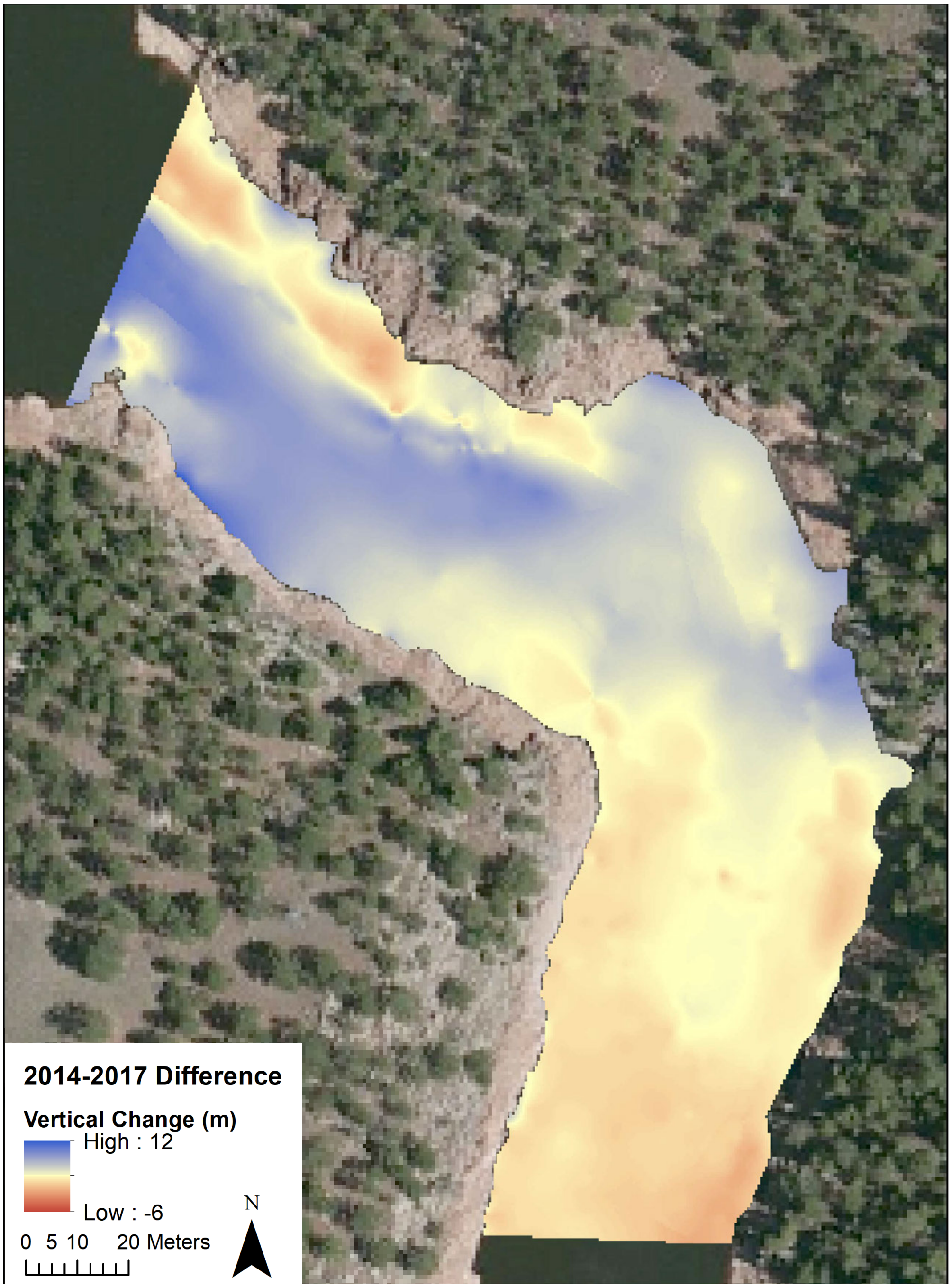


**Figure D.16:** Difference 2014-2017

# D.12 EVS Bathymetry Change Detection Model

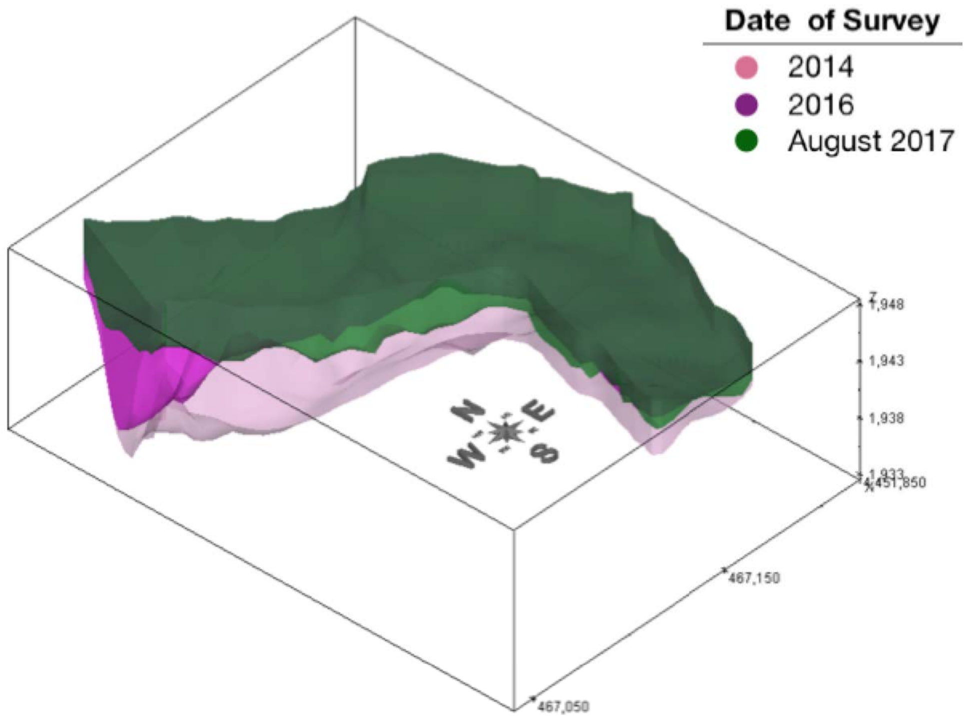


**Figure D.17:** The bathymetry model differencing output produced in EVS.

## D.13 Core Analysis Results

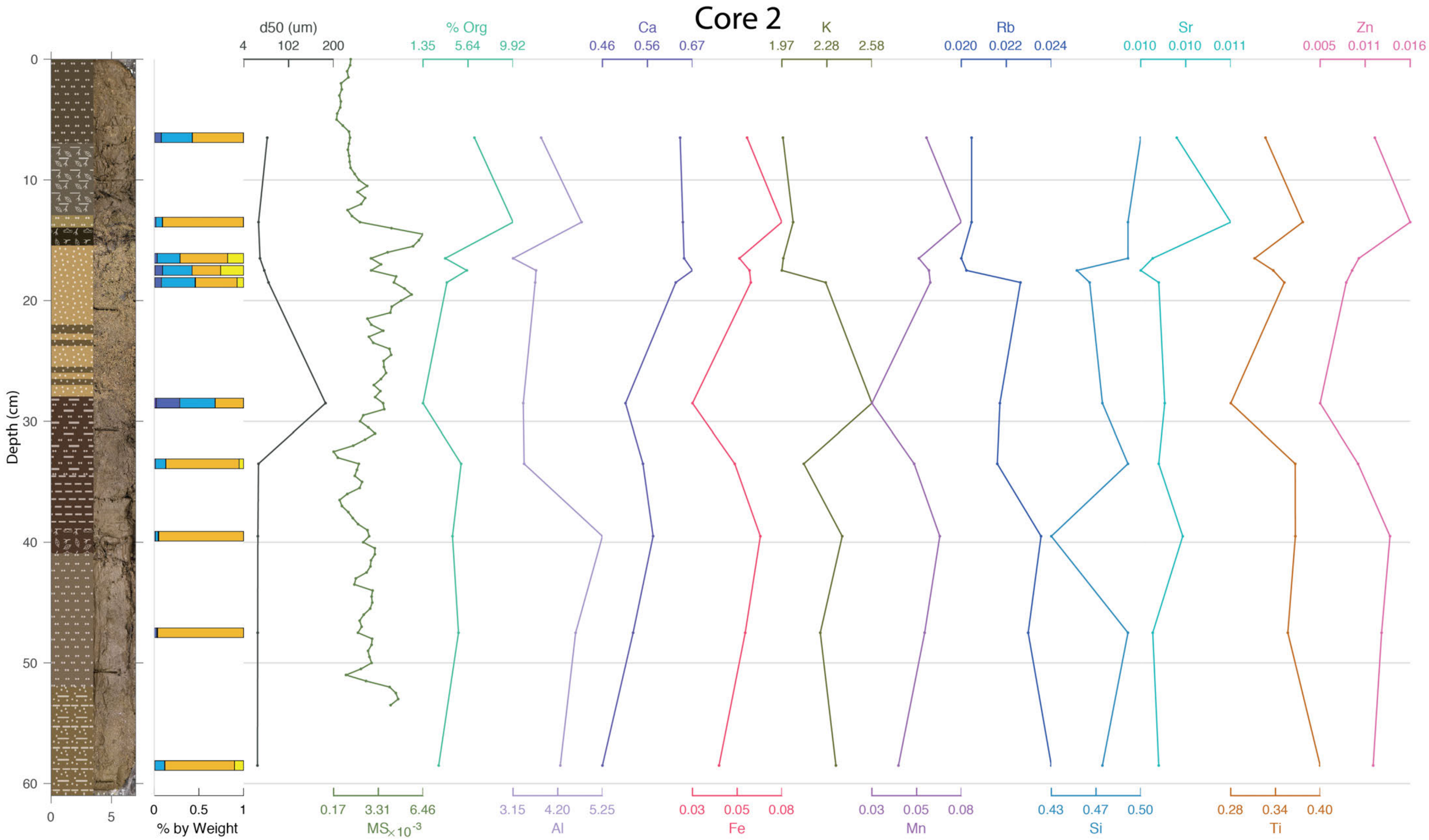


**Figure D.18:** Core 2 XRF, visual stratigraphy and grain size analysis results.

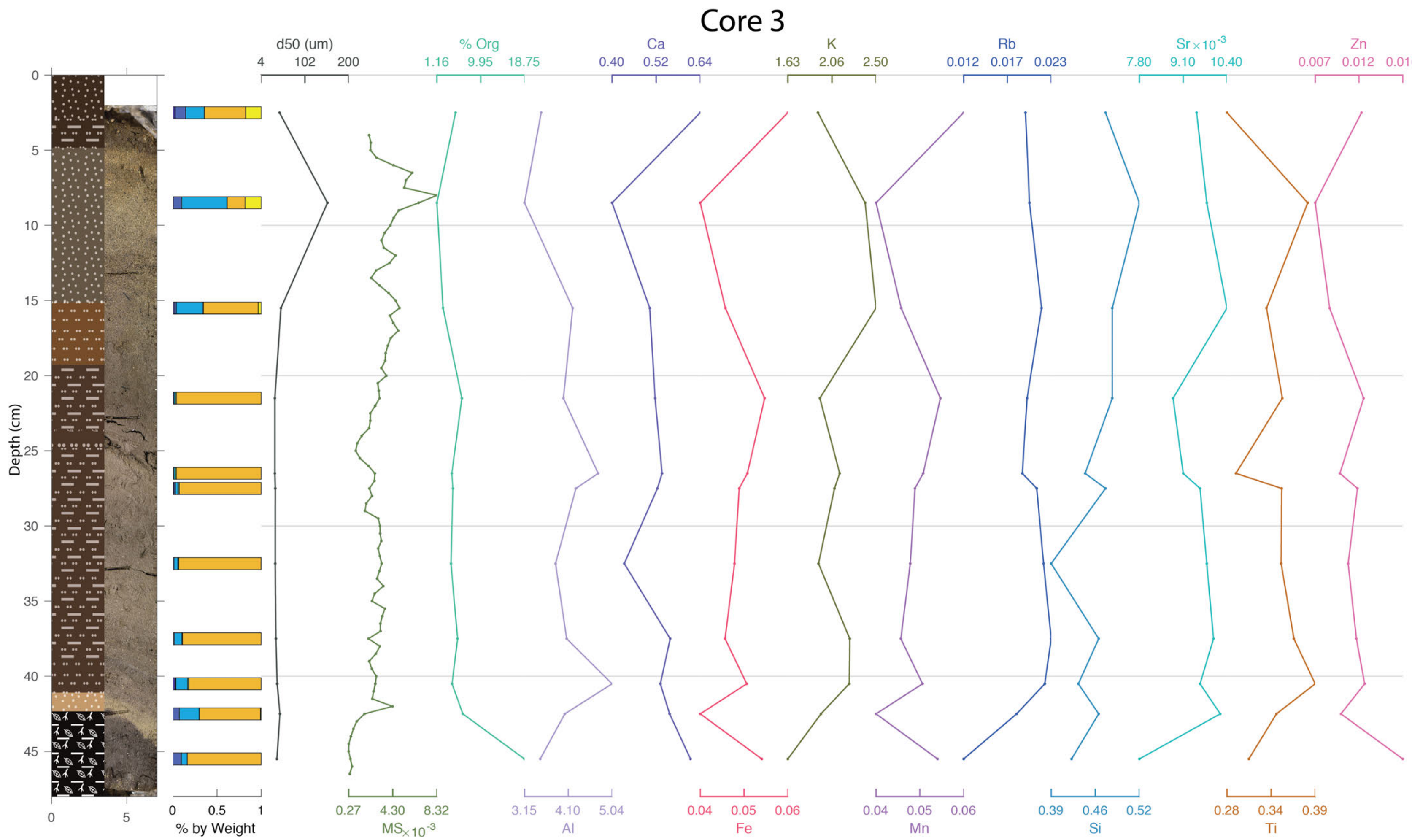


**Figure D.19:** Core 3 XRF, visual stratigraphy and grain size analysis results.

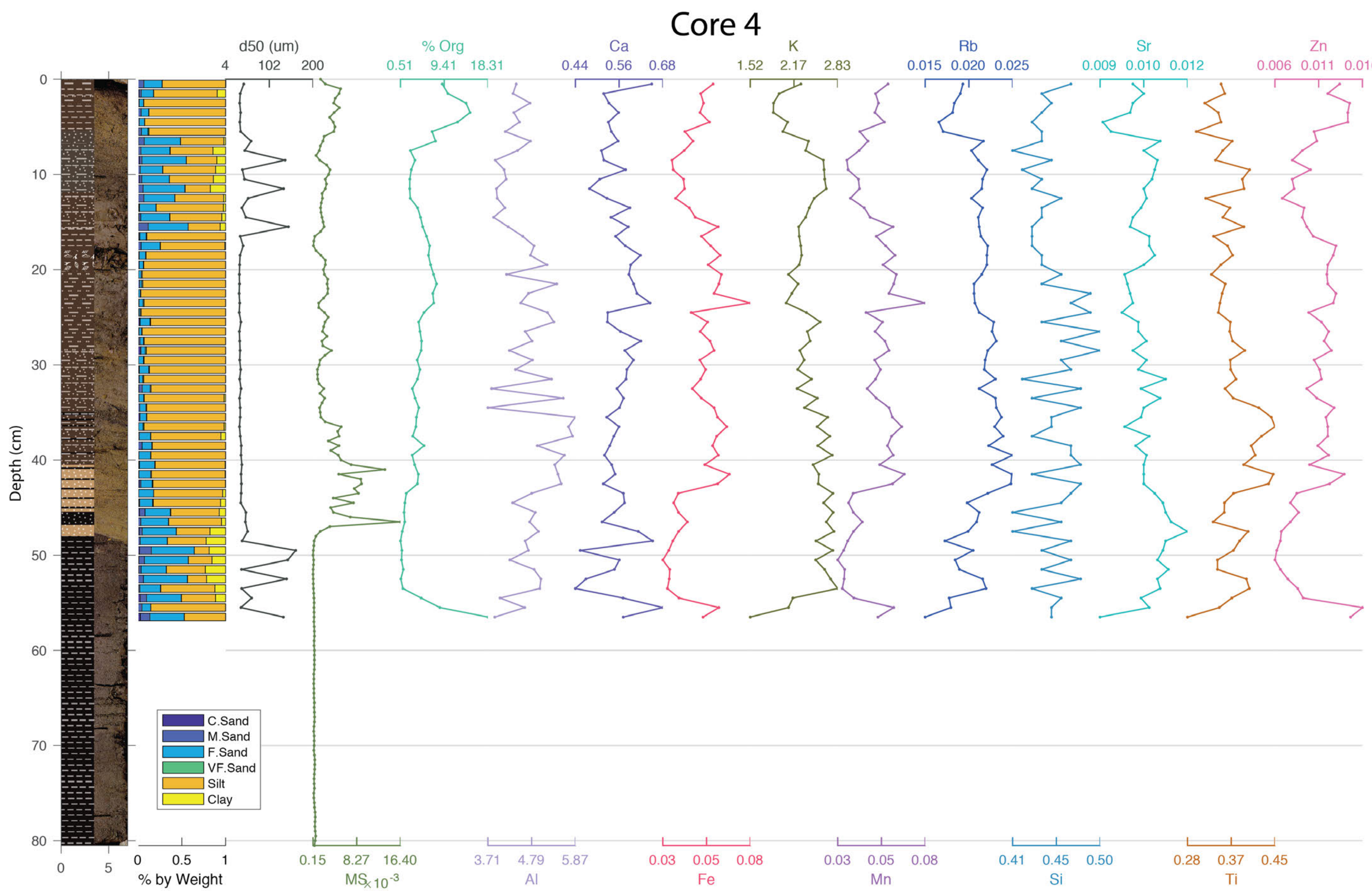


**Figure D.20:** Core 4 XRF, visual stratigraphy and grain size analysis results.

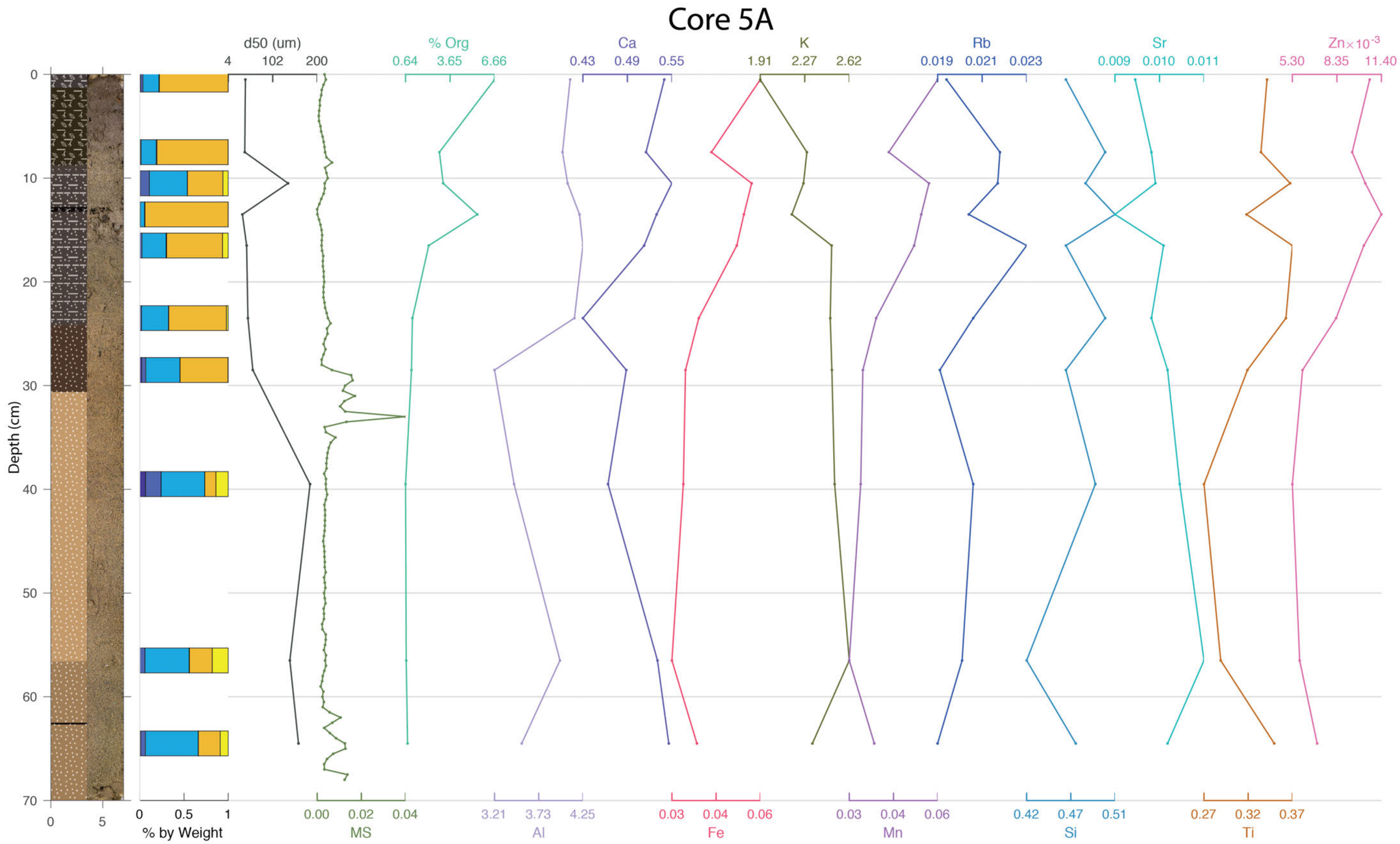


**Figure D.21:** Core 5a XRF, visual stratigraphy and grain size analysis results.

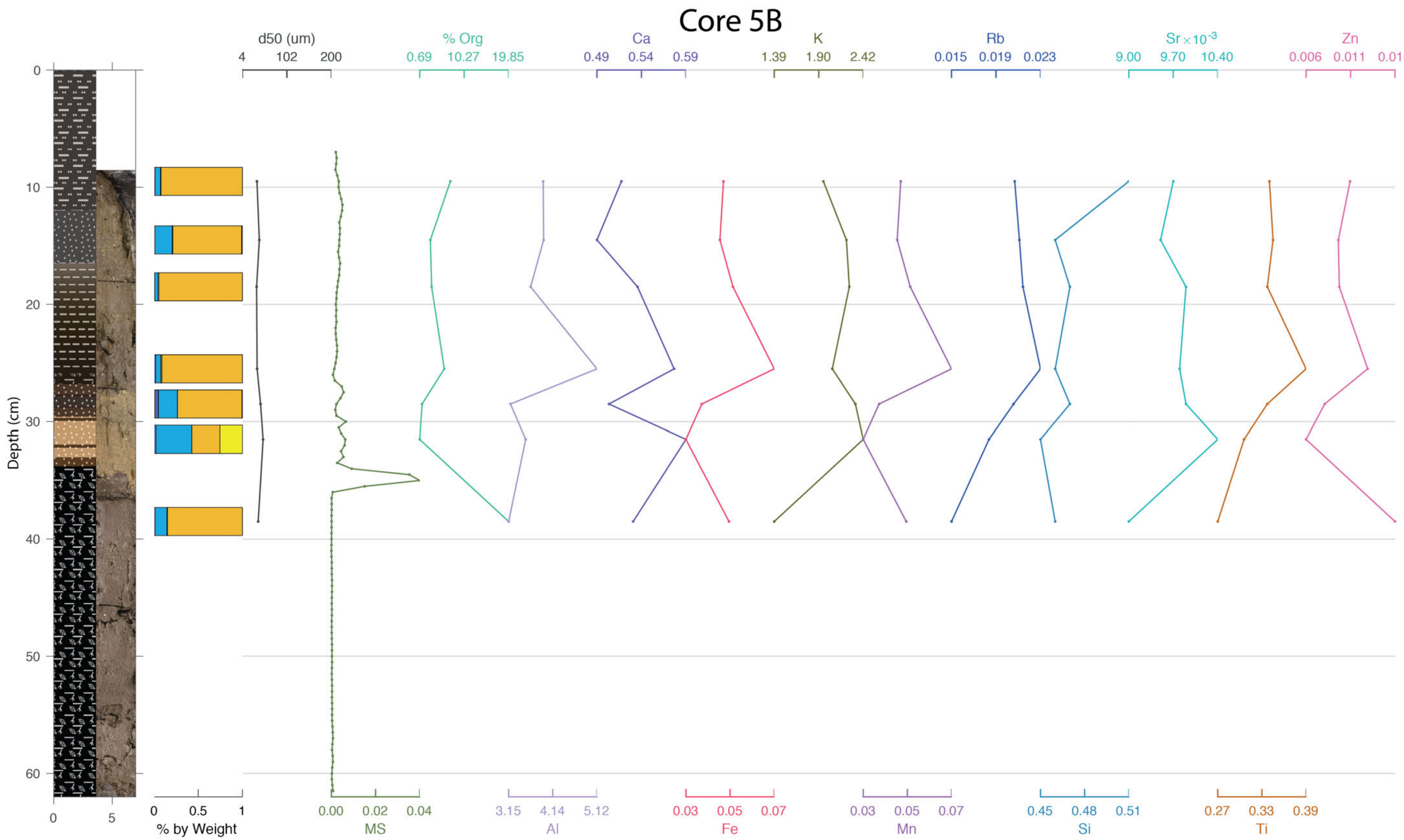


**Figure D.22:** Core 5b XRF, visual stratigraphy and grain size analysis results.

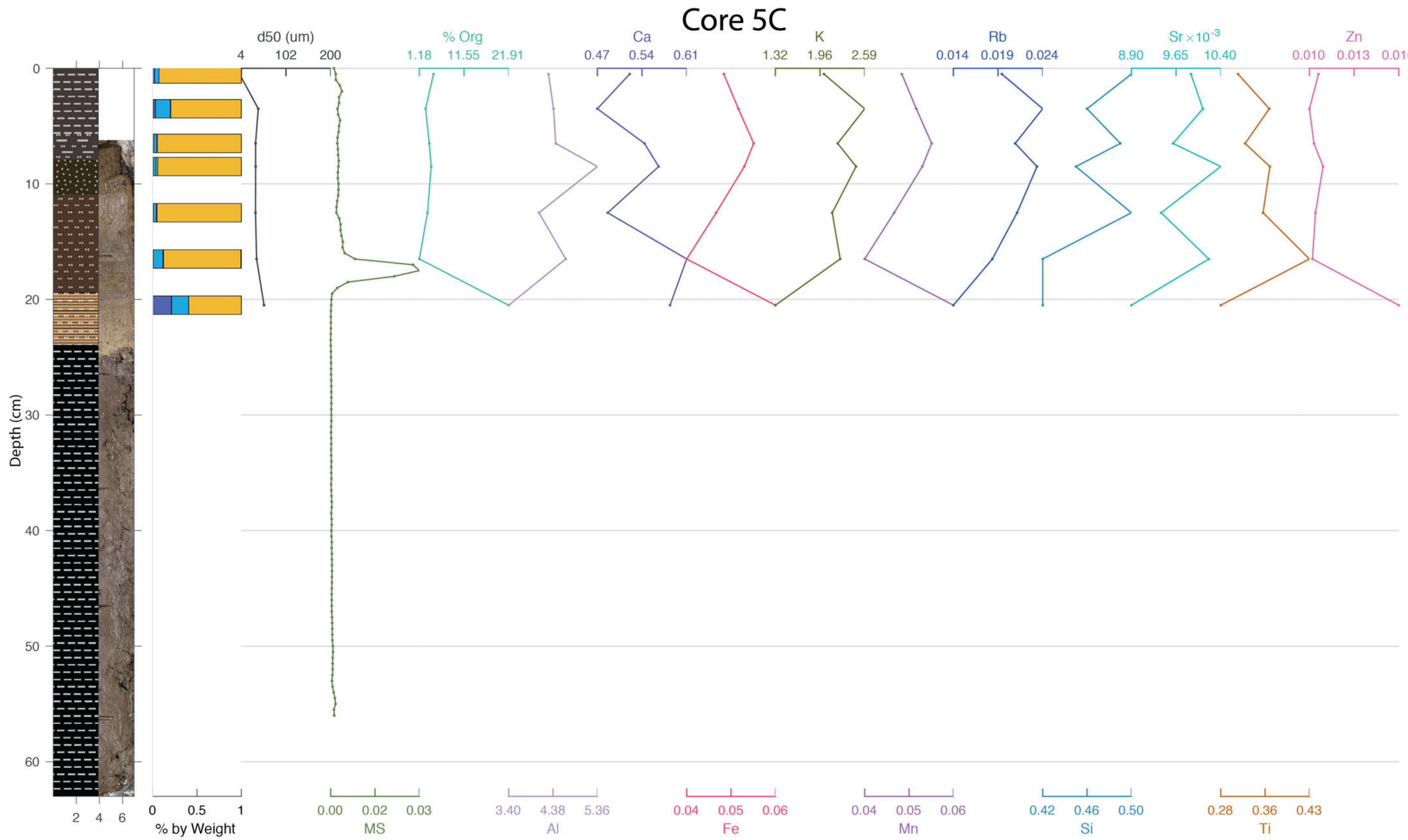


**Figure D.23:** Core 5c XRF, visual stratigraphy and grain size analysis results.

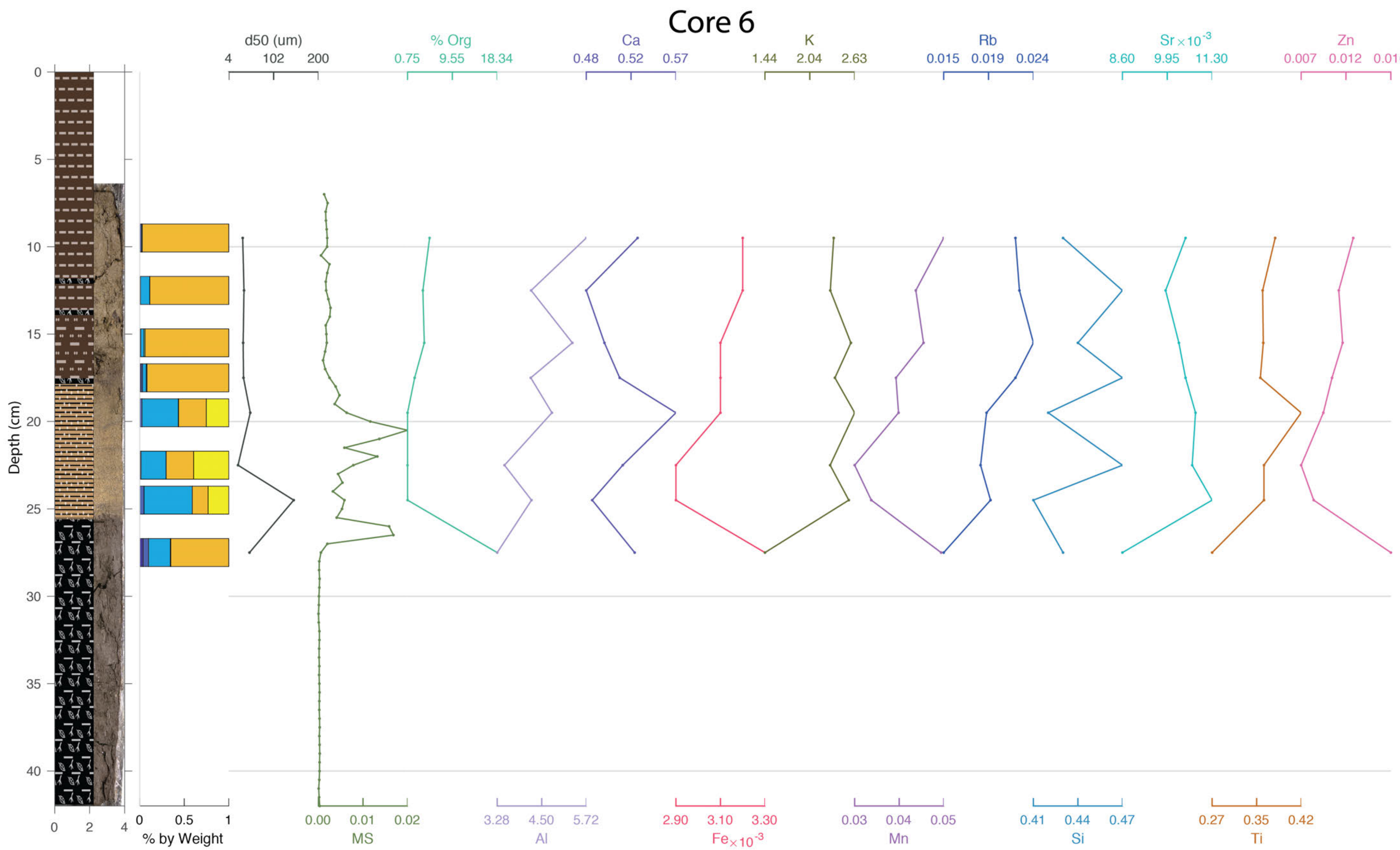


**Figure D.24:** Core 6 XRF, visual stratigraphy and grain size analysis results.

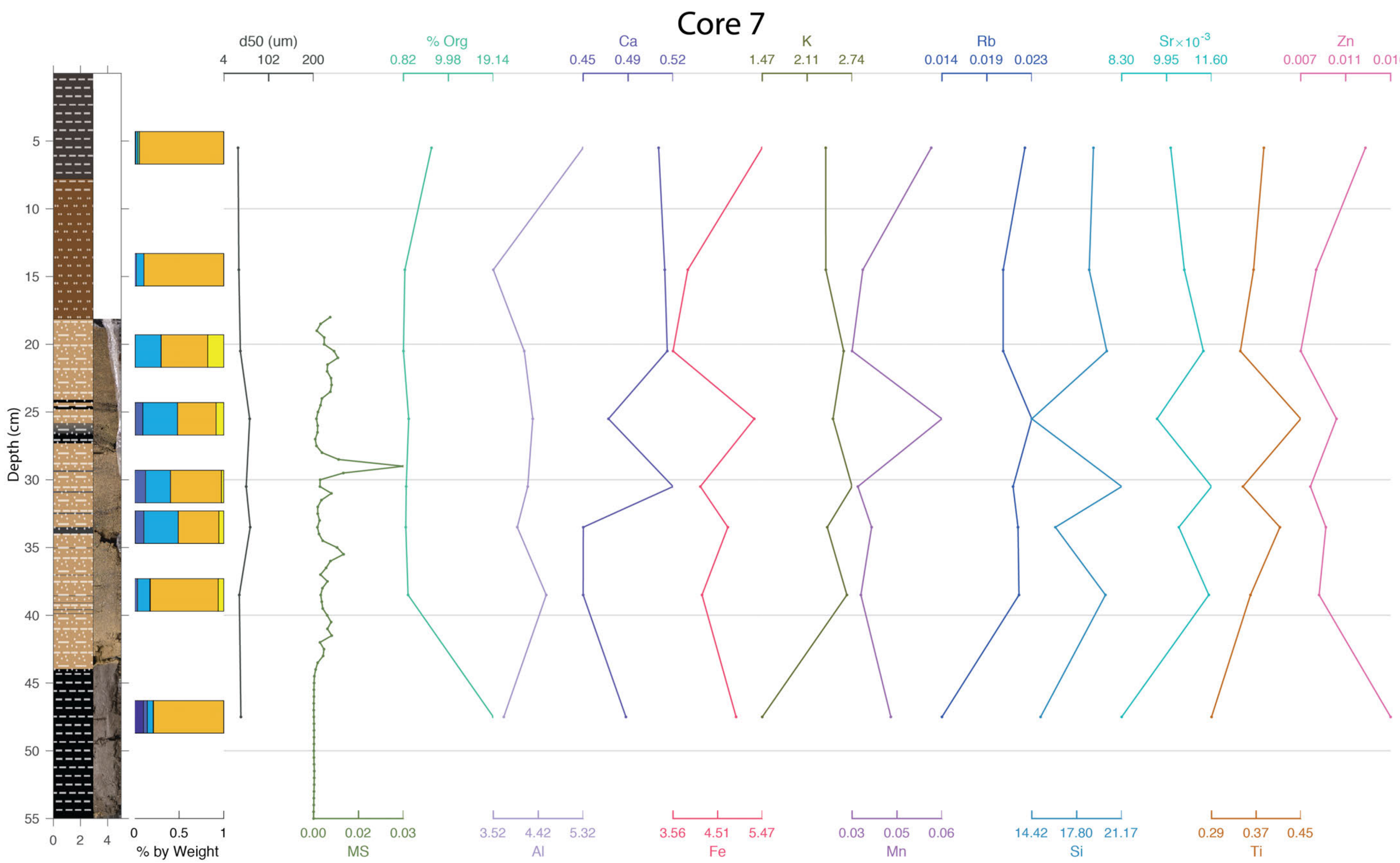


**Figure D.25:** Core 7 XRF, visual stratigraphy and grain size analysis results.

# D.14 Core C and D Grain Size Analyses

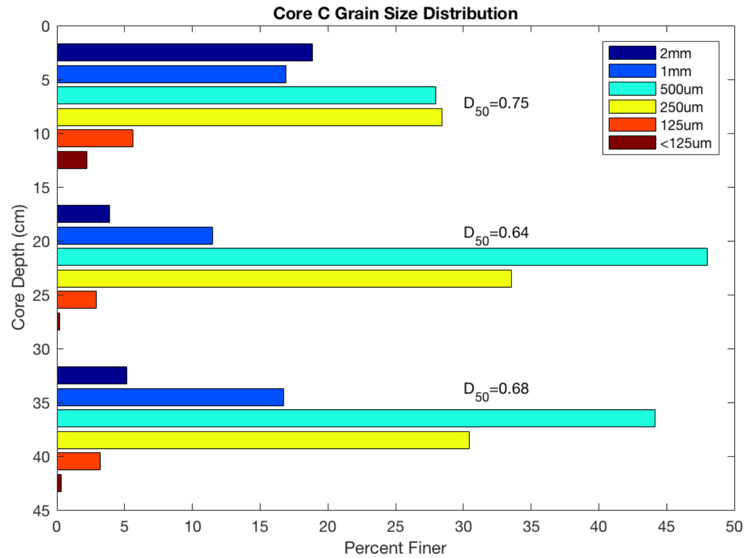


**Figure D.26:** Core C grain size results

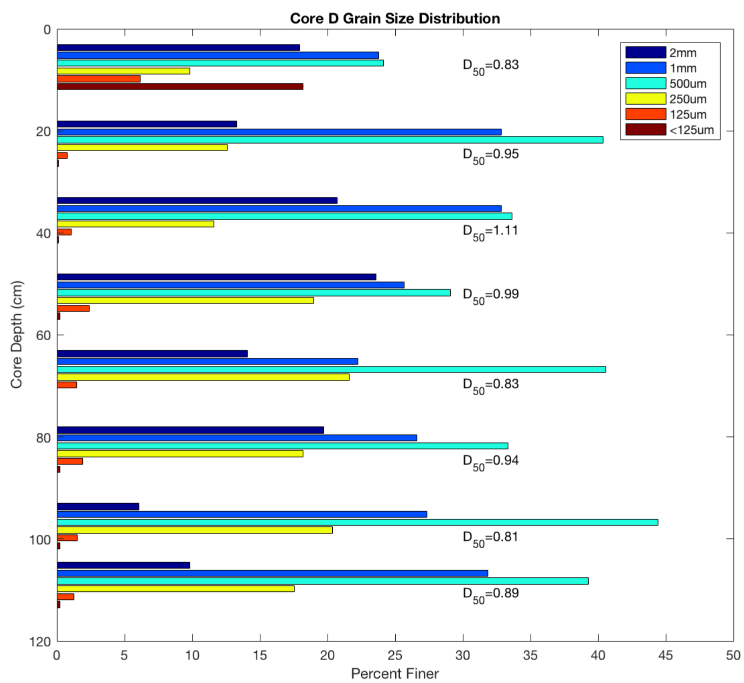


**Figure D.27:** Core D grain size results

**Table D.6:** Core C grain size analysis data.

| | Core C | | |
|---|---|---|---|
| **Depth** | 0-15cm | 15-30cm | 30-45cm |
| **Sample Name** | A (Sample 1) | B (Sample 2) | C (Sample 3) |
| 2+mm | | | |
| Tray mass (g) | 2.5 | 2.51 | 2.5 |
| Dry Sed+Tray Mass (g) | 23.51 | 6.8 | 8.18 |
| Dry Sed Mass (g) | 21.01 | 4.29 | 5.68 |
| 1mm | | | |
| Tray mass (g) | 2.54 | 2.54 | 2.54 |
| Dry Sed+Tray Mass (g) | 21.35 | 15.26 | 20.87 |
| Dry Sed Mass (g) | 18.81 | 12.72 | 18.33 |
| 500um | | | |
| Tray mass (g) | 2.5 | 2.49 | 2.49 |
| Dry Sed+Tray Mass (g) | 33.63 | 55.68 | 50.92 |
| Dry Sed Mass (g) | 31.13 | 53.19 | 48.43 |
| 250um | | | |
| Tray mass (g) | 2.51 | 2.54 | 2.54 |
| Dry Sed+Tray Mass (g) | 34.17 | 39.72 | 35.89 |
| Dry Sed Mass (g) | 31.66 | 37.18 | 33.35 |
| 125um | | | |
| Tray mass (g) | 2.53 | 2.5 | 2.53 |
| Dry Sed+Tray Mass (g) | 8.81 | 5.7 | 6.01 |
| Dry Sed Mass (g) | 6.28 | 3.2 | 3.48 |
| <125um | | | |
| Tray mass (g) | 2.5 | 2.49 | 2.49 |
| Dry Sed+Tray Mass (g) | 4.97 | 2.74 | 2.86 |
| Dry Sed Mass (g) | 2.47 | 0.25 | 0.37 |
| **Percent Mass Calculation** | | | |
| 2mm | 18.87 | 3.87 | 5.18 |
| 1mm | 16.89 | 11.48 | 16.72 |
| 500um | 27.95 | 47.99 | 44.17 |
| 250um | 28.43 | 33.55 | 30.42 |
| 125um | 5.64 | 2.89 | 3.17 |
| <125um | 2.22 | 0.23 | 0.34 |
| Total Mass (g) | 111.36 | 110.83 | 109.64 |
| **Cumulative Percent** | | | |
| 2mm | 18.87 | 3.87 | 5.18 |
| 1mm | 35.76 | 15.35 | 21.90 |
| 500um | 63.71 | 63.34 | 66.07 |
| 250um | 92.14 | 96.89 | 96.49 |
| 125um | 97.78 | 99.77 | 99.66 |
| <125um | 100.00 | 100.00 | 100.00 |
| **D50 (mm)** | 0.75 | 0.64 | 0.68 |

**Table D.7:** Core D grain size analysis data.

| | Core D | | | | | | | |
|---|---|---|---|---|---|---|---|---|
| **Depth** | 0-15cm | 15-30cm | 30-45cm | 45-60cm | 60-75cm | 75-90cm | 90-105cm | 105-113cm |
| **Sample Name** | D (Sample 1) | E (Sample 2) | F (Sample 3) | G (Sample 4) | H (Sample 5) | I (Sample 6) | J (Sample 7) | K (Sample 8) |
| 2+mm | | | | | | | | |
| Tray mass (g) | 2.5 | 2.5 | 2.5 | 2.5 | 2.5 | 2.5 | 2.5 | 2.5 |
| Dry Sed+Tray Mass (g) | 21.73 | 17 | 25.36 | 28.45 | 18.02 | 24.04 | 9.13 | 12.72 |
| Dry Sed Mass (g) | 19.23 | 14.5 | 22.86 | 25.95 | 15.52 | 21.54 | 6.63 | 10.22 |
| 1mm | | | | | | | | |
| Tray mass (g) | 2.54 | 2.54 | 2.54 | 2.54 | 2.54 | 2.54 | 2.54 | 2.54 |
| Dry Sed+Tray Mass (g) | 28.04 | 38.32 | 38.8 | 30.74 | 27.06 | 31.59 | 32.34 | 35.75 |
| Dry Sed Mass (g) | 25.5 | 35.78 | 36.26 | 28.2 | 24.52 | 29.05 | 29.8 | 33.21 |
| 500um | | | | | | | | |
| Tray mass (g) | 2.49 | 2.49 | 2.49 | 2.49 | 2.49 | 2.49 | 2.49 | 2.49 |
| Dry Sed+Tray Mass (g) | 28.35 | 46.44 | 39.58 | 34.48 | 47.15 | 38.9 | 50.92 | 43.42 |
| Dry Sed Mass (g) | 25.86 | 43.95 | 37.09 | 31.99 | 44.66 | 36.41 | 48.43 | 40.93 |
| 250um | | | | | | | | |
| Tray mass (g) | 2.54 | 2.54 | 2.52 | 2.51 | 2.51 | 2.54 | 2.54 | 2.54 |
| Dry Sed+Tray Mass (g) | 13.09 | 16.24 | 15.31 | 23.36 | 26.33 | 22.42 | 24.75 | 20.82 |
| Dry Sed Mass (g) | 10.55 | 13.7 | 12.79 | 20.85 | 23.82 | 19.88 | 22.21 | 18.28 |
| 125um | | | | | | | | |
| Tray mass (g) | 2.49 | 2.53 | 2.53 | 2.49 | 2.52 | 2.53 | 2.48 | 2.52 |
| Dry Sed+Tray Mass (g) | 9.1 | 3.39 | 3.73 | 5.15 | 4.15 | 4.6 | 4.15 | 3.84 |
| Dry Sed Mass (g) | 6.61 | 0.86 | 1.2 | 2.66 | 1.63 | 2.07 | 1.67 | 1.32 |
| <125um | | | | | | | | |
| Tray mass (g) | 2.5 | 2.49 | 2.49 | 2.49 | 2.52 | 2.5 | 2.49 | 2.52 |
| Dry Sed+Tray Mass (g) | 21.99 | 2.6 | 2.63 | 2.75 | 2.52 | 2.76 | 2.74 | 2.74 |
| Dry Sed Mass (g) | 19.49 | 0.11 | 0.14 | 0.26 | 0 | 0.26 | 0.25 | 0.22 |
| **Percent Mass Calculation** | | | | | | | | |
| 2mm | 17.93 | 13.31 | 20.72 | 23.61 | 14.09 | 19.72 | 6.08 | 9.81 |
| 1mm | 23.78 | 32.86 | 32.86 | 25.66 | 22.26 | 26.60 | 27.34 | 31.88 |
| 500um | 24.11 | 40.36 | 33.61 | 29.11 | 40.54 | 33.34 | 44.44 | 39.29 |
| 250um | 9.84 | 12.58 | 11.59 | 18.97 | 21.63 | 18.20 | 20.38 | 17.55 |
| 125um | 6.16 | 0.79 | 1.09 | 2.42 | 1.48 | 1.90 | 1.53 | 1.27 |
| <125um | 18.17 | 0.10 | 0.13 | 0.24 | 0.00 | 0.24 | 0.23 | 0.21 |
| Total Mass (g) | 107.24 | 108.9 | 110.34 | 109.91 | 110.15 | 109.21 | 108.99 | 104.18 |
| **Cumulative Percent** | | | | | | | | |
| 2mm | 17.93 | 13.31 | 20.72 | 23.61 | 14.09 | 19.72 | 6.08 | 9.81 |
| 1mm | 41.71 | 46.17 | 53.58 | 49.27 | 36.35 | 46.32 | 33.43 | 41.69 |
| 500um | 65.82 | 86.53 | 87.19 | 78.37 | 76.90 | 79.66 | 77.86 | 80.98 |
| 250um | 75.66 | 99.11 | 98.79 | 97.34 | 98.52 | 97.87 | 98.24 | 98.52 |
| 125um | 81.83 | 99.90 | 99.87 | 99.76 | 100.00 | 99.76 | 99.77 | 99.79 |
| <125um | 100.00 | 100.00 | 100.00 | 100.00 | 100.00 | 100.00 | 100.00 | 100.00 |
| **D50 (mm)** | 0.83 | 0.95 | 1.11 | 0.99 | 0.83 | 0.94 | 0.81 | 0.89 |

## D.15 Approximated Pre-Flood Bathymetry

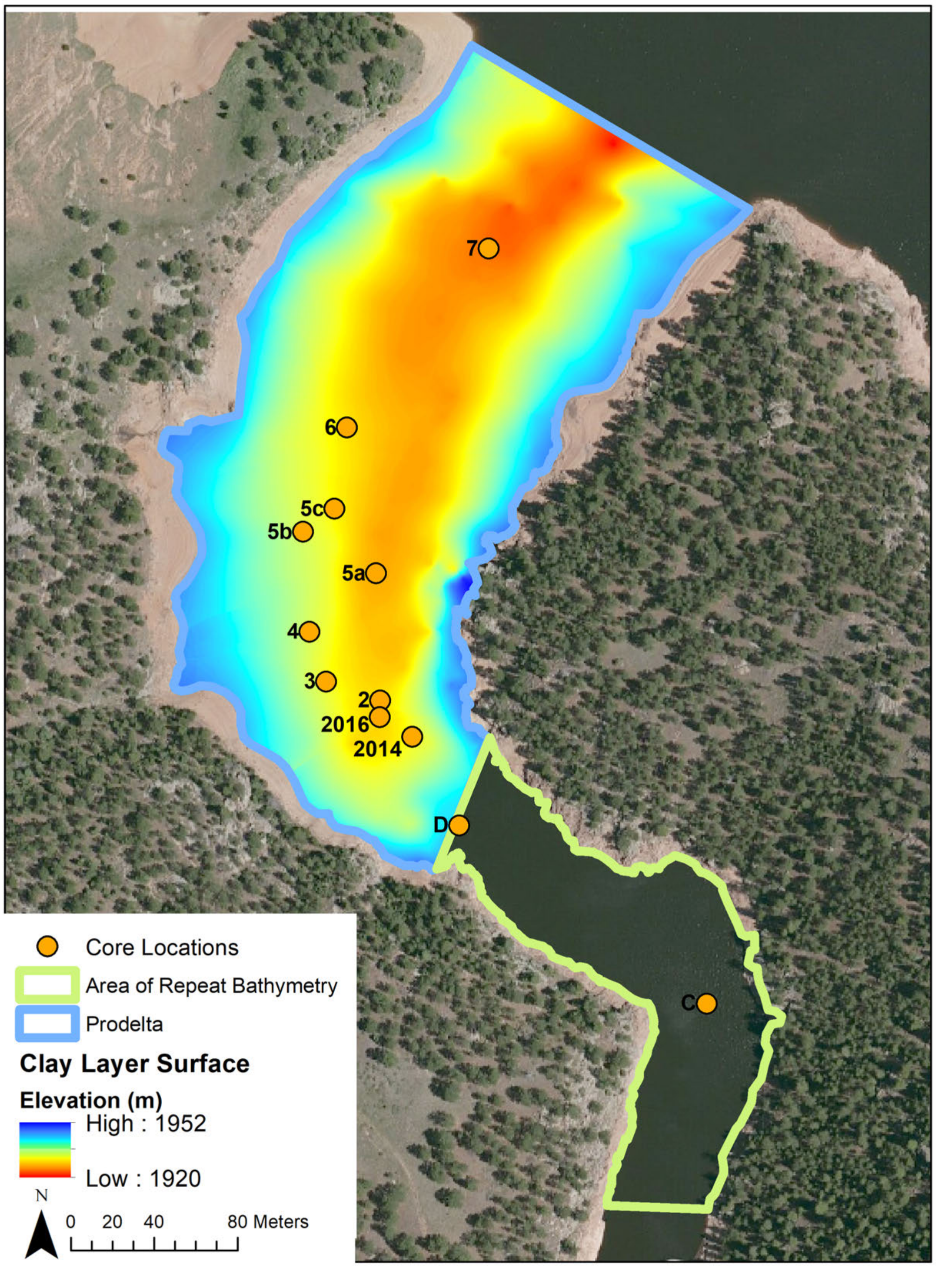


**Figure D.28:** The approximated bathymetry of the prodelta area before the 2013 flood, based on the measured elevation of the pre- and post-flood interface across the eight analyzed cores in the prodelta.

## D.16 Approximated Post-Flood Bathymetry

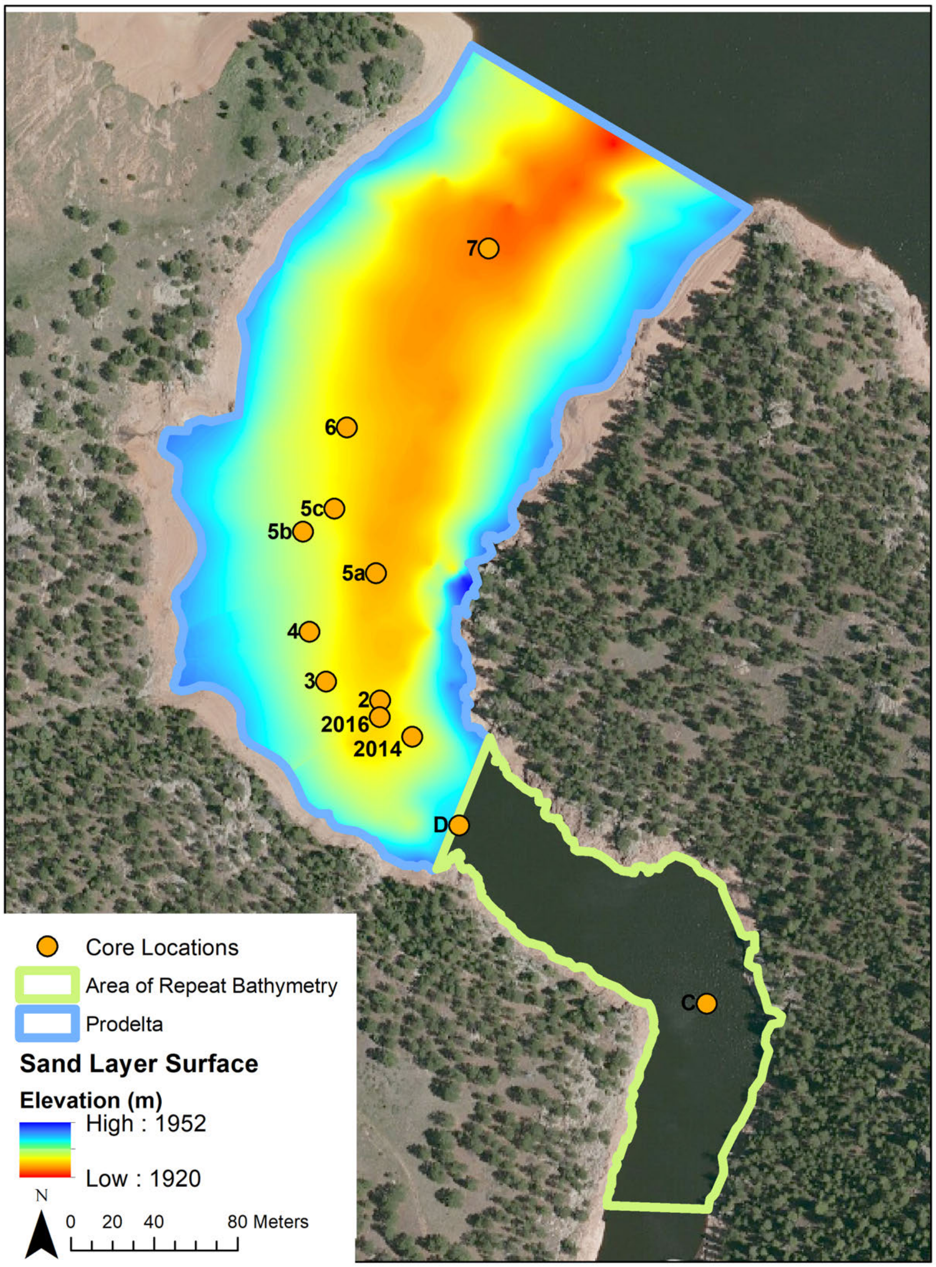


**Figure D.29:** The approximated bathymetry of the prodelta area directly after the September 2013 flood, based on the measured thickness and elevation of thick, sandy tan layer attributed to September 2013 sedimentation.

# Appendix E

# Matlab Scripts Used

## E.1 Bathymetry Survey Mapping Script

```
%Analysis of Bathymetry survey coverage
%Import Data
Data=xlsread('XYDepth-Compiled.xlsx');
X2014=Data(1:1576,1);
Y2014=Data(1:1576,2);
D2014=Data(1:1576,3);
X2016=Data(1:7124,4);
Y2016=Data(1:7124,5);
D2016=Data(1:7124,6);
XMay2017=Data(1:11157,7);
YMay2017=Data(1:11157,8);
DMay2017=Data(1:11157,9);
XAug2017=Data(:,10);
YAug2017=Data(:,11);
DAug2017=Data(:,12);
XDamAug2017=Data(1:11546,13);
YDamAug2017=Data(1:11546,14);
DDamAug2017=Data(1:11546,15);
XDam2016=Data(1:972,16);
YDam2016=Data(1:972,17);
DDam2016=Data(1:972,18);
%Plot Track
figure(1)
h4=plot(XAug2017,YAug2017,'.');
ax = gca;
xt=xticks;
ax.XTickLabel = {xt};
yt=yticks;
ax.YTickLabel = {yt};
hold on
h2=plot(X2016,Y2016,'.');
h3=plot(XMay2017,YMay2017,'.');
h1=plot(X2014,Y2014,'.');
xlabel('Easting (UTM)');
ylabel('Northing (UTM)');
title('Bathymetry Survey Track');
legend([h1 h2 h3 h4],{'2014','2016','May 2017','August 2017'});
hold off
%Calculate width of coverage based on depth
Width2014=D2014*tand(11);
Width2016=D2016*tand(11);
WidthMay2017=DMay2017*tand(11);
WidthAug2017=DAug2017*tand(11);
WidthDamAug2017=DDamAug2017*tand(11);
WidthDam2016=DDam2016*tand(11);
%BufferCalc 2014
X214=X2014+Width2014;
X314=X2014-Width2014;
Y214=Y2014+Width2014;
Y314=Y2014-Width2014;
%Buffer Calc 2016
X216=X2016+Width2016;
X316=X2016-Width2016;
Y216=Y2016+Width2016;
Y316=Y2016-Width2016;
%Buffer Calc May2017
X2May17=XMay2017+WidthMay2017;
X3May17=XMay2017-WidthMay2017;
```

```
Y2May17=YMay2017+WidthMay2017;
Y3May17=YMay2017-WidthMay2017;
%Buffer Calc Aug2017
X2Aug17=XAug2017+WidthAug2017;
X3Aug17=XAug2017-WidthAug2017;
Y2Aug17=YAug2017+WidthAug2017;
Y3Aug17=YAug2017-WidthAug2017;
%Buffer Calc Aug Dam2017
X2DamAug17=XDamAug2017+WidthDamAug2017;
X3DamAug17=XDamAug2017-WidthDamAug2017;
Y2DamAug17=YDamAug2017+WidthDamAug2017;
Y3DamAug17=YDamAug2017-WidthDamAug2017;
%Buffer Calc Dam2016
X2Dam16=XDam2016+WidthDam2016;
X3Dam16=XDam2016-WidthDam2016;
Y2Dam16=YDam2016+WidthDam2016;
Y3Dam16=YDam2016-WidthDam2016;
%Plot on top of Map
%colors
orange=[1,.6445,0];
gold=[1,.8398,0];
darkgreen=[0,.3906,0];
forestgreen=[.1328,.5430,.1328];
purple=[.5,0,.5];
thistle=[.8438,.7461,.8438];
pink=[1,.75,.793];
violetred=[.8555,.4375,.5742];
%plotting
[NSV, R]= geotiffread('Untitled1.tif');
figure(2)
ax = gca;
xt=xticks;
yt=(yticks);
mapshow(NSV, R);

hold on
h9=plot(X2Aug17,YAug2017,'.','color',forestgreen);
h10=plot(X3Aug17,YAug2017,'.','color',forestgreen);
h11=plot(XAug2017,Y2Aug17,'.','color',forestgreen);
h12=plot(XAug2017,Y3Aug17,'.','color',forestgreen);
h4=plot(XAug2017,YAug2017,'.','color',darkgreen);
h21=plot(X2DamAug17,YDamAug2017,'.','color',forestgreen);
h22=plot(X3DamAug17,YDamAug2017,'.','color',forestgreen);
h23=plot(XDamAug2017,Y2DamAug17,'.','color',forestgreen);
h24=plot(XDamAug2017,Y3DamAug17,'.','color',forestgreen);
h25=plot(XDamAug2017,YDamAug2017,'.','color',darkgreen);
h13=plot(XDam2016,YDam2016,'.','color',thistle);
h14=plot(X3Dam16,YDam2016,'.','color',thistle);
h15=plot(XDam2016,Y2Dam16,'.','color',thistle);
h16=plot(XDam2016,Y3Dam16,'.','color',thistle);
h2=plot(XDam2016,YDam2016,'.','color',purple);
h21=plot(X216,Y2016,'.','color',thistle);
h22=plot(X316,Y2016,'.','color',thistle);
h23=plot(X2016,Y216,'.','color',thistle);
h24=plot(X2016,Y316,'.','color',thistle);
h25=plot(X2016,Y2016,'.','color',purple);
h17=plot(X214,Y2014,'.','color',pink);
h18=plot(X314,Y2014,'.','color',pink);
```

```
h19=plot(X2014,Y214,'.','color',pink);
h20=plot(X2014,Y314,'.','color',pink);
h1=plot(X2014,Y2014,'.','color',violetred);
h5=plot(X2May17,YMay2017,'.','color',gold);
h6=plot(X3May17,YMay2017,'.','color',gold);
h7=plot(XMay2017,Y2May17,'.','color',gold);
h8=plot(XMay2017,Y3May17,'.','color',gold);
h3=plot(XMay2017,YMay2017,'.','color',orange);
drawLine([466020 4450650],[466500 4450650]);
text(466150,4450690,['500 Meters'],'Color','white','FontSize',12);

xlabel('Easting (UTM)');
ylabel('Northing (UTM)');
title('Bathymetry Survey Track');
hleg=legend([h1 h2 h3 h4],{'2014','2016','May 2017','August
2017'},'fontsize',12);
title(hleg,'Date  of Survey')
```

## E.2 SGeMs Output Script

```
% Matlab program "read_sgems_output.m"
%
% Created by Michael Ronayne and modified by Johanna Eidmann

nx = 700; ny = 1000;
xsiz = 0.5; ysiz = 0.5;
xmn = 466890; ymn = 4451730;
x = xmn: xsiz : (xmn + ((nx*xsiz)-xsiz));
y = ymn: ysiz:  (ymn + ((ny*ysiz)-ysiz));
cd '/Volumes/NO NAME/Bathymetry-Final10082017/2016'
% ---------------------------------------------------------------------------------
% Read the gslib-formatted file that contains the kriged values
%   (file name = kriged_values_NoHeader.dat)
% ---------------------------------------------------------------------------------
infile = 'krig1000.csv';
sgems_vector = csvread(infile);
sgems_vector(sgems_vector<0)=1948.83024;
n = 1;

for i = ny:-1:1     % Note that i = 1 is the southernmost row!
  for j = 1:nx
    kriged_prop(i,j) = sgems_vector(n);
    n = n+1;
  end
end
% ---------------------------------------------------------------------------------
% Make a 2D plot
figure
imagesc(kriged_prop)
axis equal; axis([0 500 0 500])
colorbar
% ---------------------------------------------------------------------------------
% Make a surface plot
[X,Y] = meshgrid(x,y);
figure
surf(X,Y,kriged_prop)
xlabel('Easting (m)')
ylabel('Northing (m)')
zlabel('Elev (m)')
% ---------------------------------------------------------------------------------
% Write a new output file in x,y,v format
%   (file name = output.dat)
% ---------------------------------------------------------------------------------
outfile = 'output2016.dat'
fid= fopen(outfile,'w');
n = 1;
for i = 1:ny
  for j = 1:nx
    fprintf(fid,'%15.2f%15.2f%15.2f\n',x(j),y(i),sgems_vector(n));
    n = n+1;
  end
end
fclose(fid)
% ---------------------------------------------------------------------------------
% End of program
```

## E.3 XYZ Dense Point Cloud Downsampling Script

**Downsample XYZ File with Polygon**

```
clear all; close all
cd 'C:\Users\admin\Documents\Eidmann_Folder\ChannelSfm'
addpath 'C:\Users\admin\Documents\Eidmann_Folder\ChannelSfm\AprlFinal'

[x,y,z] = xyzread('October2017-03142018-DEM.xyz');
A=x(1:2:end,:);
B=y(1:2:end,:);
C=z(1:2:end,:);
%dat=horzcat(A,B,C);
dat=horzcat(x,y,z);

S = shaperead('polygon_vertices.shp');
PolyX={S(:).X}';
PolyX1=zeros(31,1);
PolyX1=cell2mat(PolyX);
PolyY={S(:).Y}';
PolyY1=zeros(31,1);
PolyY1=cell2mat(PolyY);
figure
plot(PolyX1,PolyY1,'o-');
in=inpolygon(x,y,PolyX1,PolyY1);

b2=dat(in,:);
dlmwrite('October2017__03142018_cloud',b2,'precision',11);
```

**Function used to read XYZ data**

```
function [x,y,z] = xyzread(filename,varargin)

% xyzread simply imports the x,y,z columns of a .xyz file.  Note: there
% is no real standard for .xyz files, so your .xyz file may be different
% from the .xyz files I wrote this for.  I wrote this one for GMT/GIS
% files.
%
%% Syntax
%
% [x,y,z] = xyzread(filename)
% [x,y,z] = xyzread(filename,Name,Value)
%
%% Description
%
% [x,y,z] = xyzread(filename) imports the columns of a plain .xyz file.
%
% [x,y,z] = xyzread(filename,Name,Value) accepts any textscan arguments
% such as 'headerlines' etc.
%
%% Author Info
% This script was written by Chad A. Greene of the University of Texas
% at Austin's Institute for Geophysics (UTIG), April 2016.
% http://www.chadagreene.com
%
% See also xyz2grid and textscan.

%% Error checks:

narginchk(1,inf)
nargoutchk(3,3)
assert(isnumeric(filename)==0,'Input error: filename must ba a string.')
assert(exist(filename,'file')==2,['Cannot find file ',filename,'.'])

%% Open file:

fid = fopen(filename);
T = textscan(fid,'%f %f %f',varargin{:});
fclose(fid);

%% Get scattered data:

x = T{1};
y = T{2};
z = T{3};

end
```

## E.4 Core Analysis Matlab Script

```
Sample script for Core 4 Result Plotting
clear all
cd '/Users/johannaeidmann/Documents/CSU/Research/Data/Coring/Raw Data'
addpath('/Users/johannaeidmann/Documents/CSU/Research/Data/Plotting');
addpath('/Users/johannaeidmann/Documents/CSU/Research/Data/Coring/CorePhotos')
addpath('/Users/johannaeidmann/Documents/CSU/Research/Data/Coring/MagSus');
addpath('/Users/johannaeidmann/Documents/CSU/Research/Data/Coring');
addpath('/Users/johannaeidmann/Documents/CSU/Research/Data/Coring/CorePhotos/Core4')

Core4;
close all;
Images_Core4;
close all;
MagSusGraphing;
close all;
GSAnalysis;
close all;
%======= Data =======
x = Core4_Depth+0.5;
x2 = 80.5;
Core4_MS=zeros(length(Core4_Depth));
Core4_MS=Core4;

%Calculate Cumulative Distribution and Grain Size
Plot6=horzcat(Core4_500PTW,Core4_250PTW,Core4_125PTW,Core4_63_125PTW,Core4_4_63PTW,Core4_4PTW);
Core4_CDF_4um=Core4_4PTW;
Core4_CDF_63um=Core4_4PTW+Core4_4_63PTW;
Core4_CDF_125um=Core4_CDF_63um+Core4_63_125PTW;
Core4_CDF_250um=Core4_CDF_125um+Core4_125PTW;
Core4_CDF_500um=Core4_CDF_250um+Core4_250PTW;
Core4_CDF_1000um=Core4_CDF_500um+Core4_500PTW;
GrainSizes=[4,63,125,250,500];
Plot7=horzcat(Core4_CDF_4um,Core4_CDF_63um,Core4_CDF_125um,...
    Core4_CDF_250um,Core4_CDF_500um);
for i = 1:length(Plot7)
    d50(i)=interp1(Plot7(i,:),GrainSizes,0.5,'linear');
end

y{3} = d50'
y{4} = Core4;
y{5} = Core4_Org;
y{6} = Core4_Al;
y{7} = Core4_Ca;
y{8} = Core4_Fe;
y{9} = Core4_K;
y{10} = Core4_Mn;
y{11} = Core4_Rb;
y{12} = Core4_Si;
y{13} = Core4_Sr;
y{14} = Core4_Ti;
y{15} = Core4_Zn;

% concat=[d50';Core4_Al;Core4_Ca;Core4_Fe;Core4_K;Core4_Mn;Core4_Rb;Core4_Si;Core4_Sr];
% Z=max(concat);
% W=min(concat);

%N = length(y);
N = 15;

xLabels = {'d50 (um)','MS','% Org','Al','Ca','Fe','K','Mn','Rb','Si','Sr','Ti','Zn'};


%======= Stuff =======
% This sets how heavy the plot lines are. 1 is default, tends to look anemic.
LW = 1;
%Colors=rand(15,3);
Colors=[0.9879,0.3507,0.1248;0.1704,0.6855,0.0244;0.2577,0.2941,0.2901;0.3967,0.5306,0.3175;0.0
739,0.8324,0.6536;0.6840,0.5974,0.9569;0.4023,0.3353,0.9357;0.9828,0.2992,0.4578;0.4021,0.4525,
```

```
0.2404;0.6206,0.4226,0.7638;0.1543,0.3596,0.759327383131096;0.2,0.5583,0.7406;0.1611,0.7425,0.7
436;0.7581,0.4243,0.1059;0.8711,0.4293,0.6815;0.8711,0.4293,0.6815;0.8711,0.4293,0.6815;0.8711,
0.4293,0.6815];
%======= Plot =======
H = figure(99);
H.Color = 'white';

for n = 3 : N

% Generate subplot.
    subaxis(1,N+1,n,'SpacingHoriz',0.0,'PaddingRight',0);       % Nx1 stack, nth row

% Grab the current Axis
    A = gca;
    clr = A.ColorOrder; % get default color order
    if n == 4
    plot(y{n},CmInt,'.-','Color', Colors(n,:), 'LineWidth',LW);
    else
    plot(y{n},x, '.-','Color', Colors(n,:), 'LineWidth', LW);
    end
    if n== 3
    xlim([4 200]);
    else
    xlim([min(y{n}) max(y{n})]);
    end
    ylim([0 x2]);
    set(gca,'Ydir','reverse')

    A.Box = 'Off';
    A.LineWidth = LW;

    if n== 3
    xticks = linspace(4,200,3);
    else
    xticks = linspace(min(y{n}), max(y{n}), 3);
    end
    if n==3
    xtickformat('%,.f');
    else
        if (n == 11 | n== 13 | n==15)
            xtickformat('%,.3f');
        else
    xtickformat('%,.2f');
        end
    end
    A.XTick = xticks;

% X-axis formatting
    if n ~= 1
        A.YColor = 'None';
    else
        ylabel('Depth (mm)');
    end

    A.YGrid = 'On';

% Y-axis formatting
    A.XColor = Colors(n,:); % Match the axis color to the line color.
    if mod(n,2) == 1
        A.XAxisLocation = 'Top';

    % Hack to get rid of the X=0 grid line. (Just to see if I could).
    % This should be done after any manual YLim changes.
        hold on
            jnk = plot(A,[0,0], [A.XLim(1) A.XLim(2)], '-', 'Color','White');
        hold off
        uistack(jnk,'top');
    end
```

```
    xlabel(xLabels{n-2});

% Title. Needs to be called on first loop to go at top.
%   if n == 7
%       title({'Core 4 Analyses'}, ...
%               'FontWeight', 'Bold', 'FontSize',12);
    %end
end

subaxis(1,N+1,1,'SpacingVert',0.1,'PaddingRight',0);
B = imrotate(I,0,'bilinear');
RI = imref2d(size(B));
RI.XWorldLimits = [0 7];
RI.YWorldLimits = [0 80.5];
imshow(B,RI),axis on
set(gca,'Ydir','reverse')

subaxis(1,N+1,2,'SpacingVert',0.1,'PaddingRight',0);
barplot=Core4_depth+0.5;
barh(barplot,Plot6,'stacked');
%legend('>500','250-500','125-250','63-125','4-63','<4um','location','southeast');
legend('C.Sand','M.Sand','F.Sand','VF.Sand','Silt','Clay','Position',[77 50 60 60]);
xlim([0 1]);
ylim([0 80.5]);
ax = gca;
ax.XAxis.Color = 'black'
set(gca,'ytick',[]);
 set(gca,'ycolor',[1 1 1])
xlabel('% by Weight')
set(gca,'box','off','ycolor','w')
set(gca,'YDir','reverse');
```

**Subaxis Function**

```
function h=subaxis(varargin)
%SUBAXIS Create axes in tiled positions. (just like subplot)
%   Usage:
%      h=subaxis(rows,cols,cellno[,settings])
%      h=subaxis(rows,cols,cellx,celly[,settings])
%      h=subaxis(rows,cols,cellx,celly,spanx,spany[,settings])
%
% SETTINGS: Spacing,SpacingHoriz,SpacingVert
%           Padding,PaddingRight,PaddingLeft,PaddingTop,PaddingBottom
%           Margin,MarginRight,MarginLeft,MarginTop,MarginBottom
%           Holdaxis
%
%           all units are relative (i.e. from 0 to 1)
%
%           Abbreviations of parameters can be used.. (Eg MR instead of MarginRight)
%           (holdaxis means that it wont delete any axes below.)
%
%
% Example:
%
%   >> subaxis(2,1,1,'SpacingVert',0,'MR',0);
%   >> imagesc(magic(3))
%   >> subaxis(2,'p',.02);
%   >> imagesc(magic(4))
%
% 2001-2014 / Aslak Grinsted  (Feel free to modify this code.)

f=gcf;
UserDataArgsOK=0;
Args=get(f,'UserData');
if isstruct(Args)

UserDataArgsOK=isfield(Args,'SpacingHorizontal')&isfield(Args,'Holdaxis')&isfield(Args,'rows')&
isfield(Args,'cols');
end
OKToStoreArgs=isempty(Args)|UserDataArgsOK;

if isempty(Args)&&(~UserDataArgsOK)
    Args=struct('Holdaxis',0, ...
        'SpacingVertical',0.05,'SpacingHorizontal',0.05, ...
        'PaddingLeft',0,'PaddingRight',0,'PaddingTop',0,'PaddingBottom',0, ...
        'MarginLeft',.1,'MarginRight',.1,'MarginTop',.1,'MarginBottom',.1, ...
        'rows',[],'cols',[]);
end
Args=parseArgs(varargin,Args,{'Holdaxis'},{'Spacing' {'sh','sv'}; 'Padding'
{'pl','pr','pt','pb'}; 'Margin' {'ml','mr','mt','mb'}});

if (length(Args.NumericArguments)>2)
    Args.rows=Args.NumericArguments{1};
    Args.cols=Args.NumericArguments{2};
%remove these 2 numerical arguments
    Args.NumericArguments={Args.NumericArguments{3:end}};
end

if OKToStoreArgs
    set(f,'UserData',Args);
end
switch length(Args.NumericArguments)
   case 0
       return % no arguments but rows/cols....
   case 1
       if numel(Args.NumericArguments{1}) > 1 % restore subplot(m,n,[x y]) behaviour
           [x1 y1] = ind2sub([Args.cols Args.rows],Args.NumericArguments{1}(1)); % subplot and
ind2sub count differently (column instead of row first) --> switch cols/rows
           [x2 y2] = ind2sub([Args.cols Args.rows],Args.NumericArguments{1}(end));
       else
           x1=mod((Args.NumericArguments{1}-1),Args.cols)+1; x2=x1;
```

```
            y1=floor((Args.NumericArguments{1}-1)/Args.cols)+1; y2=y1;
        end
%        x1=mod((Args.NumericArguments{1}-1),Args.cols)+1; x2=x1;
%        y1=floor((Args.NumericArguments{1}-1)/Args.cols)+1; y2=y1;
   case 2
      x1=Args.NumericArguments{1};x2=x1;
      y1=Args.NumericArguments{2};y2=y1;
   case 4
      x1=Args.NumericArguments{1};x2=x1+Args.NumericArguments{3}-1;
      y1=Args.NumericArguments{2};y2=y1+Args.NumericArguments{4}-1;
   otherwise
      error('subaxis argument error')
end

cellwidth=((1-Args.MarginLeft-Args.MarginRight)-(Args.cols-
1)*Args.SpacingHorizontal)/Args.cols;
cellheight=((1-Args.MarginTop-Args.MarginBottom)-(Args.rows-1)*Args.SpacingVertical)/Args.rows;
xpos1=Args.MarginLeft+Args.PaddingLeft+cellwidth*(x1-1)+Args.SpacingHorizontal*(x1-1);
xpos2=Args.MarginLeft-Args.PaddingRight+cellwidth*x2+Args.SpacingHorizontal*(x2-1);
ypos1=Args.MarginTop+Args.PaddingTop+cellheight*(y1-1)+Args.SpacingVertical*(y1-1);
ypos2=Args.MarginTop-Args.PaddingBottom+cellheight*y2+Args.SpacingVertical*(y2-1);

if Args.Holdaxis
    h=axes('position',[xpos1 1-ypos2 xpos2-xpos1 ypos2-ypos1]);
else
    h=subplot('position',[xpos1 1-ypos2 xpos2-xpos1 ypos2-ypos1]);
end
set(h,'box','on');
%h=axes('position',[x1 1-y2 x2-x1 y2-y1]);
set(h,'units',get(gcf,'defaultaxesunits'));
set(h,'tag','subaxis');
if (nargout==0), clear h; end;
```

ParseArgs Function:

```
function ArgStruct=parseArgs(args,ArgStruct,varargin)
% Helper function for parsing varargin.
%
%
% ArgStruct=parseArgs(varargin,ArgStruct[,FlagtypeParams[,Aliases]])
%
% * ArgStruct is the structure full of named arguments with default values.
% * Flagtype params is params that don't require a value. (the value will be set to 1 if it is
present)
% * Aliases can be used to map one argument-name to several argstruct fields
%
%
% example usage:
% --------------
% function parseargtest(varargin)
%
% %define the acceptable named arguments and assign default values
% Args=struct('Holdaxis',0, ...
%        'SpacingVertical',0.05,'SpacingHorizontal',0.05, ...
%        'PaddingLeft',0,'PaddingRight',0,'PaddingTop',0,'PaddingBottom',0, ...
%        'MarginLeft',.1,'MarginRight',.1,'MarginTop',.1,'MarginBottom',.1, ...
%        'rows',[],'cols',[]);
%
% %The capital letters define abrreviations.
% %  Eg. parseargtest('spacingvertical',0) is equivalent to  parseargtest('sv',0)
%
% Args=parseArgs(varargin,Args, ... % fill the arg-struct with values entered by the user
%           {'Holdaxis'}, ... %this argument has no value (flag-type)
%           {'Spacing' {'sh','sv'}; 'Padding' {'pl','pr','pt','pb'}; 'Margin'
{'ml','mr','mt','mb'}});
%
% disp(Args)
%
% Aslak Grinsted 2004

% -------------------------------------------------------------------------
%   Copyright (C) 2002-2004, Aslak Grinsted
%   This software may be used, copied, or redistributed as long as it is not sold and this
copyright notice is reproduced on each copy made.  This routine is provided as is without any
express or implied warranties whatsoever.

persistent matlabver

if isempty(matlabver)
    matlabver=ver('MATLAB');
    matlabver=str2double(matlabver.Version);
end

Aliases={};
FlagTypeParams='';

if (length(varargin)>0)
    FlagTypeParams=lower(strvcat(varargin{1}));  %#ok
    if length(varargin)>1
        Aliases=varargin{2};
    end
end

%---------------Get "numeric" arguments
NumArgCount=1;
while (NumArgCount<=size(args,2))&&(~ischar(args{NumArgCount}))
    NumArgCount=NumArgCount+1;
end
NumArgCount=NumArgCount-1;
if (NumArgCount>0)
    ArgStruct.NumericArguments={args{1:NumArgCount}};
else
```

```
    ArgStruct.NumericArguments={};
end


%--------------Make an accepted fieldname matrix (case insensitive)
Fnames=fieldnames(ArgStruct);
for i=1:length(Fnames)
    name=lower(Fnames{i,1});
    Fnames{i,2}=name; %col2=lower
    Fnames{i,3}=[name(Fnames{i,1}~=name) ' ']; %col3=abreviation letters (those that are
uppercase in the ArgStruct) e.g. SpacingHoriz->sh
    %the space prevents strvcat from removing empty lines
    Fnames{i,4}=isempty(strmatch(Fnames{i,2},FlagTypeParams)); %Does this parameter have a
value?
end
FnamesFull=strvcat(Fnames{:,2}); %#ok
FnamesAbbr=strvcat(Fnames{:,3}); %#ok

if length(Aliases)>0
    for i=1:length(Aliases)
        name=lower(Aliases{i,1});
        FieldIdx=strmatch(name,FnamesAbbr,'exact'); %try abbreviations (must be exact)
        if isempty(FieldIdx)
            FieldIdx=strmatch(name,FnamesFull); %&??????? exact or not?
        end
        Aliases{i,2}=FieldIdx;
        Aliases{i,3}=[name(Aliases{i,1}~=name) ' ']; %the space prevents strvcat from removing
empty lines
        Aliases{i,1}=name; %dont need the name in uppercase anymore for aliases
    end
    %Append aliases to the end of FnamesFull and FnamesAbbr
    FnamesFull=strvcat(FnamesFull,strvcat(Aliases{:,1})); %#ok
    FnamesAbbr=strvcat(FnamesAbbr,strvcat(Aliases{:,3})); %#ok
end

%--------------get parameters--------------------
l=NumArgCount+1;
while (l<=length(args))
    a=args{l};
    if ischar(a)
        paramHasValue=1; % assume that the parameter has is of type 'param',value
        a=lower(a);
        FieldIdx=strmatch(a,FnamesAbbr,'exact'); %try abbreviations (must be exact)
        if isempty(FieldIdx)
            FieldIdx=strmatch(a,FnamesFull);
        end
        if (length(FieldIdx)>1) %shortest fieldname should win
            [mx,mxi]=max(sum(FnamesFull(FieldIdx,:)==' ',2));%#ok
            FieldIdx=FieldIdx(mxi);
        end
        if FieldIdx>length(Fnames) %then it's an alias type.
            FieldIdx=Aliases{FieldIdx-length(Fnames),2};
        end

        if isempty(FieldIdx)
            error(['Unknown named parameter: ' a])
        end
        for curField=FieldIdx' %if it is an alias it could be more than one.
            if (Fnames{curField,4})
                if (l+1>length(args))
                    error(['Expected a value for parameter: ' Fnames{curField,1}])
                end
                val=args{l+1};
            else %FLAG PARAMETER
                if (l<length(args)) %there might be a explicitly specified value for the flag
                    val=args{l+1};
                    if isnumeric(val)
                        if (numel(val)==1)
```

```
                            val=logical(val);
                        else
                            error(['Invalid value for flag-parameter: ' Fnames{curField,1}])
                        end
                    else
                        val=true;
                        paramHasValue=0;
                    end
                else
                    val=true;
                    paramHasValue=0;
                end
            end
            if matlabver>=6
                ArgStruct.(Fnames{curField,1})=val; %try the line below if you get an error
here
            else
                ArgStruct=setfield(ArgStruct,Fnames{curField,1},val); %#ok <-works in old
matlab versions
            end
        end
        l=l+1+paramHasValue; %if a wildcard matches more than one
    else
        error(['Expected a named parameter: ' num2str(a)])
    end
end
```

# Appendix F

# Daily Average Water Discharge in Lyons, CO (2014-2017)

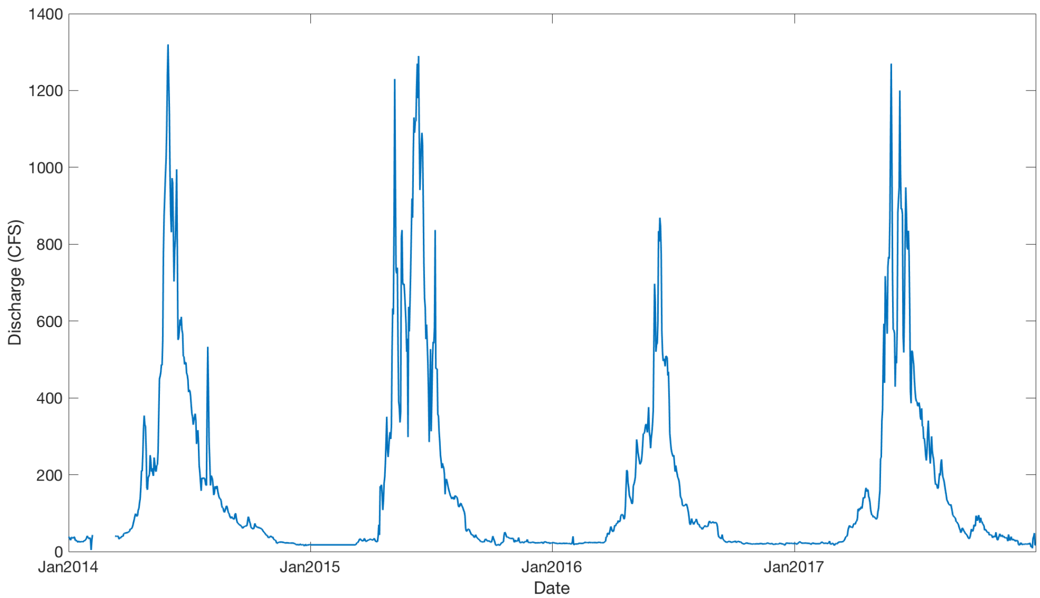


**Figure F.1:** Recorded changes in daily average water discharge of the NSV in Lyons, CO between 2014 and 2017.

# Appendix G

# Conceptual Model of Channel and Delta Response

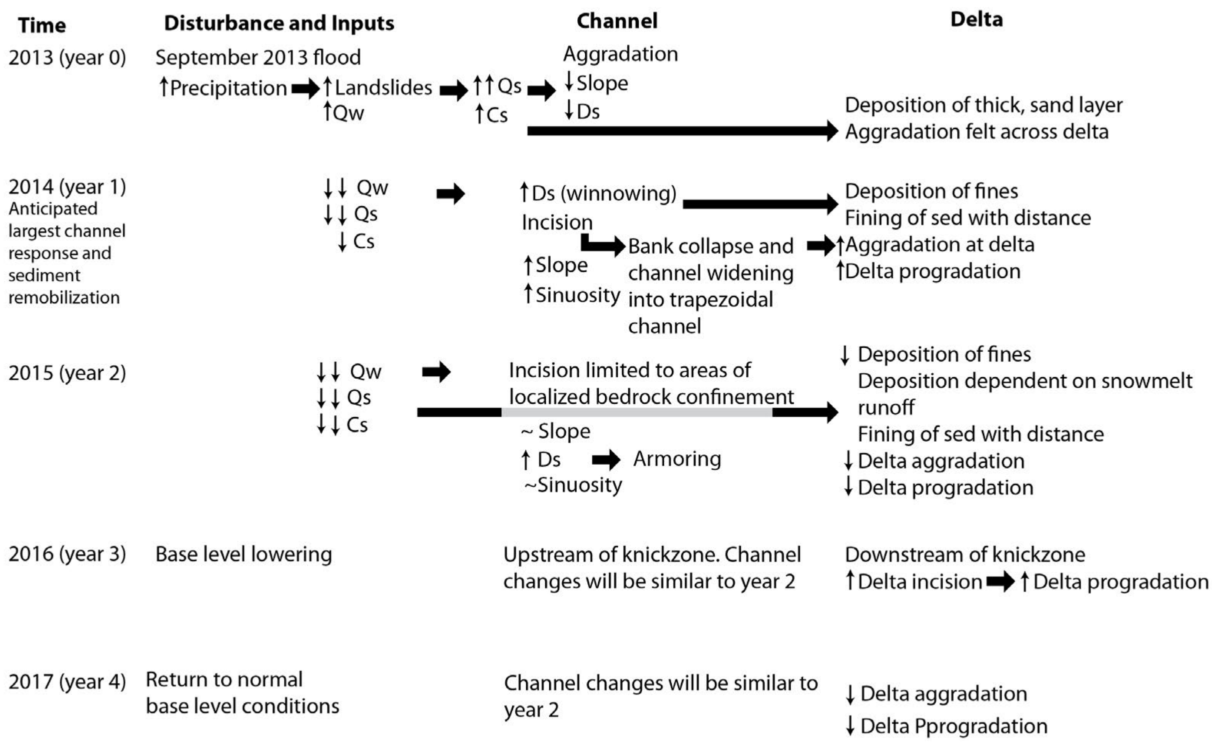


**Figure G.1:** A conceptual model that relates time since the September 2013 flood to observed and assumed changes in the channel and delta in response to disturbances and upstream river inputs.